IAEA-TECDOC-1987

IAEA TECDOC SERIES

IAEA-TECDOC-1987

An Introduction to Probabilistic Fault Displacement Hazard Analysis in Site Evaluation for Existing Nuclear Installations

IAEA
International Atomic Energy Agency

IAEA SAFETY STANDARDS AND RELATED PUBLICATIONS

IAEA SAFETY STANDARDS

Under the terms of Article III of its Statute, the IAEA is authorized to establish or adopt standards of safety for protection of health and minimization of danger to life and property, and to provide for the application of these standards.

The publications by means of which the IAEA establishes standards are issued in the **IAEA Safety Standards Series**. This series covers nuclear safety, radiation safety, transport safety and waste safety. The publication categories in the series are **Safety Fundamentals**, **Safety Requirements** and **Safety Guides**.

Information on the IAEA's safety standards programme is available at the IAEA Internet site

www.iaea.org/resources/safety-standards

The site provides the texts in English of published and draft safety standards. The texts of safety standards issued in Arabic, Chinese, French, Russian and Spanish, the IAEA Safety Glossary and a status report for safety standards under development are also available. For further information, please contact the IAEA at: Vienna International Centre, PO Box 100, 1400 Vienna, Austria.

All users of IAEA safety standards are invited to inform the IAEA of experience in their use (e.g. as a basis for national regulations, for safety reviews and for training courses) for the purpose of ensuring that they continue to meet users' needs. Information may be provided via the IAEA Internet site or by post, as above, or by email to Official.Mail@iaea.org.

RELATED PUBLICATIONS

The IAEA provides for the application of the standards and, under the terms of Articles III and VIII.C of its Statute, makes available and fosters the exchange of information relating to peaceful nuclear activities and serves as an intermediary among its Member States for this purpose.

Reports on safety in nuclear activities are issued as **Safety Reports**, which provide practical examples and detailed methods that can be used in support of the safety standards.

Other safety related IAEA publications are issued as **Emergency Preparedness and Response** publications, **Radiological Assessment Reports**, the International Nuclear Safety Group's **INSAG Reports**, **Technical Reports** and **TECDOCs**. The IAEA also issues reports on radiological accidents, training manuals and practical manuals, and other special safety related publications.

Security related publications are issued in the **IAEA Nuclear Security Series**.

The **IAEA Nuclear Energy Series** comprises informational publications to encourage and assist research on, and the development and practical application of, nuclear energy for peaceful purposes. It includes reports and guides on the status of and advances in technology, and on experience, good practices and practical examples in the areas of nuclear power, the nuclear fuel cycle, radioactive waste management and decommissioning.

AN INTRODUCTION TO PROBABILISTIC FAULT DISPLACEMENT HAZARD ANALYSIS IN SITE EVALUATION FOR EXISTING NUCLEAR INSTALLATIONS

The following States are Members of the International Atomic Energy Agency:

AFGHANISTAN
ALBANIA
ALGERIA
ANGOLA
ANTIGUA AND BARBUDA
ARGENTINA
ARMENIA
AUSTRALIA
AUSTRIA
AZERBAIJAN
BAHAMAS
BAHRAIN
BANGLADESH
BARBADOS
BELARUS
BELGIUM
BELIZE
BENIN
BOLIVIA, PLURINATIONAL STATE OF
BOSNIA AND HERZEGOVINA
BOTSWANA
BRAZIL
BRUNEI DARUSSALAM
BULGARIA
BURKINA FASO
BURUNDI
CAMBODIA
CAMEROON
CANADA
CENTRAL AFRICAN REPUBLIC
CHAD
CHILE
CHINA
COLOMBIA
COMOROS
CONGO
COSTA RICA
CÔTE D’IVOIRE
CROATIA
CUBA
CYPRUS
CZECH REPUBLIC
DEMOCRATIC REPUBLIC OF THE CONGO
DENMARK
DJIBOUTI
DOMINICA
DOMINICAN REPUBLIC
ECUADOR
EGYPT
EL SALVADOR
ERITREA
ESTONIA
ESWATINI
ETHIOPIA
FIJI
FINLAND
FRANCE
GABON
GEORGIA
GERMANY
GHANA
GREECE
GRENADA
GUATEMALA
GUYANA
HAITI
HOLY SEE
HONDURAS
HUNGARY
ICELAND
INDIA
INDONESIA
IRAN, ISLAMIC REPUBLIC OF
IRAQ
IRELAND
ISRAEL
ITALY
JAMAICA
JAPAN
JORDAN
KAZAKHSTAN
KENYA
KOREA, REPUBLIC OF
KUWAIT
KYRGYZSTAN
LAO PEOPLE’S DEMOCRATIC REPUBLIC
LATVIA
LEBANON
LESOTHO
LIBERIA
LIBYA
LIECHTENSTEIN
LITHUANIA
LUXEMBOURG
MADAGASCAR
MALAWI
MALAYSIA
MALI
MALTA
MARSHALL ISLANDS
MAURITANIA
MAURITIUS
MEXICO
MONACO
MONGOLIA
MONTENEGRO
MOROCCO
MOZAMBIQUE
MYANMAR
NAMIBIA
NEPAL
NETHERLANDS
NEW ZEALAND
NICARAGUA
NIGER
NIGERIA
NORTH MACEDONIA
NORWAY
OMAN
PAKISTAN
PALAU
PANAMA
PAPUA NEW GUINEA
PARAGUAY
PERU
PHILIPPINES
POLAND
PORTUGAL
QATAR
REPUBLIC OF MOLDOVA
ROMANIA
RUSSIAN FEDERATION
RWANDA
SAINT LUCIA
SAINT VINCENT AND THE GRENADINES
SAMOA
SAN MARINO
SAUDI ARABIA
SENEGAL
SERBIA
SEYCHELLES
SIERRA LEONE
SINGAPORE
SLOVAKIA
SLOVENIA
SOUTH AFRICA
SPAIN
SRI LANKA
SUDAN
SWEDEN
SWITZERLAND
SYRIAN ARAB REPUBLIC
TAJIKISTAN
THAILAND
TOGO
TRINIDAD AND TOBAGO
TUNISIA
TURKEY
TURKMENISTAN
UGANDA
UKRAINE
UNITED ARAB EMIRATES
UNITED KINGDOM OF GREAT BRITAIN AND NORTHERN IRELAND
UNITED REPUBLIC OF TANZANIA
UNITED STATES OF AMERICA
URUGUAY
UZBEKISTAN
VANUATU
VENEZUELA, BOLIVARIAN REPUBLIC OF
VIET NAM
YEMEN
ZAMBIA
ZIMBABWE

The Agency’s Statute was approved on 23 October 1956 by the Conference on the Statute of the IAEA held at United Nations Headquarters, New York; it entered into force on 29 July 1957. The Headquarters of the Agency are situated in Vienna. Its principal objective is “to accelerate and enlarge the contribution of atomic energy to peace, health and prosperity throughout the world”.

IAEA-TECDOC-1987

AN INTRODUCTION TO PROBABILISTIC FAULT DISPLACEMENT HAZARD ANALYSIS IN SITE EVALUATION FOR EXISTING NUCLEAR INSTALLATIONS

INTERNATIONAL ATOMIC ENERGY AGENCY
VIENNA, 2021

For further information on this publication, please contact:

External Events Safety Section
International Atomic Energy Agency
Vienna International Centre
PO Box 100
1400 Vienna, Austria
Email: Official.Mail@iaea.org

Printed by the IAEA in Austria
November 2021

IAEA Library Cataloguing in Publication Data

Names: International Atomic Energy Agency.
Title: An introduction to probabilistic fault displacement hazard analysis in site evaluation for existing nuclear installations / International Atomic Energy Agency.
Description: Vienna : International Atomic Energy Agency, 2021. | Series: IAEA TECDOC series, ISSN 1011–4289 ; no. 1987 | Includes bibliographical references.
Identifiers: IAEAL 21-01464 | ISBN 978-92-0-138321-1 (paperback : alk. paper) | ISBN 978-92-0-138221-4 (pdf)
Subjects: LCSH: Nuclear facilities — Safety measures. | Faults (Geology) — Risk assessment. | Probabilities.

FOREWORD

IAEA Safety Standards Series No. SSG-9, Seismic Hazards in Site Evaluation for Nuclear Installations, covers all aspects of site evaluation relating to seismic hazards. One of the main objectives of a seismic hazard assessment is to determine the fault displacement that may affect the safety of nuclear installations. Thorough evaluation of a new nuclear installation site is required to ascertain whether there are potential capable faults and if so, an alternative site needs to be considered. However, for an existing site a capable fault may be discovered during new investigations. A probabilistic fault displacement hazard analysis of the capable fault can therefore support the overall assessment of nuclear installation safety.

This publication provides an introduction to probabilistic approaches to fault displacement hazard assessment, namely the probabilistic fault displacement hazard analysis (PFDHA) method, and how to evaluate the displacement by fault rupture modelling. The PFDHA method has not been widely adopted in the engineering community and few applications of PFDHA have been carried out at nuclear installation sites. The most relevant applications of PFDHA at nuclear installation sites are described in the appendices.

This publication provides information on how to apply PFDHA to the site safety assessment of existing installations. The publication aims to be a tool for nuclear power plant operating organizations, regulatory bodies, vendors, technical support organizations and researchers in the area of seismic hazard assessment in site evaluation for nuclear installations. The information in this publication may also be useful for reviews of site safety programmes in Member States undertaken as part of the IAEA Site and External Events Design (SEED) service.

The IAEA greatly appreciates the contributions of all those who were involved in the drafting and review of this publication. The IAEA officer responsible for this publication was Y. Fukushima of the Division of Nuclear Installation Safety.

CONTENTS

1. INTRODUCTION

1.1. BACKGROUND

In IAEA Safety Standards No. SSR-1, Site Evaluation for Nuclear Installations [1], surface faulting is identified as one of the natural phenomena that has to be evaluated in site evaluation for nuclear installations. To implement the assessment, IAEA Safety Standards Series No. SSG-9, Seismic Hazards in Site Evaluation for Nuclear Installations [2], describes methods and practices to be used in fault displacement hazard analysis.

For new nuclear installations, site investigations need to evaluate the potential for fault displacement at or near the site, by analysing geological, geophysical, geotechnical and seismological information and data, as well as by developing seismotectonic models, together with additional specific data for the faults in question, in the site vicinity of nuclear installations. Where there is reliable evidence for a capable fault with the potential to affect the installation's safety, the safety of the site needs to be evaluated and, if necessary, an alternative site needs to be considered (see paras 8.3–8.8 of SSG-9 [2]).

For sites with existing nuclear installations, SSG-9 [2] recommends the following:

> "In view of the extensive site investigation required for a nuclear power plant before construction, in general, the situation should not arise in which further consideration has to be given to the potential for fault displacement at the site of an existing nuclear power plant. However, it may be the case that information comes to light that requires a new assessment of fault displacement potential to be made." (Ref. [2], para. 8.9)
>
> "In such circumstances, efforts should first be made to acquire further data relating to the fault of concern. It may be that, by using the definition and the deterministic methodology described in paras 8.3–8.7, no sufficient basis is provided to decide conclusively that the fault is not capable. In this case, with the totality of the available data, probabilistic methods analogous to and consistent with those used for the ground motion hazard assessment should be used to obtain an estimate of the annual frequency of exceedance of various amounts of displacement at or near the surface." (Ref. [2], para. 8.10)

The use of the probabilistic fault displacement hazard analysis (PFDHA) is introduced in para. 8.10, and paras 8.11–8.13 of SSG-9 [2] that describe practical approaches. In addition, para. 4.1 (a) of IAEA Safety Standards Series No. NS-G-2.13, Evaluation of Seismic Safety for Existing Nuclear Installations [3], states: "If a clear resolution of the matter is still not possible, the fault displacement hazard should be evaluated using probabilistic methods."

While IAEA Safety Standards Series publications recommend PFDHA, actual examples of applications of PFDHA are quite limited. Therefore, Member States expressed a need for a publication to support the implementation of the IAEA Safety Standards, especially SSR-1 [1] and SSG-9 [2], to provide information on the state-of-the-art practice and detailed technical elements of PFDHA.

1.2. OBJECTIVE

The objective of this publication is to provide information on the state-of-the-art practice and detailed technical elements related to PFDHA. Such information will assist Member States in following the recommendations of SSG-9 [2] for re-evaluating fault displacement hazards at existing nuclear installations.

The content of the publication aims to delineate the most important aspects of PFDHA (including up-to-date practices, open problems, and challenging issues) within a coherent framework. Attention has been paid to filling conceptual gaps among specific arguments (e.g., empirical evaluations vs physics-based simulation schemes) that are generally developed individually.

This publication is not intended to be a substitute for specific training in fault displacement hazard analysis. It is aimed at supplying a reference text for trained users who are not specifically aware of the most recent developments in the topics covered in this publication but are responsible for maintaining the safety of nuclear installations and external hazards assessments for existing nuclear installations.

1.3. SCOPE

This publication describes current methodologies of PFDHA including data needs, empirical and physics-based approaches. This publication also presents some practical applications of PFDHA studies by Member States and describes some of the challenges experienced by Member States when applying PFDHA. It provides state-of-the-art practices to support Member States in their implementation of PFDHA at their nuclear installation sites.

The scope of this publication includes the basics of fault displacement hazard evaluation. PFDHA methodologies and some case studies are presented to improve fault displacement hazard analysis for existing nuclear installation sites. The focus is on methods for calculating the relationship between fault displacement amount and the corresponding annual exceedance probability/frequency for a specific site.

The scope does not include office and field procedures for characterizing details of fault displacement direction, width, or distribution across a zone at the scale that might be needed for detailed site-specific engineering assessment. In addition, engineering application of the results of the fault displacement hazard analysis is out of the scope of this publication.

1.4. STRUCTURE

Section 2 describes surface faulting characteristics and data, including methods for surface faulting data collection. Section 3 explains PFDHA. Section 4 provides three case studies where PFDHA has been performed to support the evaluation of nuclear facilities. Section 5 presents the conclusions.

This publication contains also four Appendices. Appendix I shows example of extensively documented earthquake surface rupture. Appendix II provides detailed information for earthquake approach. Appendix III contains fundamental concepts for the dynamic rupture approach. Appendix IV presents detailed information for friction laws, slip distribution and stress drop parametrization.

2. SURFACE FAULTING CHARACTERISTICS AND DATA

Vibratory ground motion due to the propagation of elastic waves is the main source of damage to facilities during an earthquake. In addition, earthquakes might generate other permanent effects at the surface, such as surface faulting and tectonic deformation. Such effects can pose significant hazards to facilities [4].

Surface faulting (or surface fault displacement) is a permanent displacement of the ground surface along a fault expected to occur during shallow moderate ($6 < M_W < 7$) and strong ($M_W > 7$) events, but it might occur for even smaller earthquakes in certain specific seismotectonic conditions. Surface faulting is the earthquake-related phenomenon addressed in fault displacement hazard assessment.

Surface rupture is classified into principal (primary) faulting along the earthquake source and distributed (secondary and triggered) faulting along fault structures. Tectonic deformation such as tilting, subsidence, rotation and extensional strain can also occur during an earthquake and potentially could pose damage to facilities or lifelines, but they are not included in fault displacement hazard assessment and therefore not discussed in this publication. Secondary effects, including soil liquefaction and landslides, can also pose risk to facilities and lifelines and their occurrence is mainly dependent on ground shaking and site conditions. This publication does not consider them either.

This section provides essential information on the surface fault slip phenomenon that occurs during (co-seismic) and after (post-seismic) large earthquakes, and addresses factors that control the pattern of surface faulting. A series of characteristic parameters to be retained for the foundation of a worldwide and unified database are proposed, in order to derive those empirical relationships in the future. During the last two decades, new mapping techniques allow to improve characterization of earthquake-related surface and subsurface deformation. These techniques will surely continue to provide enriched and detailed datasets.

2.1. SURFACE FAULTING AND CAPABLE FAULTS

Surface rupture characterization, analysis and interpretation include the following elements: (1) fault rupture characteristics described by location, style of faulting, slip amount and distribution [5]; (2) earthquake source mechanics and rupture propagation [6, 7]; and (3) surface-rupture history (slip rate, timing and elapsed time) [8]. All this information is important to assess the potential for an earthquake-related hazard of geological structures with relevant other information, e.g., sediments, rock rigidity, stress regime.

In SSR-1 [1], the definition of capable fault is written like following:

> "A fault is considered capable if, on the basis of geological, geophysical, geodetic or seismological data (including palaeoseismological and geomorphological data), one or more of the following conditions applies:
>
> (a) The fault shows evidence of past movement or movements (significant surface deformations and/or dislocations) of a recurring nature within such a period that it is reasonable

to infer that further movements at or near the surface could occur. In highly active areas, where both earthquake data and geological data consistently and/or exclusively reveal short earthquake recurrence intervals, periods of the order of tens of thousands of years may be appropriate for the assessment of capable faults. In less active areas, it is likely that much longer periods will be required.

(b) A structural relationship with a known capable fault has been demonstrated such that movement of one could cause movement of the other at or near the surface.

(c) The maximum potential earthquake associated with a seismogenic structure is sufficiently large and at such a depth that it is reasonable to infer that, in the geodynamic setting of the site, movement at or near the surface could occur. (SSR-1, page 18)"

Capable faults can potentially threaten facilities because of surface rupture associated with earthquakes. Such faults are characterized by using appropriate methods to identify (recurring) displacements in recent times, which are defined from tens of thousands of years (active regions[1]) to millions of years (intraplate regions). Outcropping faults are the primary candidates. There are many earthquakes during which co-seismic surface rupture is observed along capable faults with known paleoseismic activity. For example, the 2016 M_W 7.8 Kaikoura earthquake in New Zealand ruptured a series of faults up to the ground surface, including the Kekerengu fault (slip rate ~25 mm/a) which had ruptured three times in the past 1200 years [9]. The 2010 M_W 7.2 El Mayor-Cucapah and 1892 M_W ~ 7 Laguna Salada earthquake (Baja California, northern Mexico) also breached the ground along faults which have a long slip history [10]. In the moderate magnitude range, Cinti et al. in 2011 [11] demonstrated that the rupture that appeared during the 2009 M_W 6.3 L'Aquila earthquake in Central Italy reactivated fault strands that had been active during the Holocene and Upper Pleistocene. Similarly, the pattern of surface faulting associated with the 2016 M_W 6.5 Norcia, central Italy, earthquake is clearly associated with well-known capable faults with a well-constrained paleoseismic history in the last tens of thousands of years [12]. Nevertheless, earthquakes might occur also on faults that were not previously mapped (e.g., 2010 Darfield, New Zealand and 2019 Ridgecrest, California events) due to lack of detailed investigation or new rupture.

Blind (or buried) faults might also cause surface deformation of sediment. Examples are the 2004 M_W 6.6 Chuetsu (Mid-Niigata) earthquake and the 2007 M_W 6.6 Chuetsu-oki (Off Mid-Niigata) earthquake in Japan, as well as the 2016 M_W 6.4 Meinong event in Taiwan. Maruyama et al. in 2007 [13] observed that an active fold limb ruptured with less than 20 cm fault displacement during the 2004 M_W 6.6 Chuetsu event, ~10 km east of the epicentre, while the 2007 M_W 6.6 Chuetsu-oki earthquake was responsible for the co- and post-seismic uplift of a 15 km long and 1.5 km wide active anticline, located 15 km east of the epicentre [14]. In Taiwan, the blind Meinong rupture associated with the

[1] In extremely active regions of recurrence less than several hundred years, more detailed investigations based on observations are available and valuable to evaluate the hazard.

mainshock triggered large-wavelength warping and related open cracks (<5 mm of opening) at the ground surface, which was attributed to slip on shallow (<5 km deep) flat-and-ramp faults of the fold-and-thrust belt [15].

Creeping faults are *a priori* not considered for seismic hazard evaluation when they are purely aseismic [2]. Nevertheless, their occurrence needs to be considered for PFDHA if they are not purely aseismic. In fact, recent studies suggest that some faults that exhibit creep need to be carefully characterized to assess past earthquake activity. First, creeping faults are rarely purely aseismic both in space and/or in time [16]. The Hayward fault in California [17] or the Longitudinal fault in Taiwan [18] are known to have generated significant earthquakes despite their surface creep rate. A very recent example, the 2017 M_W 6.5 Leyte, Philippines earthquake, occurred along a creeping section of the Central Philippine fault [19]. Because of modern geodetic techniques, it is now possible to survey earthquake-related surface slip in time as well in space: these data are providing growing evidence that afterslip (i.e. aseismic slip after earthquakes) is common after shallow crustal events [20].

2.2. CHARACTERISTICS OF SURFACE FAULTING

Surface faulting during an earthquake typically consists of discrete and continuous rupture on the ground, with generation of a scarp with a newly free-face (Figures 1 and 2). In other cases, surface-faulting phenomenon appears as a fold, a flexural scarp in case of dip slip faulting (Figure 3) or bending and warping of piercing lines or of surfaces (Figure 1b). There are numerous examples of intermediate cases, including the combination of surface slip and bulk deformation like warping, bending or folding of the surrounding crust. This was, for instance, the case along the 2010 M_W 7.2 Darfield earthquake with ~2 m of dextral rupture on the fault and with additional ~5 m of large-aperture offset accommodated over several tens of metres, as attested by the bending of human-made features [21]. Similar evidences were observed also for the 1999 M_W 7.7 Chi-Chi earthquake [22]. Fault scarps might be complex on a scale of metres to few tens of metres, with branches and splays for which the number and offset depend on fault dip and local geology of superficial layers. A recent classic example is the 2010 M_W 7.2 El Mayor-Cucapah earthquake (Figure 2) extensively described in [23].

FIG 1. Two views of the same site (Colli Alti e Bassi, Castelluccio, Norcia) where ruptures broke the ground surface following the 30 October 2016, M_W 6.5 Norcia earthquake in Central Italy, illustrating a possible control of surface geology on surface faulting pattern. Photos by Stéphane Baize (2016). a) Southward view of co-seismic fault scarp in bedrock (Jurassic limestones) in the foreground (top is outlined by a white dashed line), changing to a gentle warping in the alluvium (blue line), then to a new scarp in colluvial sediments as shown in b). Black arrows mark the top of long-term cumulative scarp. b) Northward view of the same rupture segment, faulting pattern changes from a sharp scarp in colluvium to gentle warping in loose alluvium.

FIG 2. Examples of principal versus secondary ruptures in northern Mexico (Baja California) that appeared during the April 6, 2010, M_W 7.2 El Mayor-Cucapah earthquake. a) Principal faulting along a series of east-dipping fault segments of the El Mayor Cucapah fault zone (EMC); b), c) and d) show distributed ruptures, sometimes at large distances, along known faults such as the west-dipping Laguna Salada fault that ruptured in 1892 and 1934. Photos by Stéphane Baize (2016).

FIG 3. Surface faulting along the Papatea fault segment from the 2016 M_W 7.8 Kaikoura earthquake. a) Plurimetric and large wave-length flexural vertical separation (dZ) of an originally flat alluvial surface (white dashed line), corresponding to an oblique (left-lateral) reverse faulting at very shallow depth. Note the tilt of the pine trees. b) A view at the hinge line of the flexural scarp, showing open cracks (with little individual vertical offsets) spreading across the fold limb. Black arrow depicts the location of the cumulative Papatea fault in the distance. Photos by Stéphane Baize (2017).

An earthquake typically nucleates along a fault at depth which then propagates laterally and vertically. Rupture propagation at depth occurs on a single ‘principal’ (or ‘primary’) fault that might reach the surface. Primary rupture might occur along a simple plane where massive slip is concentrated (e.g., 1999 M_W 7.5 Izmit earthquake). However complex events during which various fault segments with large displacement are mobilized are not rare (e.g., 1992 M_W 7.3 Landers in California, USA; 2010 M_W 7.2 Darfield and 2016 M_W 7.8 Kaikoura in New Zealand; 2019 M_W 6.4 and M_W 7.1 Ridgecrest in California, USA). These segments might be parallel laterally-stepping or branching. Both geodetic and seismologic models show that the largest displacements at depth are concentrated on slip patches along the so-called ‘principal’ fault plane(s), and the largest surface fault displacement is generally observed along the projection of this plane at the surface (e.g. 2016 M_W 6.5 Norcia [24, 25]).

Besides primary ruptures, historical and certainly many recent events show the occurrence of off-fault deformation and faulting on connected segments, such as splays, parallel branches or other structurally connected-to-primary fault segments. The displacement amount on these off-fault ruptures is generally less than on the primary fault and the continuity of the segments is normally reduced on those so-called ‘secondary’ ruptures. During large events, minor displacements (several mm to several cm) of tectonic origin might also occur along mapped faults at large distances, on clearly non-connected strands. Hosted on segments without any structural relationships with the primary fault, the slip events are suspected to occur on faults that are close to failure. These remote ruptures are suspected to have been ‘triggered’ by seismic waves or strain. Triggered aseismic faulting occurred on historically active faults of southern California after the 2010 M_W 7.2 El Mayor-Cucapah earthquake in northern Mexico, at distances exceeding 100 km [26]. Petersen et al. in 2011 [27] were the first to separate the two kinds of off-fault distributed rupture in their dataset. These authors defined triggered rupture when it occurs at a distance of more than 2 km from the main (primary) fault. The corresponding data were not included to derive empirical regressions of off-fault displacement with distance. As stated in [27]: “adjacent faults are an important source of fault-rupture hazard and should be considered in the analysis"; and they need to be considered separately because they respond to different processes than typical secondary faulting.

The major issue is then how to objectively define a triggered rupture. The basic characteristic of a connected slip is a direct structural link (at the surface or at depth) between fault segments, but this might be too restrictive to encompass all the 'secondary' ruptures related to the earthquake deformation, and therefore a geodetic definition is more appropriate. In the crustal volume strained during the interseismic period around a principal fault, 'secondary' slip is scattered in this volume during the earthquake (elastic rebound) (Figure 4). With challenging the development of Interferometric Synthetic Aperture Radar (InSAR) techniques eliminating any gravity relevant deformations or fractures, for any shallow earthquakes around the world, it might be possible to map in great detail and quantify the co-seismic ground deformation at the scale of the entire earthquake-related deformed volume: 'triggered' slip, beyond this, could then be challenging to distinguish univocally using an unbiased and reproducible criterion.

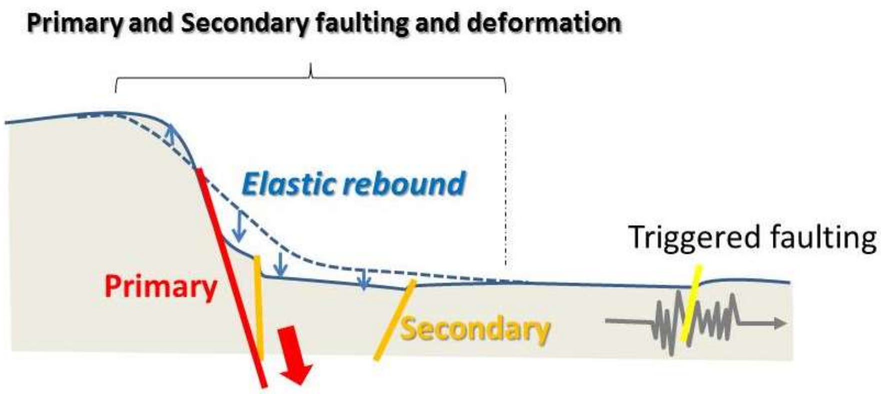

FIG 4. Schematic diagram illustrating how and where secondary and triggered rupture can occur off the principal fault during a normal faulting earthquake.

When compiling a database for further analyses (i.e., deriving empirical regressions or scaling relationships), it is necessary to first identify the major and 'primary' (or 'principal') fault which is quite continuous in the earthquake-related deformation volume (but complexity could be included like stepovers, gaps) and which hosts maximum displacements. This 'primary' fault generally corresponds to the fault with the largest cumulative history. Its surface trace needs to be consistent with fault plane geometry determined from seismologic and geodetic data and models.

2.3. FACTORS CONTROLLING SURFACE FAULTING

The following Sections 2.3.1 to 2.3.4 describe the factors that control the occurrence and amount of surface faulting, namely the parameters depending on the causative earthquake (magnitude, focal mechanism) and associated fault (geometry and depth), and those depending on site conditions.

2.3.1. Magnitude

The most major earthquake parameter that controls surface faulting occurrence and size is the event magnitude. It is largely recognized that surface faulting is generally not expected for events smaller than M_W 6. This has been validated to some degree by the statistical analyses published in [28].

The probability function of surface rupturing versus magnitude published in [29] suggests that the Japanese earthquakes have a lower likelihood to rupture the surface than in U.S. and other cases worldwide. Nevertheless, in some cases due to peculiar local seismotectonic and site conditions, including very shallow depths, small events down to M_W 4.0 have been observed to rupture the ground surface along identified faults [30], sometimes with unusually large surface displacements (e.g., in the high elevation eastern Cordillera of the Ecuadorian Andes [31], or in intraplate southern France [32]). Surface rupture appeared along the Fiandaca fault on the eastern flank of the Etna stratovolcano, during a small magnitude and very shallow event (2018 M_W 4.9, depth ~2 km), with length up to 7.5 km and net slip up to 40 cm [33, 34].

2.3.2. Focal mechanism

In the various compilations, the probability of surface rupture also depends on fault kinematics: strike-slip and normal earthquakes are expected to produce surface faulting at smaller magnitudes than reverse earthquakes. At a first glance, the 50% probability that the primary fault breaches the ground surface is for M_W 6.0 strike-slip [28], M_W 6.2 normal [35] and M_W 6.5 reverse earthquakes [36]. It must be noted that the empirical relationships that indicate these probabilities might be based on not statistically representative of the phenomenon.

2.3.3. Distance

Like any co-seismic effects on the natural and human environment, the occurrence and extent of surface faulting at a specific point is not only dependent on magnitude, but also on the distance to the source. Similar to ground motions attenuation trends, fault displacement rapidly attenuates with distance from the fault rupture to the secondary strands, splays and branches, typically over several hundreds of metres. In empirical predictions of ground motion, there are several ways to determine the distance to the source of the shaking, including the distance to epicentre, hypocentre, fault plane, projection of fault plane at the surface, and projection of the shallow fault tip at the surface. To date, for fault displacement hazard, distances are calculated as the shortest distance to the principal fault trace at the surface (Figure 5).

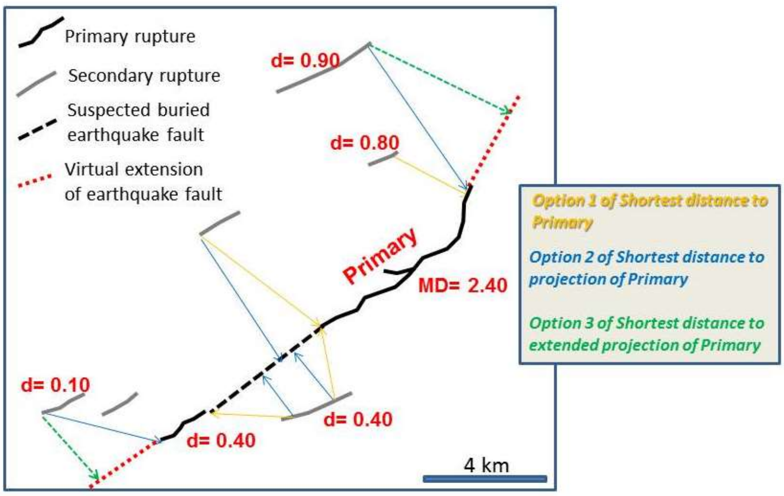

FIG 5. Schematic diagram showing different options of distance measures from distributed ruptures evidence to the primary fault trace. Data are from the 1987 Edgecumbe earthquake in New Zealand [37].

2.3.4. Site specific fault parameters

The developers of empirical ground motion models have significantly increased the number of parameters to predict ground motions with distance. In a similar way, even surface displacement would also need to be accounted for more predictor parameters, for instance by incorporating 'local' site conditions, geometrical and structural complexities such as principal fault dip, hanging wall effect. The fault structure and geometry, including its depth and dip, need to be the first set of critical parameters to predict surface rupture likelihood and pattern.

2.3.4.1. Principal fault geometry

With a dipping principal fault, it has been observed that the rupture generally propagates into the hanging wall block and creates distributed faulting like during the 1999 M_W 7.7 Chi-Chi earthquake in Taiwan [22]. Fault geometry at depth, similarly to near surface, largely controls surface-faulting pattern and the most striking cases are those occurring on shallow faults with very low dip in compressional flat-and-ramp tectonic environments. In such cases, primary surface faulting can be absent (e.g., M_W 7.8 2015 Gorkha, Nepal event [38]) or displacement is largely limited to secondary or triggered ruptures (see previously cited example in Taiwan). It is important to note that even blind faults could cause secondary surface rupture and thus they could be considered in hazard analyses.

Principal fault changes in strike or continuity (bends, step-over) usually induce slip transfer across these discontinuities leading to rupture complexity: this is clearly shown by cases like the 1954 surface wave magnitude (M_s) 6.8 Dixie Valley, Nevada earthquake (USA) [39]. For building a worldwide database, the along-strike structural pattern of a principal fault is a parameter that can control surface rupture because faulting is much more distributed at fault tips, stepovers, bends and other geometric irregularities (simple vs complex ruptures, e.g. 2010 El Mayor-Cucapah earthquake [23]). To account for this, it is suggested to include the location of the site with respect to structural entities of the principal fault in future databases: a regular site is near a linear, well-defined portion of principal fault; and a complex site is located in stepovers, relays or bends, within a fault gap or at a fault tip.

2.3.4.2. Surface geology

Surface ruptures of the 2010 M_W 7.2 El Mayor-Cucapah earthquake, in northern Mexico, were extensively studied both by geologists in the field and by geodesists. Classic field measurements, as well as high-resolution geodetic measurements, provide an accurate mapping, a complete analysis of the rupture and an insightful synthesis of the factors controlling the rupture zone fabric and pattern [40]. These studies document how local geology, affects the fault zone width, the number of fractures, their arrangement and connectivity, the displacement distribution over the rupture zone and the displacement amount on each fracture. These studies clearly conclude, for instance, that the width of the ruptured zone increases with the thickness of surficial and loose sediments above the bedrock fault. Sandbox models have confirmed the role of surface geology because measured near-surface material stiffness notably influences the rupture pattern and fabric, and even the likelihood of surface slip for reverse active faults [41, 42].

Numerous paleoseismological studies, as well as recent surface rupture cases, for instance in central Italy during the 2009 M_W 6.3 L'Aquila and 2016-2017 M_W 6.5 Amatrice-Norcia earthquake sequence [25], show that the rupture preferentially reaches the ground surface along pre-existing fault segments. A similar conclusion has been reached after a detailed study of pre-earthquake imagery in the Ridgecrest sequence region, illuminating that 2019 surface rupture occurred along pre-existing faults [43]. This empirical observation is also validated by the sandbox experiment in [42]. Surface faulting was obtained with lower shortening value for previously faulted material, whatever its lithology and stiffness.

Based on these elements, it was considered important to include a basic classification in a surface faulting database (cover beds vs basement; basic sediment lithology), that can be realistically observed in the field.

2.4. METHODS FOR SURFACE FAULTING DATA COLLECTION

Field mapping is the classical method to gather surface rupture data in the period immediately after an earthquake, as well as a long time after its occurrence. On the other hand, the development of remote sensing techniques (InSAR, LiDAR) allows enriching the surface rupture datasets. The following Sections 2.4.1 and 2.4.2 describe the methods.

2.4.1. Field mapping

Field mapping is a fundamental data source for describing surface faulting. Typical measurements of fault offsets are performed by geologists, using classical tools like tape, on morphological features like ground surface, drainage thalwegs and channel boundaries. The quality of the measurements generally depends on the preservation of the analysed feature and on the experience of the practitioner. As mentioned in [44], faint and distributed slip planes are easier to map in the field. Traditional mapping is necessary because it is the best approach to understand the morphological features and to validate a feature as an offset marker and to exclude other options (e.g., a deflection of a channel). Field measurement is therefore the ultimate technique to accurately measure the displacements on the fault planes. In most of parts of the world, it is still the best approach to obtain precise measurements particularly when factoring in cost.

Recently, a very significant mapping effort was accomplished in the European earthquake geological community to map the ruptures caused by the 2016-2017 Central Italy sequence, leading to a highly detailed map and dataset (see Appendix I). After the 2019 Ridgecrest sequence with two M_W 6.4 and M_W 7.1 earthquakes in California, the US community mapped in detail the associated surface rupture to embrace its complexity [45].

2.4.2. Remote sensing

Remote sensing techniques have been used for decades to observe earth surface changes. In the early 1980's, Philip and Meghraoui in 1983 [46] used aerial photos to map the surface ruptures caused by the 1980 M_W 7.0 El Asnam earthquake in Algeria. Notably, the first order surface deformation associated with the 1992 M_W 7.3 Landers earthquake has been inferred from Synthetic Aperture Radar (SAR) data from European Remote Sensing (ERS) satellite ERS-1 [47]. The continuing development of remote sensing techniques like aerial photo correlation and structure from motion photogrammetry, SAR techniques, aerial or terrestrial Light Detection And Ranging (LiDAR) laser (also named 3-D laser scanning) and the increasing frequency and resolution of satellite images improve the accuracy of land change measurement. With a capacity to capture decimetre-scale offsets, LiDAR can provide a significant complement to fieldwork [48] with which there is generally a good accordance [49]. The evaluation was also facilitated by the InSAR maps available in the early phase (e.g., after the 2014 M_W 6.0 South Napa earthquake [50]). In the 2010 M_W 5.0 Pisayambo, Ecuador earthquake, any ruptures would not have ever been recognized without InSAR analysis, in such a remote and high-elevation region of the Andes [31]. Recent cases have underlined the large benefits of remote techniques in zones with no accessibility because of either security issues (optical correlation in eastern Pakistan [51]) or in regions with extensively covered areas (InSAR). With the Japanese Advanced Land Observing Satellite (ALOS) InSAR, subtle deformation features are measurable. Refer, for example, to the work of [52] who mapped distributed ruptures associated with the 2016 M_W 7.0 Kumamoto earthquake around south-west of the Aso volcano, Kyushu, Japan. Ritz et al. in 2020 [32] used freely available data from the Sentinel satellites to estimate the relative vertical throw along the surface rupture. These techniques open the possibility to increase the off-fault surface faulting datasets related to large earthquakes and even the basic detection of primary/distributed faulting during moderate to small magnitude events.

Correlation of pre- and post-seismic optical images is another interesting technique to capture the earthquake-related deformation fields. Optical correlation is of major interest for detecting and measuring horizontal changes. Together with other high-resolution techniques, an important contribution of this technique is the possibility to measure inelastic deformation around fault strands. Recent studies (e.g., 1992 Landers and 1999 Hector Mine earthquakes [53]) could detect and evaluate the amount of off-fault diffuse and inelastic deformation that characterizes most of the damage zones around large magnitude earthquakes.

Obvious benefits can be expected from such innovative techniques. For recent ruptures, they potentially yield a large number of measurements at a same site, and this is important for estimating the local variability and, in a sense, giving estimates of uncertainty. For both, remote and field studies, it is crucial to measure all the available offset geomorphic features, to avoid biases by preselecting features. This information is reported in the Surface Rupture during Earthquakes (SURE) database (see discussion in Section 2.6). For instance, information on local geology needs to be collected; it could be used in further statistical analyses.

2.5. EXISTING SURFACE FAULTING DATASETS

Empirical relationships are the basis of most seismic hazard analyses, whether they are deterministic or probabilistic. With regards to the surface rupture hazard, the hazard level depends on several issues:

- The probability of primary faulting describes the likelihood with which an active fault will break the surface. This relationship is based on the number of events (in databases of past earthquakes) during which surface faulting has been observed as a function of magnitude [7, 28, 29, 35, 54, 55].

— The conditional probability, given a specified magnitude, that the displacement at a specific point along the primary fault will exceed a defined value of displacement, is also assessed through analysis of slip distribution along past earthquakes [7, 56–59].
— The probability of secondary faulting has been proposed for normal faulting earthquakes in the Basin and Range Province, western USA [58], strike-slip earthquakes [27], reverse earthquakes [59], and all fault types in Japan [29]. This probability function is basically derived by the counting pixels (in an appropriately sized mesh) where a slip has been observed, at successive distances to the primary fault.
— The conditional probability of exceedance of a specified value of secondary displacement to occur is expressed with respect to the distance to the primary fault. It has been derived by different authors with scarce datasets for strike-slip faulting [27], normal faulting [58], reverse faulting [59] and Japanese events of all types [29].

For displacement hazards, secondary faulting is simplified and considered as a random process, in the sense that it depends on the distance to the primary fault and other specific factors (e.g., soil, primary displacement complexity, energy release), without any control of pre-existing structures. Well-studied recent cases show that secondary faulting occurs not only on detectable faults, but also in 'unexpected' places [23, 25], and statistical studies focused on secondary faulting occurrence are missing. Pre-existing faults have to be investigated around the existing nuclear installation site and respected to evaluate the dataset.

To date, the main datasets that have been used in fault displacement hazard assessment are the following:

— In an unpublished report, Pezzopane and Dawson in 1996 [35] compiled the surface faulting data from 21 western North American earthquakes that occurred in the extensional Cordillera of the western U.S. and Mexico between 1869 and 1995, covering the magnitude range from M_W 5.2 (1975 Galway Lake) to M_W 7.5 (1887 Sonora). This dataset mainly includes normal-faulting earthquakes but also strike-slip events (extensional), and the majority includes primary and secondary ruptures.
— Youngs et al. in 2003 [58] used the normal faulting earthquake dataset of [35] to derive empirical relationships (conditional probability of distributed faulting, for instance). This report encompasses a set of fault earthquake maps with information on local observations of surface faulting. Several surface ruptures were transferred from this report into the SURE database [60], basically using those fault maps and related displacement information.
— Petersen et al. in 2011 [27] compiled the surface displacement data for seven strike-slip earthquakes (five from the USA) with information for both primary and distributed slip, within the M_W 6.5 to 7.6 range. The events are 1968 M_W 6.6 Borrego Mountain, 1979 M_W 6.5 Imperial Valley, 1987 M_W 6.5 Superstition Hills, 1992 M_W 7.3 Landers, 1995 M_W 6.9 Kobe (Japan), 1999 M_W 7.6 Izmit (Turkey) and the 1999 M_W 7.1 Hector Mine. Statistics for the on-fault

displacements have been supplemented with the Wesnousky database [57]. From their compilation, Petersen et al. in 2011 [27] have considered that observations farther than 2 km from the primary fault are 'triggered' and for this reason were not included in the statistics. The statistics of those ruptures are available online as a supplement (see Ref. [27]).

— Moss and Ross in 2011 [36] used an upgraded version of the Lettis et al. database [56] to produce a probability distribution of primary faulting during reverse earthquakes. They explored the spatial variability of slip along the fault plane based on the same datasets and determined the reverse-specific relationships for some terms involved in a PFDHA, except those for distributed faulting. In recent years, Takao et al. in 2014 [61] started filling the gap by developing a set of data for reverse earthquakes with distributed displacement segments and values.
— Nurminen et al. in 2020 [59] used a database containing 15 reverse faulting earthquakes from M_W 4.9 to 7.9, including 2064 fault segments and 1062 vertical displacement observations. The methodology in [59] is based on georeferenced maps of surface ruptures during historical earthquakes of medium-high magnitudes, and on in-situ displacement measurements, and an evaluation of the ranking of those ruptures.

In conclusion, available surface displacement datasets are relatively scarce compared to ground motion datasets and they mostly do not provide a detailed description of the complexity of surface faulting. Moreover, there is no inclusion of any site-specific and local conditions (e.g., soil and subsoil characteristics), which are recognized as important factors controlling the occurrence and pattern of surface faulting. To date, only magnitude and focal mechanism parameters are considered.

2.6. TOWARDS A HOMOGENOUS DATABASE

In the framework of the IAEA International Seismic Safety Centre (ISSC) Extrabudgetary Programme and the TERPRO SURFACE Project [60] of the International Union for Quaternary Research (INQUA), workshops were held in Paris in 2015 and Menlo Park in 2016 with the aim to discuss on how to build a worldwide and unified database of surface ruptures for fault displacement hazard purposes. It appeared that there is a broad and worldwide interest in the probabilistic estimates of displacement amount and its distribution during future earthquakes for the engineering design of infrastructures. Distributed deformation is a key concern, particularly for long baseline structures such as pipelines, tunnels and bridges. The current structure of this worldwide database, so-called SURE for 'SUrface Rupture during Earthquakes', has been fully discussed and agreed by the experts during the above-mentioned workshops.

The workshop participants agreed in compiling the available datasets and implementing them into the SURE format. This first release, which is available online, is described in a scientific publication [62]. The SURE database includes the 'historical cases' already considered in [35] and a few events considered in [59]. Beyond these, it includes data from recent cases which provide a significant amount of data. The database includes 44 earthquakes, mainly from Japan and the USA, with more than 10 000 displacement observations. The earthquakes range from the end of the 19th century to 2016, and their magnitude from M_W 5.0 to 7.9. Strike-slip events are the most numerous (23) followed by normal (11) and reverse (10) events. In the future, it is expected that data will be derived from remote sensing measurements with quantification of variability and uncertainty. Special attention is needed to homogenize the parameters to be implemented. To facilitate this compilation effort, a new template has been developed that allows selecting a set of basic fields useful for building statistical relationships.

The SURE database is structured into three major tables (Figure 6): a 'displacement observation point table'; a 'rupture section table' and an 'earthquake table'. Each displacement observation at geo-referenced point is linked to the 'rupture section table' and to the causative 'earthquake table' through an appropriate identifier, related to a one-to-many record structure. Fields associated to each table are shown in Figure 6. The displacement observation table is the core of the database, containing the basic information for fault displacement hazard assessment. It includes all the observations for the set of earthquakes with required information such as latitude, longitude, and net slip. Slip measurements are recorded as horizontal and vertical components (with associated uncertainties), as this distinction will be ideal for design, as not all structures are equally sensitive to one or the other component. The table also allows for the compilation of 'large aperture offset', i.e., earthquake-related finite displacement which includes the slip on the fault trace (net offset) and the inelastic part of deformation documented that sometimes goes along with (Figure 7). This table also lists the relevant information giving the observation context, such as local surface geology, structural location with respect to principal fault (e. g., location on a straight well-defined segment, step-over, relays, fault tip) (Figure 8). The rupture section table includes primary and distributed fractures (line work) and is stored associated with a polyline vector layer (e.g., Shapefile) for mapping surface ruptures in a geographic information system (GIS). Attributes for the segment file will include the identifier of the causative earthquake and, if any, information on slip history (previously documented fault segment and fault, paleoearthquakes, slip rate). The map showing the geographic distribution of surface ruptures is a fundamental part of the database as this information is used to calculate the rupture probability functions for the fault displacement hazard analysis.

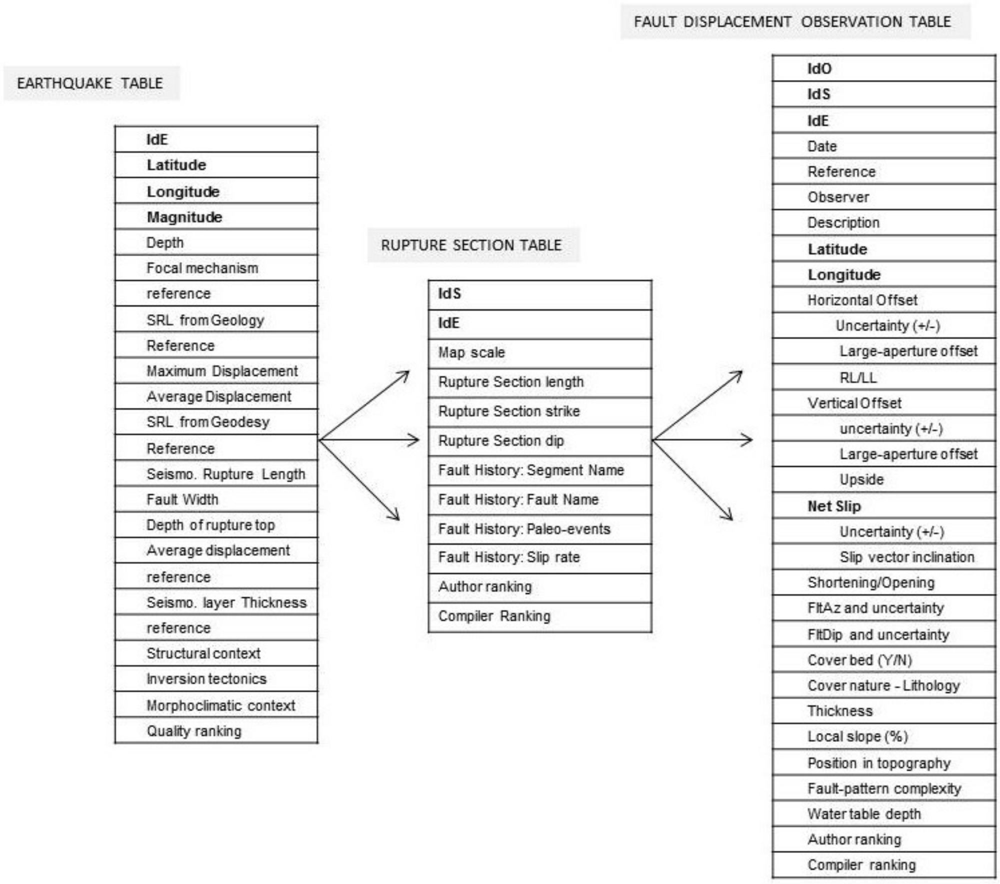

FIG 6. Structure of the SURE database. Three main tables with several attributes and numerical fields are linked following a one-to-many structure.

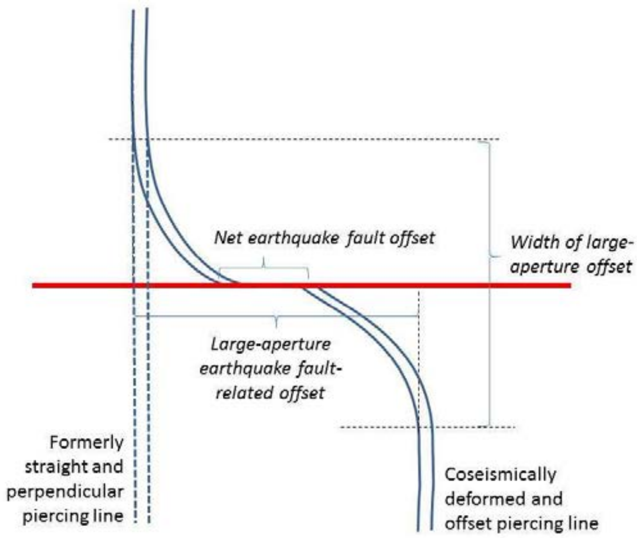

FIG 7. Surface slip can be the combination of discrete rupture along the fault traces and flexural deformation inferred from piercing lines, forming a 'large-aperture' offset.

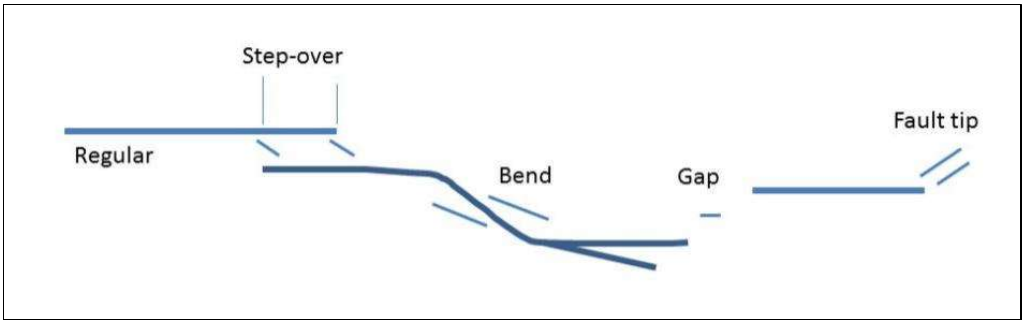

FIG 8. Basic glossary of geometric discontinuities along a principal fault (bold lines). Thin lines represent distributed ruptures with less displacement and continuity.

Thanks to the recent technological developments, the quality of the surface displacement datasets can be significantly improved in terms of data density, homogenization, and spatial resolution. For example, the fault displacement hazard initiative (FDHI) led by the University of California in Los Angeles is developing a database of discrete brittle slip and distributed inelastic strain measurements for several earthquakes with extensive datasets [63]. This database is structured after the Next Generation Liquefaction relational database [64], that will include a wide range of measurement types such as net slip, vertical throw and strike slip values, or point observations (from field measurements) and displacement profiles (from high-tech datasets), as well as site-specific data (e.g., surface geology, topography).

The development of future generation fault displacement models will be based on both, older data integrated with newer datasets, including field measurements, high-resolution and high-tech datasets. Developing site specific (non-ergodic) empirical relationships for fault displacement hazard assessment will require significant future work, including the need to enlarge the dataset to more cases in various seismotectonic settings (e.g., volcano-tectonic environment, intraplate context, reverse fault earthquakes). Following the classical approach defined in [58] both observation points and segment ruptures will have to be ranked in terms of on-fault versus off-fault and of secondary versus triggered slip because the SURE database includes a minimal level of interpretation concerning the ranking of ruptures (primary, secondary, triggered). Facing complex cases, the compiler will have to establish a justified framework. Referring to the surface faulting characteristics developed in Section 2.3, the primary rupture (also called principal rupture or on-fault rupture) is defined for further analyses (i.e., compilation of data to perform attenuation relationships) by the large continuity of ruptured fault portions, large displacement values and long-term evidence along it.

Alternatively, distributed or off-fault displacement evidence will be defined off the principal ruptures and can be subdivided into secondary and triggered ruptures. The latter occurs along remote (often pre-existing) faults and shows up generally small displacements. Secondary ruptures have generally little continuity and small displacement; they can be structurally associated with the principal rupture or not, but they are included within the crustal volume strained before and during the earthquake (the extension of which is for instance defined by the InSAR envelope). Examining recent cases, one could define 'subsidiary principal ruptures' in the 'secondary slip sets' because this reactivates large portions of cumulative fault but with lesser displacements (e.g., Laguna Salada fault during the 2010 M_W 7.2 El Mayor-Cucapah earthquake along the El Mayor Cucapah fault zone). In the reverse-fault earthquakes cases, secondary rupture can be associated with bending-moment or flexural slip (as during the 1980 M_W 7.0 El Asnam earthquake). Another issue when analysing the observations for developing empirical models is to define a distance metric for distinguishing off-fault rupture from the primary rupture. There are several alternatives that could be envisaged in the map point of view. Off-fault observation distance could be measured with the shortest distance to the major faults (case ‘yellow’ in Figure 5). When off-fault points or segments are located beyond the major fault tips, an option is to calculate the distance from the observation point to a projected and extended trace of the primary rupture (cases ‘green’ and ‘blue’ in Figure 5).

3. PROBABILISTIC FAULT DISPLACEMENT HAZARD ANALYSIS

PFDHA assesses the relationship between the amount of fault displacement that might occur at a site due to earthquake-related fault rupture and its probability of being exceeded. As stated in Section 1, PFDHA is a methodology that is recommended in SSG-9 [2] to evaluate fault displacement hazard for an existing nuclear installation.

In accordance with SSG-9 [2], displacements that need to be considered in PFDHA are described as follows:

> "In the probabilistic fault displacement hazard analysis, the following two types of possible displacements should be considered: (a) primary displacement, typically in the form of direct seismogenic fault rupture; and (b) secondary displacement (also called indirect or subsidiary displacement), typically associated with induced movement along pre-existing seismogenic slip planes (e.g. a triggered slip on an existing fault or a bedding plane from an earthquake on another fault) and non-seismogenic slip planes (e.g. localized fractures and weak clay seams). In addition, the displacement should generally be characterized as a three dimensional displacement vector, and should be resolved into components of slip along the fault trace and along the fault dip, with the resulting amplitude equal to the total evaluated slip (for a given annual frequency of exceedance and given fractile of hazard). The evaluation should address epistemic uncertainties adequately." (Ref. [2], para. 8.11)

In this publication, the term 'principal displacement' is used in a similar manner to the term 'primary displacement' in SSG-9 [2] and 'on-fault displacement' in some scientific literature. The term 'distributed displacement' encompasses the terms 'secondary displacement' in SSG-9 [2] and 'off-fault displacement' in some literature.

3.1. OVERALL METHODOLOGIES OF PFDHA

In PFDHA, the objective is to determine the displacements at a site given one or more exceedance probability levels, usually by first solving for its inverse, the probability of exceeding one or more target displacement values. The probability of exceedance, expressed as the annual exceedance frequency (exceedance rate), can be obtained by Eq. (1):

$$\lambda(D > D_0) = \alpha_{DE} P(D > D_0) \tag{1}$$

where $\lambda(D > D_0)$ is the annual exceedance frequency that a fault displacement D in an event exceeds D_0, D_0 is the level of a specific fault displacement, α_{DE} is the rate of displacement events on the fault, and $P(D > D_0)$ is the probability that D in an event exceeds D_0 .

Eq. (1) is applicable to both primary and secondary displacements as defined in [2].

Current PFDHA has defined two basic approaches for solving Eq. (1) that differ based on whether or not there are data at or near the site of interest to quantify α_{DE} and the exceedance probability distribution $P(D > D_0)$. The first approach, called 'displacement approach', relies on quantifying the rate of events and the exceedance probability distribution from analysis of paleoseismic data collected at or near the site. The displacement approach is also designated as 'direct approach' because it relies on the evaluation and interpretation of site-specific paleoseismic data for past earthquake displacements to understand the hazard. Unfortunately, it is practically challenging to conduct this approach due to limitations of directly observed data at the site of interest.

The second approach, called 'earthquake approach', is used when there are no reliable data from the site to quantify α_{DE} or $P(D > D_0)$ directly. The earthquake approach instead provides the rate of events and displacement exceedance probability distribution by estimating the locations, sizes and rates of future earthquakes at and near a site, and by estimating the frequencies that a particular earthquake will result in displacement at a site of a particular size. In this sense, the earthquake approach to PFDHA follows a methodology that is similar to standard probabilistic seismic hazard analysis (PSHA) for evaluating ground shaking hazards. Currently, the standard earthquake approach PFDHA relies on global empirical data to compensate for the lack of site-specific data and thus it is assumed that the ergodic assumption in probability theory is valid for earthquake processes. The ergodic assumption used in hazard studies [65] implies that the statistical properties of a process do not change from region to region, and any sample of the process from a region is completely representative of the process as a whole.

For both, the displacement and earthquake approaches, there are uncertainties in the rate of displacement events and the displacement exceedance probability distribution. These uncertainties include epistemic uncertainties, which are related to the limitations in our understanding of the earthquake phenomena. Examples of epistemic uncertainties for the displacement approach include uncertainties in the paleoseismic data regarding the rate of displacement events, or uncertainties in the amount of prior displacements. Examples of epistemic uncertainties in the earthquake approach include uncertainties in the earthquake locations, magnitudes and rates that might result in displacements at the site, and uncertainties in the displacement amounts that result from earthquakes of a certain size or distance from the site. Other uncertainties in PFDHA are related to the inherent variability of the phenomena. Examples of this type of uncertainty, which is called aleatory variability, include the variability in the displacement amount from event to event at a site which defines the displacement probability distribution. In PFDHA, as in other probabilistic analyses of rare phenomena, capturing these epistemic and aleatory uncertainties is an important element in the hazard assessment. A more detailed description of the uncertainty assessment in PFDHA is given in Section 3.4.1.

3.1.1. Displacement approach

In the case where there is sufficient site information about the fault displacement history (amount of displacement per event and age of events), the probability of displacement exceedance at the site can be solved by Eq. (1). This equation might be used for both principal and distributed faults. The simplicity of Eq. (1) belies the fact that a proper analysis requires the availability of a large number of displacement observations that is seldomly achieved at a single site. This might be circumvented by applying some assumptions or approximations. In that case, $P(D > D_0)$, can be estimated by integrating a probability density function obtained by statistical analysis of the geological data at the site.

If an average recurrence interval, R_{ave}, of displacement events on a fault can be calculated from geological information, the rate α_{DE} can be obtained by Eq. (2):

$$\alpha_{DE} = \frac{1}{R_{ave}} \tag{2}$$

if R_{ave} cannot be obtained, it is possible to estimate α_{DE} using Eq. (3):

$$\alpha_{DE} = \frac{SR}{D_E} \tag{3}$$

where SR is the slip rate of the fault of interest and D_E is the average amount of displacement on the fault.

Angell et al. in 2003 [66] demonstrated an example of the displacement approach in PFDHA for submarine pipelines in the Gulf of Mexico using seismic and geological data. The average event rate was calculated using Eq. (3). The displacement approach was also used in the Yucca Mountain nuclear waste repository project in Nevada, USA, as explained in Section 4.1.

3.1.2. Earthquake approach

Even with the above approximations, there are often not enough site-specific data to use the displacement approach. In these cases, a model of earthquake occurrence on nearby faults is used (earthquake approach), and current practice relies partially, or entirely, on observations from other fault systems (the ergodic assumption). Analogous to PSHA, the earthquake approach uses an integration over a set of earthquakes distributed on the fault, replacing the simple event rate α_{DE} in Eq. (1) with an integration over magnitude and location-dependent event rate:

$$\alpha\left(m_{\min}\right)\int_{m,s} f_{M,S}\left(m,s\right)dmds \tag{4}$$

where $\alpha(m_{min})$ is the overall rate of events with magnitude larger than a minimum magnitude (m_{min}) considered in the analysis and $f_{M,S}(m,s)$ is a probability density function that describes the magnitude m, that might occur along the source at a distance s from the end of the fault.

Similarly, $P(D > D_0)$ in the earthquake approach is expanded with a conditional probability of displacement exceedance based on predictor variables related to the surface rupture characteristics and the location and dimension of the site of interest relative to the rupture. The geometric relationship developed in [27] for strike-slip earthquakes is shown in Figure 9. Their empirical model describes the conditional probability of the displacement exceedance as (see Section 3.3.1):

$$P\left[D > D_0 \middle| l/L, m, D \neq 0\right] \tag{5}$$

where l/L is the along-fault distance ratio (l is the distance measured from the nearest point on the fault rupture to the closest end of the rupture and L is total rupture length) and $D \neq 0$ is the condition that the earthquake produces surface-fault displacement at the site.

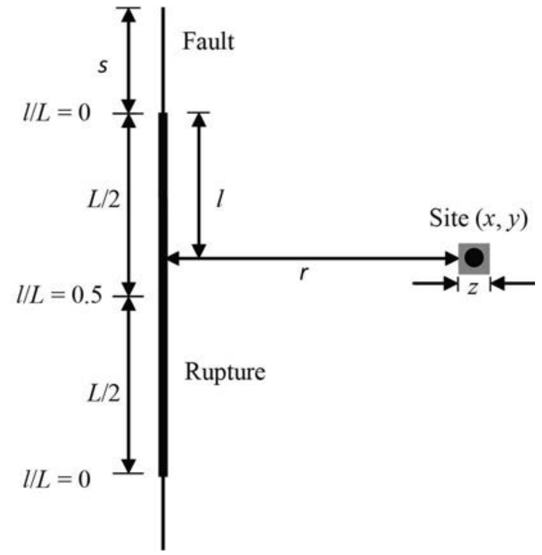

FIG 9. Definitions of variables used in the fault rupture hazard analysis: x and y are site coordinates; z is dimension of the area (z^2) considered in calculating the probability of fault displacement; r is closest distance from the site to mapped fault trace; l/L is on-fault distance ratio, where l is distance measured from the nearest point on the rupture to the closest end of the rupture and L is total rupture length; and s is distance from the end of the rupture to the end of the fault (from [27] whit permission).

Of course, alternative parameterizations are possible and future empirical and/or physics-based models (see Section 3.3.4) can be introduced here with alternative predictor variables.

Since the integration in Eq. (4) is over surface ruptures that are distributed on a fault, additional factors need to be added to the original Eq. (1) to account for the fact that not all surface ruptures will affect the site. First, not all earthquakes break the surface, and thus the probability that a fault produces any surface rupture ($sr \neq 0$) might need to be defined. A simple, magnitude-dependent distribution for this probability is:

$$P\left[sr \neq 0 \middle| m \right] \tag{6}$$

Although other predictor variables such as style of faulting, crustal thickness and earthquake nucleation depth might be considered as well (partially described in Appendix II). If the earthquake does break the surface, there is a separate probability that the rupture crosses the site of interest ($D \neq 0$), as inferred in Eq. (5). Using the geometric definitions in Figure 9, this rupture probability might be defined as a function of footprint dimension z and its perpendicular distance r from the mapped principal fault:

$$P\left[D \neq 0 \middle| z, r, sr \neq 0 \right] \tag{7}$$

As with Eqs (5) and (6), the predictor variables in Eq. (7) might be expanded based on available data and models. The example forms shown here reflect the approximate scheme developed in [27].

When the above replacements and additions are applied and integrate over event magnitude and location distributions for the earthquake approach, Eq. (1) then transforms into:

$$\begin{aligned}\lambda\left(D>D_0\right)_{xyz}&=\alpha\left(m_{\min}\right)\int_{m,s}f_{M,S}\left(m,s\right)P\left[sr\neq 0\middle|m\right]\\&\times\int_{r}P\left[D\neq 0\middle|z,r,sr\neq 0\right]\\&\times P\left[D>D_0\middle|l/L,m,D\neq 0\right]f_R\left(r\right)drdmds\end{aligned}\tag{8}$$

where $f_R(r)$ is a probability density function that characterizes the perpendicular distance from the site to all potential ruptures. See Section 3.3.2 for detailed discussions.

Thus far, there has been no distinction drawn between principal fault displacement and distributed fault displacement. Adopting the capital letters D and D_0 for principal displacement and lower case letters d and d_0 for distributed displacement in accordance with [27], one might adopt Eq. (8) as an example form of the earthquake approach for principal fault PFDHA. The annual exceedance frequency for the distributed fault displacement hazard has a similar general form as Eq. (8) and might be expressed as follows:

$$\begin{aligned}\lambda\left(d>d_0\right)_{xyz}&=\alpha\left(m_{\min}\right)\int_{m,s}f_{M,S}\left(m,s\right)P\left[sr\neq 0\middle|m\right]\\&\times\int_{r}P\left[d\neq 0\middle|z,r,sr\neq 0\right]\\&\times P\left[d>d_0\middle|r,m,d\neq 0\right]f_R\left(r\right)drdmds\end{aligned}\tag{9}$$

As stated above, the general forms shown in Eqs (8) and (9) might not contain some detailed expressions or predictor variables introduced by other authors. Therefore, when performing a PFDHA, the methodology needs to be selected after the consideration of the seismotectonic setting and the available data, models and methods. For instance, Takao et al. in 2013 [29] introduced an additional conditional probability related to rupture segments based on the observation that the ratio of surface earthquake fault length to earthquake source fault length depends on the magnitude of the earthquake. Probability density functions and conditional probabilities proposed in [29, 36, 58, 59, 61] for a variety of faulting types and seismotectonic environments are documented in Appendix II.

3.2. SOURCE CHARACTERIZATION

Both traditional PSHA and the earthquake approach of PFDHA have terms that might be categorized as either seismic source characterization or as characterization of the hazard phenomena: ground motion characterization in the case of PSHA and fault displacement characterization for PFDHA. Whereas in PSHA seismic source characterization involves the development of both fault sources (well defined planar sources of earthquakes), and areal seismic source zones (earthquakes produced from crustal volumes with non-specified, or semi-randomized locations), PFDHA for this publication uses only fault sources with the potential to rupture the ground surface. Seismic source characterization for fault sources typically consists of defining the set of faults that might contribute to the hazard at the site of interest and developing the magnitude-recurrence distribution and rupture location distribution as defined in Eq. (4).

In this publication, the data needs of the displacement approach under seismic source characterization (Section 3.2.1) are addressed for convenience since the data are geological in nature. Then in Section 3.1.2 the data needs and methods to satisfy Eq. (4) will be discussed. Fault displacement characterization (Section 3.3) discusses data, models, and methods to satisfy Eqs (4), (5), and (6) or their equivalents.

3.2.1. Direct observations

Direct observations are geological data from fault trench studies and other field observations at the site that directly or indirectly pertain to past earthquake occurrences. For instance, the rate of displacement events, α_{DE}, in Eq. (1) might be obtained by dating observed displacement events, estimating a mean recurrence interval and its uncertainty, and solving Eq. (2). Alternatively, the rate can be computed simply as the slip rate divided by the average displacement per event (Eq. (3)) with an appropriate propagation of uncertainties in both the slip rate and average displacement terms. The conditional probability of displacement exceedance, $P(D > D_0)$, can be obtained by measuring the amount of displacement for many events at a site. The input for the displacement approach can therefore be as simple as the geological displacement measurements and timing of the displacement events.

In practice, geological observations of past displacement events often are limited in number and are subject to different interpretations by experts that might result in significant differences in the resulting hazard. In developing the displacement approach, it is important to be mindful of the quantity and quality of data available to constrain displacement models, and to consider alternative statistical or geological models of the fault displacement phenomena affecting the site. Such uncertainties might be captured using a logic-tree approach that clearly identifies epistemic uncertainties in available data, alternative models that explain the data, and resulting uncertainties in the correct values for the terms in Eq. (1). Angell et al. in 2003 [66] present an example of the use of geological models to help understand epistemic uncertainty in the mechanism of faulting affecting an offshore facility. Hecker et al. in 2013 [67] present an example of a statistical model for aleatory variability in fault displacement at a site based on an analysis of paleoseismic data from various tectonic environments and styles of faulting.

3.2.2. Source characterization for the earthquake approach

As stated before, in the earthquake approach there is a large overlap between PSHA and PFDHA, since both use earthquake distributions in time, space and magnitude to develop the hazard models. This is reflected in the commonality between the input parameters for both methods, such as recurrence models, earthquake rates and fault geometry. In fact, if a particular hazard evaluation involves a ground motion and a fault displacement component, it is desirable that identical input parameters are used wherever there is commonality. In some cases, higher precision is needed in defining certain parameters for PFDHA compared to PSHA, such as the fault geometry.

For the earthquake method, the seismic source characterization consists of two main components: fault parameters and the earthquake recurrence model.

3.2.2.1. FAULT PARAMETERS

The fault parameters in their simplest form consist of a fault type (i.e., strike-slip, normal, reverse), surface trace, dip and downdip fault width often based on seismogenic thickness. The rake of the slip vector is often not prescribed in PSHA, but it is of importance in PFDHA if the response of the structure is strongly dependent on direction of the slip (see discussion in Section 3.4.3). Secondary faulting is an important factor in the analysis of the displacement hazard and thus precise and comprehensive mapping of surface ruptures is essential for better constraints on probabilistic fault displacement hazard. Also, to develop more refined empirical relations of the surface displacement, and to validate numerical simulation approaches, it is important to obtain information on the physical subsurface conditions at the rupture, as these are very likely to affect the characteristics of the fault at the surface.

3.2.2.2. Maximum magnitude

The basic measure of an earthquake size is the seismic moment M_0 (see IAEA Safety Report Series No. 89 [68]) in N·m, and the most commonly used earthquake magnitude M_W is the standard measure for earthquake size and is used throughout this publication. Other instrumental magnitude scales exist, and in the case where the seismicity rate is based on earthquake catalogue data, the correct conversions to M_W might need to be applied [69–71].

In the three models of magnitude-frequency distribution mentioned in following Section 3.2.2.3, the maximum magnitudes for faults are typically derived using source-scaling relations from either rupture length or rupture area and infrequently average or maximum displacement. Wells and Coppersmith in 1994 [5], Leonard in 2010 [72], and others (Figure 10) have developed a comprehensive set of relations between rupture length, rupture width, rupture area, and displacement (average and maximum) with magnitude for crustal earthquakes. These relations have been developed for normal, reverse and strike-slip fault types.

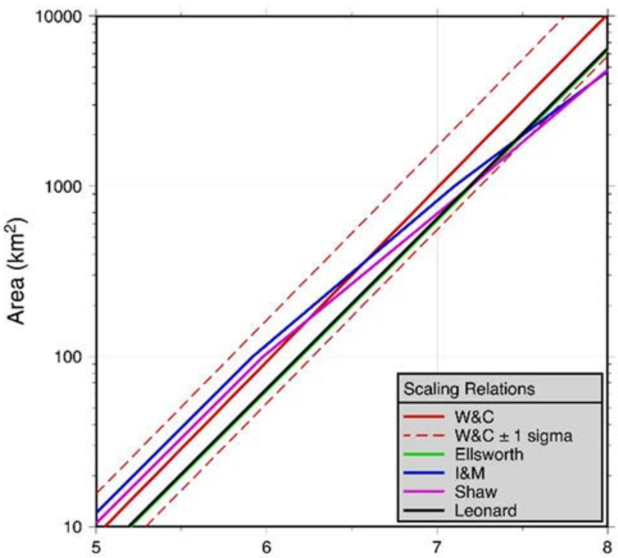

FIG 10. Comparison of several area-magnitude scaling relations for crustal earthquakes. W&C – Wells and Coppersmith [5], Ellsworth [73], I&M -Irikura and Miyake [74, 75], Shaw [76], Leonard [77].

Almost all scaling relations can be reduced to a form like $M_W = a \cdot \log X + b$, where X can be displacement, rupture area, rupture length or rupture width. One subset of scaling relations are the so-called self-similar models, where the displacement and fault dimensions scale are proportionally with seismic moment, which means that the static stress-drop is independent of magnitude. In this case, the constant a is 1. The Leonard model [72] is an example of self-similar scaling relations. Several scaling relations assume that downdip fault width saturates for large magnitudes, and therefore consist of two parts. These include the Irikura and Miyake relationship [74, 75] for Japanese intraplate earthquakes and the Hanks and Bakun relationship [78] for continental strike-slip earthquakes. For smaller magnitudes, the relationship is self-similar whereas for larger events, the parameter a becomes 4/3. The break in the relationship is often explained as being due to the fault width saturating as it equals the thickness of the seismogenic crust, and has also been inferred by others [79, 80].

Stirling et al. in 2013 [81] evaluated many of the published scaling relationships and made recommendations regarding the quality and applicability of the various relations. They note that tectonic environments and style of faulting are important factors and they must be taken into account in choosing the relations for a given purpose.

Some cautions need to be taken when applying these scaling relations for PFDHA. Whereas in PSHA, the magnitude is the defining parameter for the ground motions, in PFDHA it is usually the average displacement, derived from the magnitude. Most scaling relations are not internally consistent and therefore, if the magnitude is determined by the rupture area the average displacement that is then computed from the magnitude might not be consistent with the original scaling data.

3.2.2.3. Earthquake recurrence

In PSHA, the earthquake occurrence is usually assumed as a Poisson process, where the probability of an event occurrence can be calculated using the mean recurrence interval and is independent of the time since the last event on the same fault occurred [82]. More recently, time-dependent occurrence models have become available [83] and have been used for at least some fault sources that have well-documented rupture histories [84]. Given that sufficient information of the rupture history of a capable fault is available, one could argue that for PFDHA, a time-dependent model might be more accurate since the hazard is dominant by the identified capable fault rather than by diffuse seismicity. However, since PFDHA for nuclear facilities will often be applied to faults where the detailed history is relatively unknown (since well known capable faults are typically avoided) or where the recurrence times are very long (for the very same reason), it is appropriate to use time-independent models in most cases.

Whether a time-independent or time-dependent approach is taken in PFDHA, the estimates of earthquake recurrence are at the core of a PFDHA. Recurrence estimates consist of two main elements: the magnitude-frequency distribution and the overall moment rate.

Magnitude-frequency distributions

Magnitude-frequency distributions (often called recurrence relations) describe the earthquake rate as a function of the magnitude (Figure 11). There are three models commonly in use to define the distribution of earthquake magnitudes with which the strain on an earthquake source is released: the Gutenberg-Richter exponential relation [85], the characteristic earthquake model [86, 87], and the maximum magnitude model [88]. These models are shown in Figure 11.

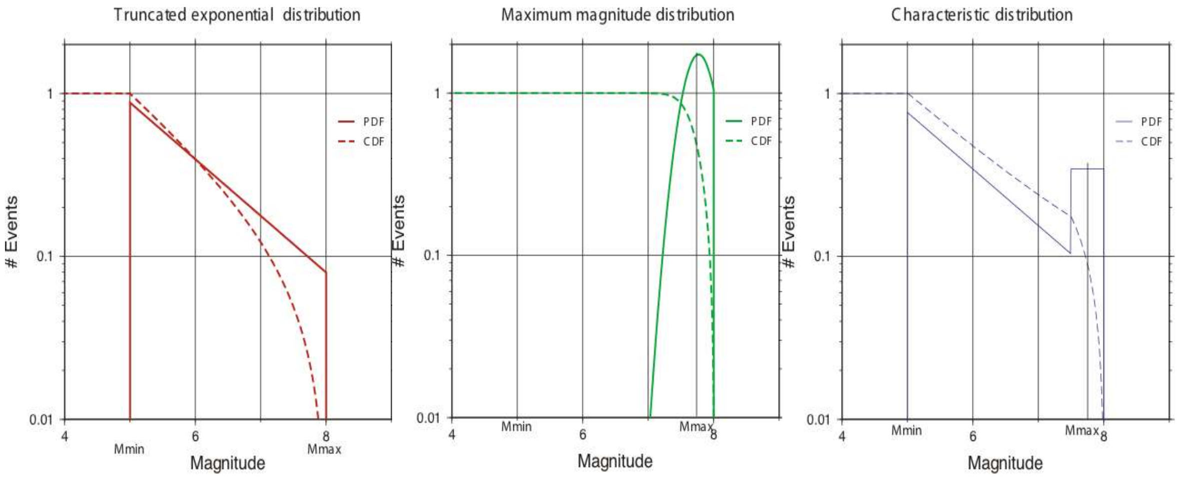

FIG 11. Probability density function (PDF) and cumulative density function (CDF) of the Gutenberg-Richter truncated exponential distribution, the maximum magnitude distribution and the characteristic distribution.

It appears that the characteristic and maximum magnitude models are more appropriate when describing the seismicity on individual faults, whereas the Gutenberg-Richter relation is more applicable to areal source regions, or ensembles of multiple source zones [87], although this is observation still being debated for faults like the San Andreas fault [89].

Moment rate

Magnitude-frequency distributions provide the relative contribution of magnitudes of the recurrence model and need to be scaled so that they conform to input deformation rates. There are several ways that overall event rates are defined as input: the simplest are by directly specifying recurrence intervals in a maximum-magnitude model or applying observed *a*- and *b*-values from a catalogue analysis into a Gutenberg-Richter model. For fault sources, the recurrence rates are often derived from fault slip rates. In this case, the magnitude-frequency distributions are computed through moment balancing [90]. In this procedure, the slip rates are first transformed into moment rates on the fault by multiplying the slip rates with the fault area and shear modulus. This moment rate is then used to scale the overall magnitude distributions to conform to the input slip rates.

3.2.2.4. Earthquake recurrence intervals and slip rates

For capable faults, the activity rate of the maximum earthquakes anchors the magnitude-frequency distribution. This activity rate is expressed either in terms of recurrence intervals (inter-event times) or fault slip rates. Slip rates are calculated by dividing the amount of co-seismic displacement by the time period over which that displacement has occurred. Recurrence intervals and slip rates are obtained through a variety of paleoseismic techniques with paleoseismic trench studies and age-dating of the geological units observed in the trench. If multiple earthquakes are exposed in the trench and they can be dated, then the recurrence intervals can be estimated. The use of recurrence intervals in PSHA (and PFDHA) is superior to using slip rates, because the latter incorporate unknown open-ended time periods and if the fault exhibits the temporal clustering, the slip rates might vary through time [91]. In addition to trench studies, slip rates can also be estimated based on measurements of fault displacement using dated surficial deposits or geomorphic features. Measurements over different time periods at multiple locations will provide estimates of the epistemic uncertainties in the slip rates. More detailed descriptions of fault recurrence rates can be found in IAEA-TECDOC-1767 [92].

3.3. FAULT DISPLACEMENT PREDICTION MODELS

Fault displacement prediction models are essential for PFDHA. These include models for: (1) the probability of having surface fault displacement given that an earthquake of specified magnitude occurs; (2) the probability of having a displacement on a principal fault over a specified area given that an earthquake of certain magnitude occurs with a surface rupture; (3) the probability of having a displacement at a distance from the fault over a specified area given the earthquake occurs; and (4) the probability that either a principal or distributed fault displacement exceeds some level within a specified area, given that an earthquake of a specified magnitude occurs with a surface rupture. To date, these models have been empirically based but physics-based numerical simulations are likely to be used in the future (see Section 3.3.4).

3.3.1. Empirical methods

Surface rupture is strongly dependent on the type of faulting, as well as on the details of the structural character of the fault. For normal faulting, the distribution of a rupture at the surface, including secondary displacement, was analysed and included in the empirical relations in [58]. Similarly, Petersen et al. in 2011 [27] developed models for strike-slip faults, Takao et al. in 2013 [29] quantified secondary displacement for a mix of mechanisms, and Nurminen et al. in 2020 [59] for reverse faults. Boncio et al. in 2018 [93] analysed surface fault zone widths for thrust faults and found that the character of the thrust faults, whether they are ‘simple’ or part of some flexural or bending moment structure, makes a big difference on the width distributions.

At this point, the type and character of faulting in the empirical relations does not extend any further than the three main categories, strike-slip, normal and thrust faulting. However, recent studies, such as [93], certainly point out that the possibility of a more refined specification of the surface faulting based on the structural character of the faulting, especially for thrust faults.

The probability of exceeding a specified displacement is calculated using empirical attenuation relationships between fault displacement and predictor variables such as location on or off a fault. Empirical models have been developed based on statistical analyses of available data from field measurements. Model equations, coefficients, and plots of data distribution are documented in Appendix II, including models developed in [58].

Existing empirical models for off-fault displacement have been developed based on offset displacements measured on discrete features far from the primary rupture. Discrete displacement might account for only a portion of the total off-fault deformation associated with an earthquake. Significant amount of non-discrete deformation can occur and can be damaging to structures built on top of the deformation zone. The American Nuclear Society Standards Committee Working Group ANSI/ANS-

2.30 [94] distinguishes discrete surface fault ruptures from tectonic surface deformation and provides guides for probabilistic hazard assessments for both. Recent applications of remote sensing techniques and optical image correlation can provide comprehensive characterization and quantification of total coseismic slip and off-fault strain distribution [95, 96]. Once incorporated, these new techniques would significantly improve the probabilistic assessment of hazards associated with co-seismic surface fault displacement, as well as co-seismic tectonic deformation.

Probability of surface rupture

The probability of a surface rupture, $P[sr \neq 0|m]$ in Eqs (8) and (9), is an important part of the empirical equations for both principal and distributed displacement hazards. Currently, several of such functions have been developed by different authors (Figure 12). Wells and Coppersmith in 1993 [28] used a logistic model and developed model coefficients using a worldwide data set of all slip types. Youngs utilized the Wells and Coppersmith logistic model and developed model coefficients for normal faults using data from [35]. Takao et al. in 2013 [29] also developed such a relationship for all fault mechanisms in Japan, and Moss and Ross in 2011 [36] developed relations for thrust faulting (Figure 12). The relation for thrust faults gives much lower probabilities of surface rupture than the relations for other fault types. This might be due to thrust earthquakes being more prone to diffusion of the displacement toward the surface, but it might also be caused by the fact that the thrust database includes events on so-called blind thrusts, which never reach the surface. If that is the case, then the use of the relations for thrust faults that are known to break the surface might lead to an underestimation of the hazard. Therefore, a careful check and scrutiny process of the database from a given empirical model are important before applying an empirical relationship. This process would provide the basis to evaluate the applicability of the empirical model to the target site.

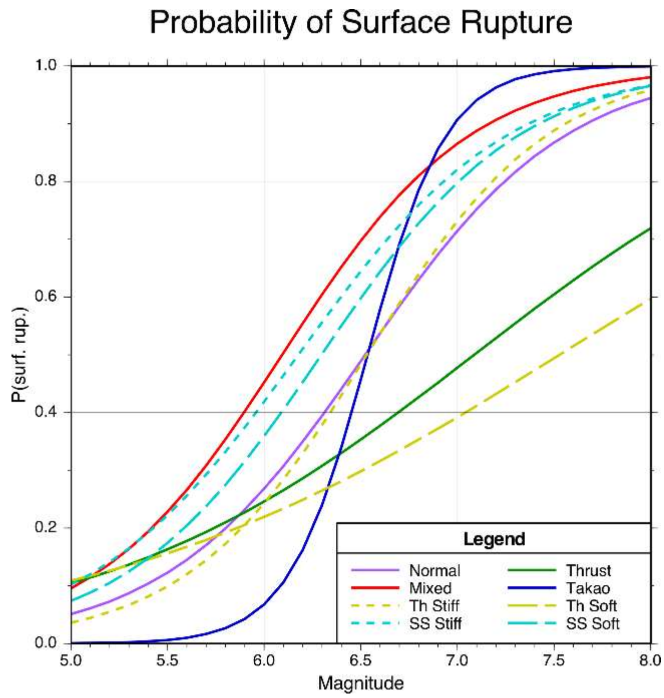

FIG 12. Probability of surface rupture given magnitude for different earthquake mechanisms (red, Petersen et al. [27], all types mixed), (green, Moss and Ross [36], reverse faults), (purple, Youngs et al. [58], normal faults) and a combined set from Japan (blue, Takao et al. [29], reverse and strike slip). The dashed lines show the relations from [41], which differentiate according to the average topographic slope as a proxy for soil properties.

3.3.1.1. Principal fault displacement models

Probability of non-zero displacement

The probability of non-zero displacement, $P[D \neq 0|z,\ r,\ sr \neq 0]$ in Eq. (8), represents the distribution of surface ruptures on the principal fault, and is expressed as the ratio of cells of the rupture on the principal fault to the total number of cells in [58]. This accounts for discontinuities of surface rupture along the fault and the probability of rupture reaching the site. Takao et al. in 2013 [29] developed a piecewise linear function for this probability term.

Conditional exceedance probability

The displacement exceedance probability, $P[D > D_0 \mid l/L,\ m,\ D \neq 0]$ in Eq. (8), is a conditional probability of displacement exceedance. It is determined by integrating a probability density function characterizing natural variability in the magnitude of fault displacement. Often, fault displacement is normalized to remove the dependence on the earthquake magnitude. The gamma, or Weibull distribution is used for principal displacement (*D*) normalized by average displacement (*AD*). The beta distribution is used for displacement normalized by maximum displacement (*MD*). Parameters of each probabilistic distribution are defined relative to the position along the fault or by functions characterizing spatial distribution of displacement along the fault. When the displacement is normalized, the exceedance probability is calculated by convolving the probability distribution for *AD* or *MD* with the probability distribution of *D/AD* or *D/MD* in the hazard integration.

Wesnousky in 2008 [57] pointed out that the asymmetric displacement distribution is better than the symmetric distribution. Hemphil-Haley and Weldon in 1999 [97] indicated principal fault displacement tapers off the ends of the rupture. Youngs et al. in 2003 [58], Moss and Ross in 2011 [36], and Takao et al. in 2013 [29] assume a symmetric fault displacement along a fault.

Petersen et al. in 2011 [27] developed three alternative regression models in which the displacement is defined as a function of the earthquake magnitude and the on-fault distance: (1) the bilinear model (consistent with their data set); (2) the quadratic model (consistent with asymmetric displacement distribution observed in [57]); and (3) the elliptic model (consistent with another displacement distribution in [55, 98]). For strike-slip faults, the predicted displacement decreases towards the end of the rupture, especially within the final 20 to 30% of the total rupture length at each end. Petersen and Chen in 2011 [99] compared the published data. They found the data for reverse faults and those from Japanese are similar to the data for strike-slip faults in the centre portion of the fault, but they differ near the end of the fault (Figure 13).

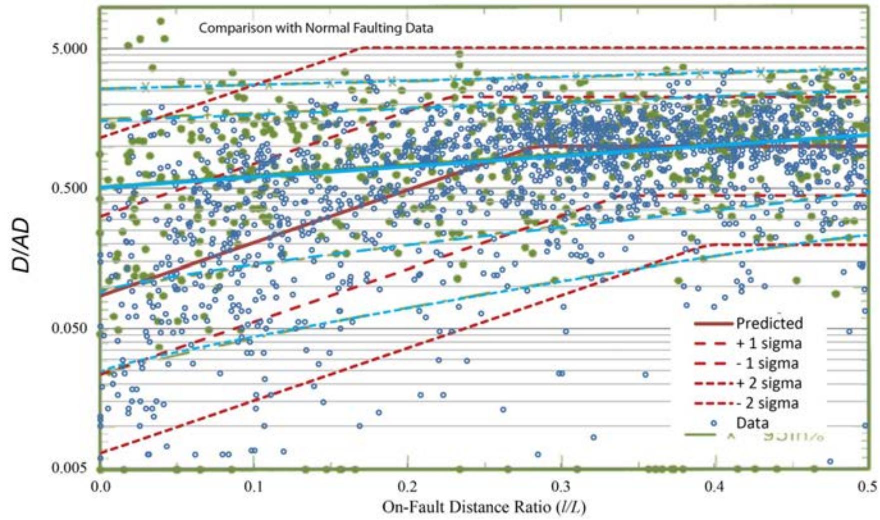

FIG 13. Comparison of reverse (green circles) and strike-slip (blue circles) D/AD data for global earthquakes. Strike-slip fault regressions are shown with red lines [27]. Reverse faulting data are from [36]. (from [99] whit permission)

3.3.1.2. Distributed fault displacement models

The occurrence of distributed fault displacement tends to depend on faulting mechanism. Field observations of surface faulting suggest that down-warping on the hanging wall block during reverse faulting earthquakes might cause tension fissures on the surface. Subsidence of the hanging wall block from normal faulting might lead to secondary fractures. Youngs et al. in 2003 [58] and Nurminen et al. in 2020 [59], who compiled the normal and reverse fault data, developed distributed fault displacement models on both sides of the fault. In contrast, Petersen et al. in 2018 [27], who compiled the global strike-slip fault data, do not distinguish opposing sides of the fault.

Probability of non-zero displacement

The probability of distributed fault displacement, $P[\, d \neq 0 \mid r, z, sr \neq 0]$ in Eq. (9), is evaluated as the ratio of the number of cells that contain ruptures off the principal fault to the total number of cells at a given fault distance in [58] and [27]. Each raster map of distributed fault ruptures is discretized into a uniform grid with a chosen cell size. The number of cells containing distributed faulting divided by the total number of cells at a given fault distance gives a measure of the rate of occurrence of distributed ruptures at that distance. The cell size (a proxy for footprint size of engineering structure) is critical in calculating the probability of a rupture at a site. Smaller footprints have lower probabilities for ruptures occurring within their boundaries than larger footprints. Youngs et al. in 2003 [58] and Takao et al. in 2013 [29] used a set 500 m × 500 m cell size with a logistic function. Petersen et al. in 2011 [27] used square cells with cell sizes ranging from 25 to 200 m. In their model, the probability of a distributed rupture decreases with increasing fault distance, following a power function. Takao et al. in 2014 [61] used square cells with cell sizes ranging from 50 to 500 m and a logistic function to characterize the probability of a distributed rupture. A distributed fault displacement model for a thrust faulting is not yet available.

Boncio et al. in 2018 [93] considered computing the probability of a distributed rupture only in sections of the principal fault that have distributed ruptures by compiling data from 11 well-studied past thrust earthquakes ($5.4 \leq M_W \leq 7.9$). Fault displacements on splay faults or on other faults are also included in their analysis as sympathetic distributed fault displacements. Their analysis distinguishes the footwall side from the hanging wall side. Their results indicate different rupture zone widths on the hanging wall and on the footwall (i.e., rupture occurrence is asymmetric about the principal fault). The average ratio of footwall-to-hanging wall rupture zone widths is about 1:2. They also found a positive relation between the earthquake magnitude and rupture width.

In [59] the spatial distribution parameter of distributed fault ruptures is approached by ‘slicing’, as an alternative to ‘gridding’, in order to balance the relative incompleteness of the surface rupture maps for the historical cases used in the empirical analysis. The area off the primary fault is divided into slices of 10 m width parallel to the primary fault strike, and slices that contain at least a partial distributed rupture segment are counted. The frequency-distance distributions of distributed ruptures are the sum of slices that include at least a partial distributed displacement segment, normalized to the number of events in the database. The displacement analysis is done based on the vertical slip, which is the metric that is measured the most frequently in the field.

Conditional exceedance probability

The displacement exceedance probability, $P[d > d_0 \mid r, m, d \neq 0]$ in Eq. (9), is obtained by integrating a probability density function characterizing the distribution of secondary displacement data. The distributed displacement data are modelled under the assumption of decreasing displacement with increasing distance from the principal fault. Youngs et al. in 2003 [58] define the distance to be the closest distance to the rupture. Petersen et al. in 2011 [27] separate the variable s, distance from end of the fault, from r, distance from the principal fault. Power or exponential functions are used. Nurminen et al. in 2020 [59] used the distance from a point with a measured vertical surface slip along a distributed rupture to the nearest primary fault trace. Both [58] and [59] provided the distribution fault displacement attenuation functions for normal and reverse faults, respectively, that differ for the footwall and hanging wall sides. In contrast, [27] and [29] established attenuation relationships without distinguishing between footwall and hanging wall.

Similar to principal attenuation relationships, distributed fault displacement (d) often is normalized by MD or AD of the principal fault displacement. Petersen et al. in 2011 [27] estimated a power function attenuation for normalized distributed fault displacement (d/AD). Both [58] and [29] estimated attenuation using an exponential function. Moreover, [58] indicated greater amplitude in the hanging wall compared to the footwall. The calculation of exceedance probability is described in Appendix II.

3.3.2. Principal rupture location uncertainty

PFDHA starts with a high-quality fault map. Epistemic location uncertainty is specific to fault maps used in PFDHA analyses. Most maps have location errors, and fault features are not always well recognized. The location and spatial complexity of faults directly affect the amount and distribution of predicted fault displacement and are essential, but difficult, aspects of PFDHA. Surface ruptures from historical earthquakes commonly deviate from fault traces mapped prior to the earthquakes. In many cases, historical surface ruptures are more widespread and complex than mapped faults. Large uncertainties are associated with surface rupture from future earthquakes.

The uncertain nature in the location of surface rupture from future earthquakes (location uncertainty) is captured using a probability distribution, $f_R(r)$, in Eqs (8) and (9) for hazard integration following the approach in [27]. This approach defines an empirical model for $f_R(r)$ that includes the dependence of fault displacement hazard on the accuracy and complexity of mapped fault traces. Uncertainty in rupture location was considered in the PFDHA study for the Krško Nuclear Power Plant, as described in Section 4.3. Chen and Petersen in 2011 [100] applied the approach to calculate probabilistic fault displacement hazards and develop displacement hazard maps for the M_W 7.8 ShakeOut earthquake scenario [101] on the southern San Andreas fault. They also developed a strategy to partition probabilistic displacement among multiple mapped branching faults.

This section summarizes data and models to quantify rupture location uncertainty and model implementation in PFDHA. It also provides examples of partitioning estimated displacement among complex branching fault traces.

3.3.2.1. Rupture location uncertainty

Petersen et al. in 2011 [27] compared locations of observed surface ruptures with fault traces on fault maps produced prior to the earthquakes for eight large surface-rupturing strike-slip earthquakes. They quantified location uncertainty by systematically measuring distances from observed surface ruptures to the corresponding previously mapped fault traces as illustrated schematically in Figure 14.

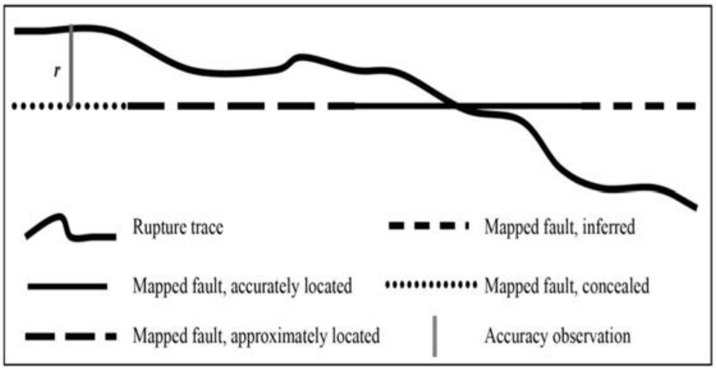

FIG 14. Diagram showing distance (r) between observed surface rupture and fault trace mapped prior to the earthquake producing the surface rupture (reproduced with permission from [27]).

Measured distance (r) data were grouped based on accuracy of previously mapped fault traces following the categorization used in California's Alquist-Priolo (A-P) earthquake fault zone maps (http://www.conservation.ca.gov/cgs/Pages/Program-SHP/Alquist-Priolo.aspx), namely accurately located, approximately located, inferred, and concealed fault traces. Summary statistics (means and standard deviations) indicate smaller location discrepancies for more accurately mapped fault traces (Table 1). Re-centring distance statistics to mapped fault locations produces zero mean and two-sided standard deviation (σ) in accordance with Eq. (10):

$$\sigma = \sqrt{\sigma'^2 + \mu^2} \tag{10}$$

where σ' is one-sided standard deviation and μ is mean.

TABLE 1. MAPPING ACCURACY SUMMARY: DISTANCE (R) MEASURED FROM MAPPED FAULT TRACE TO OBSERVED SURFACE RUPTURE (From [27]).

Mapping accuracy	Mean (m)	One-sided standard deviation (m)	Two-sided standard deviation on fault locations (m)
All	30.6	43.1	52.9
Accurate	18.5	19.5	26.9
Approximate	25.2	35.9	43.8
Concealed	39.4	52.4	65.5
Inferred	45.1	57.0	72.7

Petersen et al. in 2011 [27] further divided measured distance data for the concealed and inferred categories into subgroups based on whether mapped fault traces are simple or complex. Complex fault traces occur where the fault changes strike, splays, steps over to a new trace, or terminates. Summary statistics indicate smaller location discrepancies for simple fault traces (Table 2).

TABLE 2. COMPLEXITY SUMMARY: DISTANCE (R) MEASURED FROM MAPPED FAULT TRACE TO OBSERVED SURFACE RUPTURE (From [27]).

Complexity	Mean (m)	One-sided standard deviation (m)	Two-sided standard deviation on fault (m)
Simple – concealed	36.6	45.0	61.9
Simple – inferred	31.5	38.3	49.6
Complex – concealed	90.3	73.1	116.2
Complex – inferred	83.2	81.3	116.4

The lateral extent of future surface rupture around a previously mapped fault can be estimated for a chosen probability distribution based on the summary statistics in Tables 1 and 2. For example, assuming distance data (r) follow a normal distribution, there are about 95% and 64% probabilities that surface rupture from future earthquakes will occur within 54 m (two standard deviations) and 27 m (one standard deviation), respectively, on either side of an accurately mapped fault. A normal distribution (with truncation) is assumed in [27] for distances (r) between observed ruptures and mapped fault traces. Area under the normal probability density function over foundation dimension or dimension of area of interest is used to scale displacement exceedance rate in PFDHA. This approach produces a non-zero exceedance probability of a displacement (and non-zero principal displacement) near the mapped fault. The distribution of exceedance probability across the fault for a given displacement resembles a normal distribution because of the normality assumption in characterizing location uncertainty. Similarly, the distribution of displacement with a given exceedance probability across the fault also resembles a normal distribution, exhibiting a bell-shaped profile centred on the mapped fault. Figure 15 illustrates the probability and displacement profiles across a mapped fault for a hypothetical M_W 7 earthquake occurring on average every 140 years. Figure 15(a) shows 50-year exceedance probability profiles for four selected displacement levels for an accurately mapped fault. Figure 15(b) shows displacement profiles with 10% exceedance probability in 50 years for the four mapping accuracy categories, illustrating strong effects of mapping accuracy on hazard estimates. Figure 15(b) is a modified version of Figures 8(c) and 8(g) in [27].

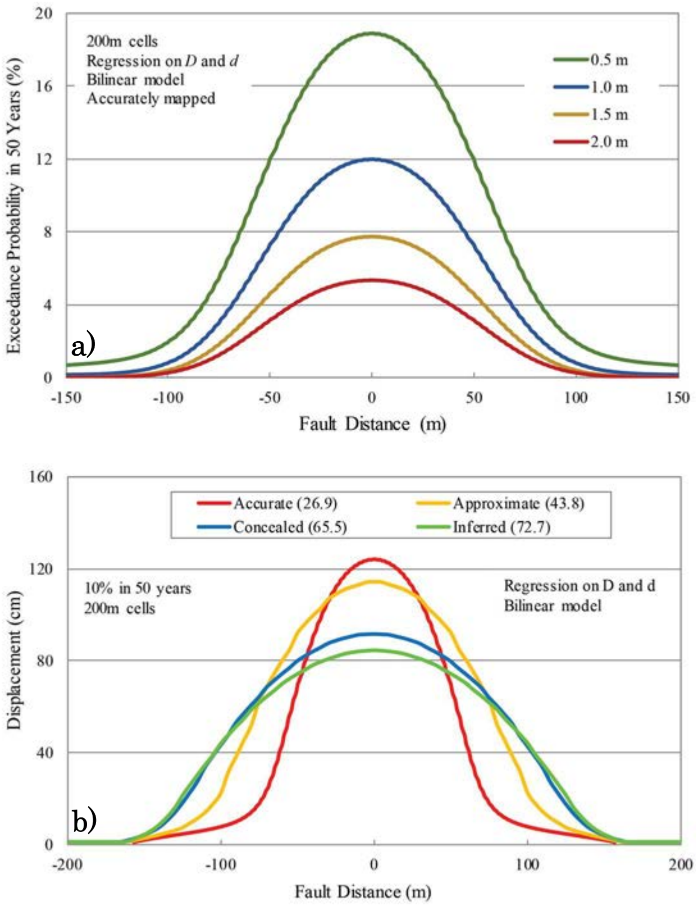

FIG 15. Examples of calculated exceedance probability and displacement profiles across mapped fault: a) exceedance probability in 50 years for different displacement levels; b) displacement across a mapped fault showing effects of mapping quality (standard deviations in meters are presented in parentheses). Without location uncertainty, one would expect principal displacement only on the mapped fault trace (with permission from [27]).

Like many other types of uncertainties, location uncertainty has aleatory and epistemic components. The summary statistics from [27] in Tables 1 and 2 includes both components. Epistemic uncertainty is associated with mapping and other inaccuracy, whereas aleatory variability reflects natural randomness in surface rupture location. With regard to epistemic uncertainty, it is stated in [102]:

> "Traditionally, active faults are mapped by geologists using field methods and aerial photographs or other remote sensing imagery. They record the locations and extents of fault-related geomorphic and stratigraphic features onto a base map. Thus, the accuracy of a mapped fault trace depends on quality of the base map, clarity of fault-related features, ability of the geologist to identify these features, availability of reference topography and landmarks, and ability of the geologist to accurately mark the recognized features on the base map.
>
> Maps produced according the National Map Accuracy Standards (https://egsc.usgs.gov/isb/pubs/factsheets/fs/17199) often include feature location uncertainty specified by the map maker. For example, the USGS 7.5-minute quadrangle topographic maps (standard mapping scale of 1:24,000 or 1 cm equals 240 meters) have an inherent feature

location uncertainty of about 15 m. Feature location uncertainty may be larger in certain terrains and for maps produced before modern positioning techniques, such as Global Positioning System (GPS), became available. In addition, features drawn on the base map have uncertainty that is often unknow.” [102]

An example of epistemic location uncertainty is shown in Figure 16 at a location on the Superstition Hills fault in California. There is a 25 m to 30 m location discrepancy (*r*) between the mapped trace of the A-P earthquake fault zone map compared to a fault scarp shown in the LiDAR-derived hill shade relief image. As stated in [102], the fault mapping used traditional methods such as photogrammetry, without the benefit of LiDAR. The fault scarp shown in this example experienced trigger or surface ruptures from three historical events: the 1968 M_W 6.5 Borrego Mountain earthquake, the 1979 M_W 6.5 El Centro earthquake, and the 1987 M_W 6.6 Superstition Hills earthquake. Moreover, due to difficulties in transferring a well-recognized feature from the field to a base map with limited resolution, the inaccuracy of the mapped trace is epistemic. Obviously, with surface rupture from past earthquakes and high-resolution images, fault map can be improved to reduce location uncertainty.

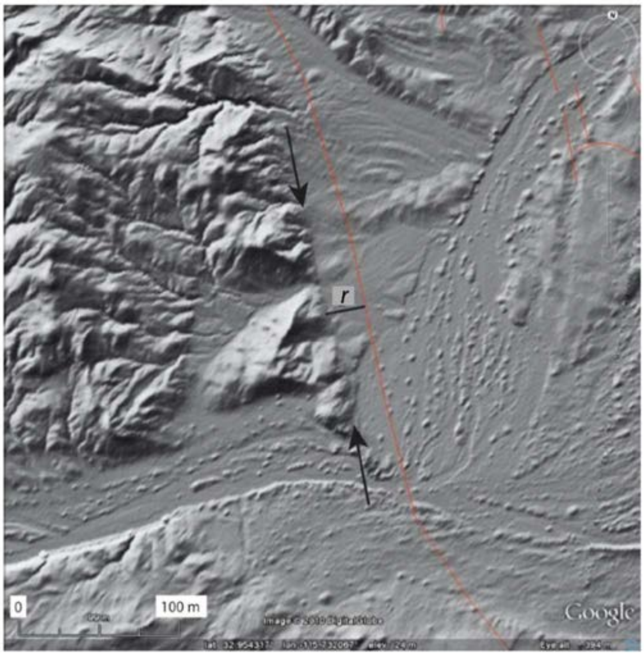

FIG 16. Relation between the location of fault scarp (shown by black arrows) and mapped fault trace locations (in red). The fault trace is taken from a 1:24 000-scale Alquist-Priolo Earthquake Fault Zone map. In this case, the discrepancy r between the mapped fault trace and the geomorphic fault feature is about 30 m and it is associated with epistemic uncertainty in the 1:24 000 scale mapping. (with permission from [102]).

A quantitative estimate of the remaining epistemic location uncertainty can be factored into PFDHA analyses. Chen et al. in 2013 [102] demonstrated a GIS-based approach to develop data necessary to quantify location uncertainty associated with existing A-P fault maps. They obtained improved surface fault map traces by carefully interpreting fault features on high-resolution (sub-metre) LiDAR digital elevation models and other imagery specially processed to make fault features more easily recognizable. The epistemic uncertainty in the A-P maps was quantified by systematically measuring distances between improved fault traces and mapped A-P fault traces. Summary statistics of that dataset yielded epistemic location uncertainties of 23 m, 36 m, 44 m, and 45 m, respectively, for accurately located, approximately located, concealed, and inferred A-P fault traces. These numbers are 15% to 38% smaller than those obtained in [27].

The trench log shown in Figure 17 illustrates inherent (aleatory) variability in rupture location from earthquake to earthquake. The trench is situated within a small releasing stepover on the Garlock fault in California. At least four paleoseismic events are identified [103], showing the variability of faulting both in relative time and space. The event-to-event location variability can be quantified using paleoseismic trench logs by systematically measuring distances from the most recent to all previous events. Simpler, straight fault traces are less variable in location compared to faults in more structurally complex areas [103, 104]. Fault geometric complexity need to be addressed when interpreting trench observations and quantifying location variability.

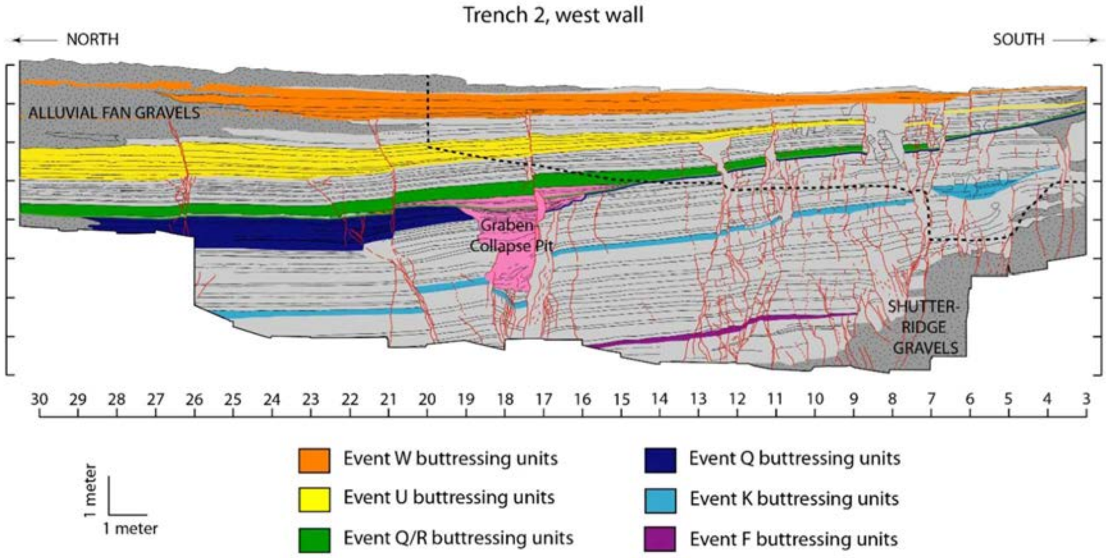

FIG 17. Trench log from the El Paso Peaks paleoseismic site on the Garlock fault showing the variability of rupture locations through time and space ([103], with permission). Faults at meters 12 and 22 ruptured during event U, and not the later event W, while the fault at meter 26 only ruptured during event W. The fault at meter 17-18 ruptured in multiple events, including Q, R, U, and W.

3.3.2.2. Implementation of rupture location uncertainty

Hazard analyses commonly treat epistemic uncertainty and aleatory variability separately. A logic tree approach is usually used to treat epistemic uncertainty and it consists of a given number of branches, where each branch represents and describes alternative models or parameter values. The judgment about the likelihood of the alternative models is represented by the weights on the branches. The branch weights sum to unity. Mathematically, weights are probabilities. Aleatory variability, on the other hand, is convoluted with hazard integration. These two kinds of uncertainties have different effects on calculated hazard. Epistemic uncertainty affects the spread of percentile hazard curves, whereas aleatory variability determines the intrinsic nature of each hazard curve, including its slope.

Similarly, epistemic uncertainty and aleatory variability in rupture location can be accounted for separately in PFDHA methodology. However, currently there is insufficient data to establish regression relations and essential statistics separately for each type of uncertainty. Mapping uncertainty can be treated using a logic tree approach, resulting in alternative displacement profiles across mapped faults and percentile hazard curves at given locations. Location variability affects the shape of the hazard curves and displacement profiles. It can be accounted for by integrating a probability density function similar to the approach used in [27].

3.3.2.3. Fault spatial complexity

The seismogenic structures often consist of multiple parallel or sub-parallel branches or splay faults that experience simultaneous principal rupture displacement in an earthquake. In such cases, principal displacement calculated from PFDHA can be partitioned among multiple branches and splays.

Chen and Petersen in 2011 [100] developed an approach to a partition fault displacement profile using the total displacement profile (e.g., that shown in Figure 15(b)) calculated from PFDHA. The partitioning of the displacement is based on the best-estimate displacement fraction (F_i) of each branch relative to the total displacement, where F_i is determined based on site- and fault-specific geological investigations, available data and professional judgement of the geologists, subject to epistemic uncertainty. Displacements from multiple branch profiles are added if the branch fractional profiles overlap in space to obtain a final profile across the entire fault zone. For the *i*th branch, the displacement fraction (F_i) is defined as:

$$F_i = \frac{D_i}{D} \tag{11}$$

where D_i is the fault displacement on the *i*th branch and D is the total fault displacement. The procedure involves the following steps: (1) calculate the total displacement profile using PFDHA assuming the fault has only one branch (the mapped main trace), which yields a single bell-shaped profile, $f(s)$, centred at the main fault trace; (2) scale the total displacement profile by displacement fraction (F_i) for the *i*th branch and centre the scaled profile at mapped trace of the *i*th branch; and (3) combine individual profiles for all branches, including the main branch, by adding displacement values at common locations to obtained the final, partitioned profile, $f_P(s)$, as:

$$f_P(s) = \sum_i F_i \times f(s + s_i) \tag{12}$$

where s_i is distance from branch i to the main trace. Adding s_i shifts the fractional profile to centre at the *i*th branch. The distance is positive on one side of the main trace, and negative on the opposite site. Figure 18 illustrates two cases of displacement partitioning assuming three mapped fault traces for a conceptual total profile shown in Figure 18(a). The fractional factor was chosen to be 20% for the branch to the left of the main trace, and 10% for the branch on the right, for illustration. Branch faults are assumed to be 100 m and 64 m on opposite sides of the main trace, respectively, in Figure 18(b), resulting in overlapping fractional profiles and an asymmetrical partitioned profile. In Figure 18(c), branch faults are assumed to be 900 m and 700 m on opposite sides of the main trace, respectively, which produced three fractional profiles that do not overlap in space and a partitioned profile with three distinct peaks.

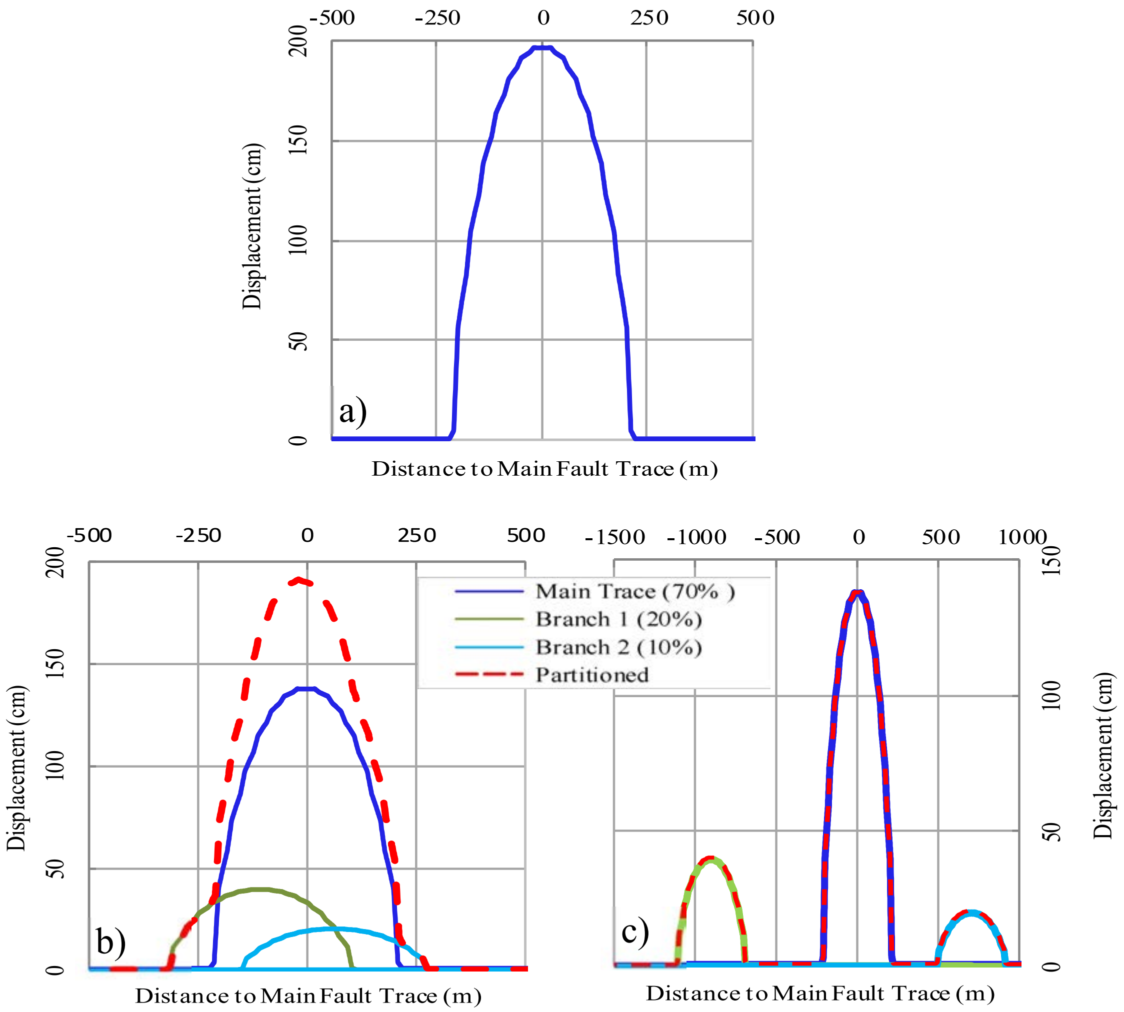

FIG 18. Illustration of displacement partitioning among the main trace and two branch traces: a) total profile without partition; b) partition with branch traces 100 m and 64 m on opposite sides of the main trace, respectively; c) partition with branch traces 900 m and 700 m on opposite sides of the main trace, respectively. ([100], with permission).

The displacement fraction in Eqs (11) and (12) needs to be based on professional judgement and available site data, subject to epistemic uncertainty. Displacement partitioning is one solution, other solutions might also be appropriate. For example, one could assign the probability of a rupture to each fault branch instead.

Slip partitioning and complex surface ruptures are observed in many recent and historical earthquakes, for example, the 2016 M_W 7.8 Kaikoura earthquake in New Zealand [105], the 2016 M_W 7.0 Kumamoto in Japan earthquake [106], and the 1999 M_W 7.1 Hector Mine earthquake in California [107]. There are also examples of relatively simple surface ruptures with nearly all co-seismic slip concentrated on a single mapped fault trace along at least some sections of faults, for example, the 2002 M_W 7.9 Denali earthquake in Alaska [108]. Apparently, it is difficult to know if a slip in future earthquakes will be partitioned or will occur mainly on a particular mapped trace. Nevertheless, one has to decide where to locate the expected displacement calculated from PFDHA. Such decisions significantly alter the outcome of the hazard analysis and need to reflect the results of thorough fault- and site-specific geological studies and professional judgment of the geologists.

Physics-based rupture models could provide insights on the likelihood of branching and degree of displacement partitioning (see Section 3.3.4). For instance, several theoretical studies showed that, for a fault system with multiple faults or fault branches, the path taken by rupture during an earthquake is a dynamic process that depends on fault geometry, stress field and friction mechanics [109–113]. Dynamic rupture propagation models representing existing, geometrically complex fault systems showed that the rupture of some combinations of faults and fault branches are more likely than others (e.g., for the Durance Fault in south-eastern France [114] and for the 2014 Northern Nagano earthquake [115]).

Chen and Petersen in 2011 [100] applied PFDHA approach in [27] to evaluate the fault displacement hazard along the southern San Andreas fault. Their analyses incorporated rupture location uncertainty and partitioning of calculated probabilistic displacement. Displacement hazard maps were produced in addition to probability and displacement profiles across the fault and displacement hazard curves at selected locations. Moreover, Chen and Petersen in 2011 [100] show examples of displacement hazard maps for a case assuming a rupture displacement occurring only along the mapped main fault trace and a case with displacement partitioned among multiple fault branches using slip fractions assigned in [116] for the ShakeOut scenario earthquake based on geological data and professional judgement. Those displacement hazard maps are very different, indicating displacement partitioning among branches is important in assessing fault displacement hazard.

Those displacement hazard maps also show that the lateral extent of the zone with potential surface fault displacement largely depends on location uncertainty and fault complexity. Narrower displacement zones are expected where fault traces are simpler (a single or few mapped traces) and faults are more accurately located (smaller location uncertainty). Wider displacement zones correspond to greater fault trace complexity and poorer mapping accuracy. It would be important in PFDHA to reduce epistemic location uncertainty by improving the accuracy of mapped fault traces and to better quantify aleatory variability in rupture location.

3.3.3. Shallow subsurface properties

The current empirical-based PFDHA models do not consider shallow material conditions as predictor variables for displacement, despite observations that suggest the effect of subsurface materials can be significant, as described in Section 2.3.4. Surface rupture from earthquakes extends further from the principal rupture to cover a wider zone on soft soil deposits compared to stiffer soils. This can be seen in several analogue experiments on sand. Loukidis and Salgado in 2009 [117] suggested that the band of strain in dense sand was narrower than in loose sand when subject to the same amount of base offset displacement.

Future empirical models are likely to incorporate the shallow material condition for displacement prediction. Moss et al. in 2013 [41] investigated the effect of $Vs30$ (time-averaged shear-wave velocity in the top 30 m) on the probability of surface rupture, in which $Vs30$ was derived from topographic slope [118]. The slope-derived $Vs30$ was classified into two groups to characterize soil stiffness: soft soil ($Vs30$ < 600 m/s) or stiff soil ($Vs30 \geq$ 600 m/s). A logistic regression was carried out on the data in reverse and strike-slip groups. The probability of surface rupture for reverse faults with low slope-derived *Vs*30 is lower than others. Subsequently, Moss et al. in 2018 [119] investigated the influence of soil shear stiffness by analogue experiments and numerical simulations. They found that shear stiffness controls the propagation of rupture and rupture zone width.

Thio and Oettle in 2018 [120] studied the effect of a soft overburden (sandy soil) numerically using PLAXIS 2D and found a straightforward relationship between soil thickness and reduction of principal fault displacement (Figure 19). These results are validated with experimental results, and it might be possible to use this methodology to develop relations between soil properties and surface deformation, both in terms of principal fault displacement reduction and the width of the deformation zone.

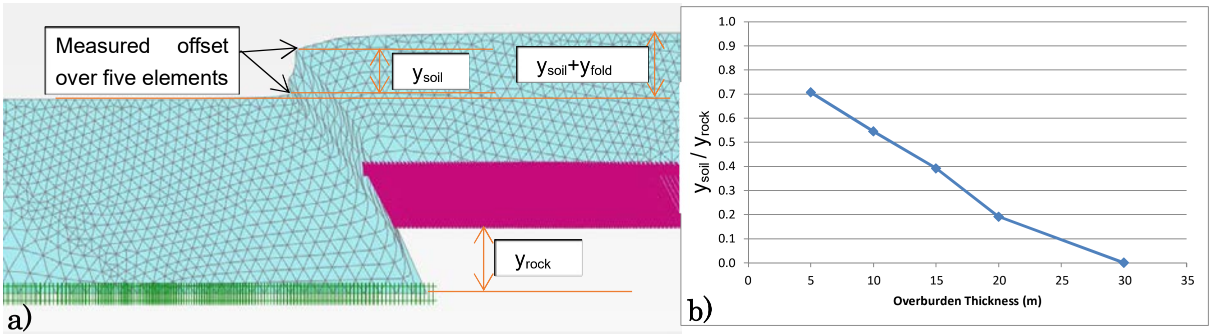

FIG 19. Numerical analysis of the effect of overburden thickness on surface displacement for a thrust fault. a) Model setup. b) Surface fault displacement as a function of overburden thickness. These results are for typical sandy soils ([120], whit permission).

In addition, there are some efforts to describe the surface rupture from earthquakes through physics-based models [121–124] that might be used for PFDHA, as described in Section 3.3.4. Therefore, a detailed description of the shallow subsurface properties of the site of interest would be essential.

3.3.4. Physics-based numerical simulation of fault rupture

Ideal models to fill the gaps due to the lack of data are physics-based models that take into account the following elements: (1) geometry of finite fault rupture; (2) physical rupture criteria to break the free-surface; (3) three-dimensional (3-D) stress field; and (4) geological and site conditions. These physics-based models can be constrained with available information of the area of interest; in particular, of primary importance, are the geometrical fault complexity [125–127] and the 3-D stress field. The level of detail of the fault geometry depends on the needs and sensitivity of the results [128]. The stress field is particularly essential when considering non-elastic off-fault deformation and fault networks with different fault orientations and depths [112, 129]. All these features are relevant for fault displacement prediction.

As described in Sections 3.1 and 3.3.1, due to data limitation the different components of PFDHA use empirical probability distribution models based in global data set (also limited) to estimate fault displacement. Nevertheless, earthquake processes are not consistent with such ergodic assumption, as demonstrated by some researchers using the largely increased ground motion database over the last decade [130–132]. The use of site-specific non-ergodic models can have a large effect on seismic hazard estimates [131]. Therefore, in the context of site-specific PFDHA, the physics-based numerical simulations, capturing details of the site of interest for fault displacement prediction, can complement the empirical models and available data to improve the representation of the site of study and to be consistent with the non-ergodic process of natural earthquakes.

3.3.4.1. Numerical models

3-D physics-based numerical simulation of fault displacement caused by principal faults can be done using the so-called dynamic rupture approach [133]. This method considers the physical processes involved in the fault rupture, incorporating conservation laws of continuum mechanics, friction, and stress state on the fault interface. The rupture is idealized as a dynamically running shear crack on a frictional interface embedded in a linearly elastic or nonlinear continuum. This idealization has proven to be a useful foundation for analysing natural earthquakes [134–137]. The fundamental concepts for the dynamic rupture approach such as friction law, stress drop, and fracture energy are explained in detail in Appendix III, as well as concepts of verification and validation that are needed for the application of such methods.

Incidentally, this approach can be applicable to model distributed faults which are generated by the rupture of the principal faults [121, 122, 127, 138–142]. These models allow the generation of off-fault plastic strain to relax the very high stress concentration in the dynamic rupture process around the rupture front. For example, Dalguer et al. use the discrete element method for the generation of localized off-fault cracks in a 3-D numerical simulation [121, 122] and found that the distribution of cracks is dominated along the extensional side on the main fault, and the length of the cracks increases with the rupture propagation distance of the principal fault. When the rupture of the principal fault approaches the free-surface, they also found that the off-faults cracks develop forming a flower-like structure surrounding the principal fault as a consequence of the fault rupture termination near the free-surface [121, 122]. Similar features have been modelled by other authors [140, 141]. Ma and Andrews in 2010 [140] attributed the formation of a flower-like structure as a consequence of the confining pressure that increases with depth, therefore, off-fault damage near the free-surface is easily created. The patterns of the associated off-fault cracks and plastic deformation simulated with 3-D numerical methods can provide useful insights on the extension of the distributed faults for the PFDHA.

The more explicit models to evaluate distributed-faulting probability and associated fault displacement is a priori incorporating the secondary or neighbouring faults in the dynamic rupture computation of the main fault. The location, geometry, and physical properties of the distributed faults (connected branches or not) can be obtained from field observations and geological studies. The distributed faults introduced in the model need to be the most relevant secondary faults with size compatible to the numerical discretization. Site specific evaluation of pre-existing faults is respected to provide accurate modelling.

3.3.4.2. Procedure for incorporating numerical models in PFDHA

The physics-based rupture models can contribute to the incorporation of numerical models in PFDHA in two ways: (1) to augment the limited empirical dataset with the generation of additional synthetic fault displacement data; and (2) to evaluate site-specific probabilities of a surface rupture for a fault with a given geometrical configuration, geological structure and a given magnitude.

The best information available from the area of interest, such as fault geometry, stress field, geological structure, geological slip rate, among others, would be necessary to better constrain the numerical model. A set of simulations needs to be composed of a sufficient number of realizations to capture reasonable statistical properties. The principal fault parameterization, characterized with stress drop and/or slip distribution models, can be generated stochastically with a series of random realizations or with asperity models, so that the statistical distributions are consistent with past earthquakes. The inclusion of physics-based simulation data in PFDHA would not only generate additional data but can also help to evaluate uncertainties.

3.3.4.3. Numerical example of fault displacement simulation

The distributed fault displacement decreases particularly when the distance from the principal fault is greater than 5 km based on observations. Accordingly, Takao et al. in 2014 [61] conducted model experiments and numerical calculations in order to complement the data. In this section, the key points of the numerical calculations are described.

For the numerical simulations, the discrete element method (DEM) was employed in order to collect the distributed fault displacement data. When performing the DEM, two sizes of the cell elements of the DEM (D = 1 mm and 2 mm), and two dip angles (45 and 60 degrees) for the reverse fault were taken into account. In order to confirm the reproducibility, Takao et al. in 2014 [61] validated the calculation results by comparing the experiment results performed in [143].

Examples of the DEM calculation results are indicated in Figure 20. The colouring of the figure is based on the square root of the second invariant of deviatoric strain ($\sqrt{J2}$). The ratio of the distributed fault displacement to the principal fault displacement (*d/AD*), in accordance with the distance from the principal fault, was plotted based on the results of the numerical simulations (Figure 21). In addition, since it is quite difficult to measure the maximum displacement in numerical calculations because of the narrow model (in the perpendicular direction to this figure), the results were assumed to be an average displacement. A 90% non-exceedance level curve can be developed based on the experimental, numerical and field data:

$$d / AD = 1.6e^{-0.20r} \quad (13)$$

where r is the distance from principal fault in km. Since the validity of utilizing the results of the model experiments and numerical calculations in the same way as the field data is controversial, Takao et al. in 2014 [61] described that this approach is a trial application and that further study and examination are necessary.

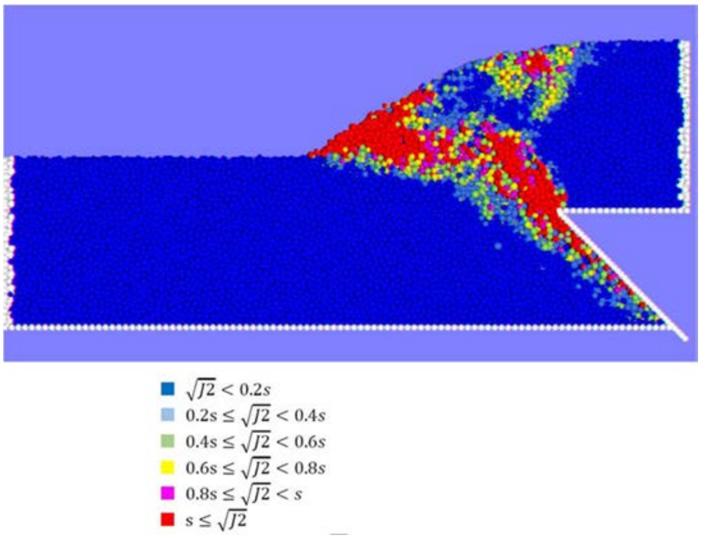

FIG 20. Amplitude of the square root of the second invariant of deviatoric strain $\sqrt{J2}$ from a Discrete Element Method fault rupture computation (dip angle = 45°) showing development of surface ruptures. S = 3.0 and $\sqrt{J2}$ was re-determined as an incremental from the state when a vertical displacement of the base was 2.4 cm in order to emphasize $\sqrt{J2}$. White elements have imposed boundary conditions following a lab experiment ([61], reproduced with permission).

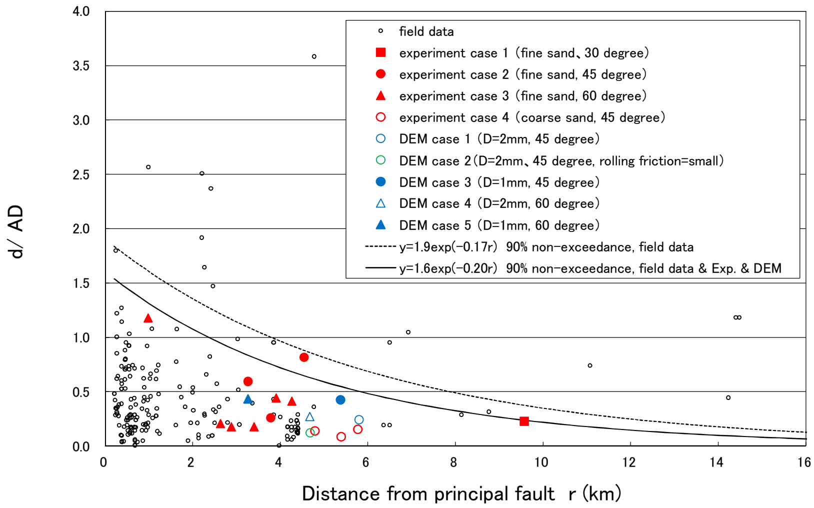

FIG 21. Revised d/AD attenuation curve based on experiment and Discrete Element Method ([61], reproduced with permission).

3.4. HAZARD RESULTS AND UNCERTAINTIES

The final stage of a PFDHA is the hazard computation using a hazard software and the inputs of seismic source characterization and fault displacement prediction models. This process requires the preparation of well-defined hazard inputs that incorporate aleatory and epistemic uncertainties. In order to capture epistemic uncertainties, logic tree branches and corresponding weights need to be objectively defined for each analysis. A general recommendation to capture epistemic uncertainty is described in Section 3.4.1 below.

The results of a PFDHA are most commonly represented by hazard curves that plot annual exceedance frequency versus fault-displacement amplitude. The total (or weighted mean) hazard curve is commonly presented along with hazard fractiles and various sensitivity plots. Examples of hazard curves from the Yucca Mountain nuclear waste repository site in Nevada, USA, and from the Krško

Nuclear Power Plant in Slovenia are provided in Sections 4.1 and 4.3, respectively. In addition to hazard curves, it might be desirable for some projects to present disaggregation results to determine the controlling earthquakes in terms of magnitude, distance, and standard deviation. Beside the computation of the hazard, a key element of the whole procedure is that the hazard results be reproducible at any time for evaluation of the results such as in sensitivity analyses as a result from new data, models and methods that become available after the completion of PFDHA. An example of the reproducibility of calculations and testing of results against new models is presented in the example from the Diablo Canyon Power Plant case study in Section 4.2.

3.4.1. Epistemic uncertainty assessment

The incorporation of epistemic uncertainty in a PFDHA might include logic trees that consider multiple assumptions, hypotheses, models, and model parameterizations. All paths through a logic tree are considered to result in a valid calculation of the hazard, with the combined weight through each path, reflecting the relative likelihood that a given path results in the correct result. The various paths through a logic tree might be represented by a suite of hazard curves associated with corresponding weights. A goal of the logic tree approach is to develop a model with alternative branches that are (at least approximately) mutually exclusive and collectively exhaustive, and assign weights for each branch that reflect the centre, body, and range of technically defensible interpretations as determined from an objective assessment of available data, models, and methods [144, 145]. This assessment needs to be performed for each part of the PFDHA.

Table 3 shows an example of epistemic uncertainties to be considered in PFDHA. It is essential to consider all the potential alternatives in terms of the items having epistemic uncertainties.

TABLE 3. EXAMPLE OF EPISTEMIC UNCERTAINTIES TO BE CONSIDERED IN PFDHA.

Fault type	**Examples of items having possibilities to be treated as epistemic uncertainties**	
	Displacement approach (direct approach)	**Earthquake approach**
Principal fault	· Seismogenic or not · recurrence interval · slip rate · average slip amount per event · variability degree of a probability density function such as standard deviation, shape factor, scale factor · adoption / non-adoption of ergodic hypothesis	(in addition to the items listed at left) · fault length · fault width · dip angle of fault plane · fault mechanism (normal/ reverse/ strike-slip) · earthquake magnitude · uniformity of displacement distribution (uniform/ non-uniform) · discrepancies in equations to evaluate items necessary for PFDHA such as scaling rule, occurrence probability
Distributed fault	· capability (capable/ incapable) · recurrence interval · slip rate · average slip amount per event · variability degree of a probability density function such as standard deviation, shape factor, scale factor · adoption / non-adoption of ergodic hypothesis	· distance from the principal fault · discrepancies in equations to evaluate items necessary for PFDHA such as occurrence probability, distance attenuation etc. · variability degree of a probability density function such as standard deviation, shape factor, scale factor

For an example as for mapping accuracy, Petersen et al. in 2011 [27] described as follows:

> "This mapping accuracy is an epistemic uncertainty and can be reduced with additional information. Normally this epistemic uncertainty should be considered as alternative branches in a logic tree. However, we do not have geologic data to separate the aleatory variability from the epistemic uncertainty." [27].

Therefore, Petersen et al. in 2011 [27] considered mapping accuracy as an aleatory variability using a normal distribution, which was derived from an analysis comparing the mapped fault with the rupture trace.

A way to display the impact of epistemic uncertainties on the total hazard in PFDHA is through a tornado plot. Figure 22 presents the results from a recent study in [120], which stems from a PFDHA on the Santa Susana fault in southern California. The model used is an updated version of UCERF3, and thus includes all the logic tree branches of that particular source characterization, as well as additional branches for the displacement prediction equations and source-specific modifications.

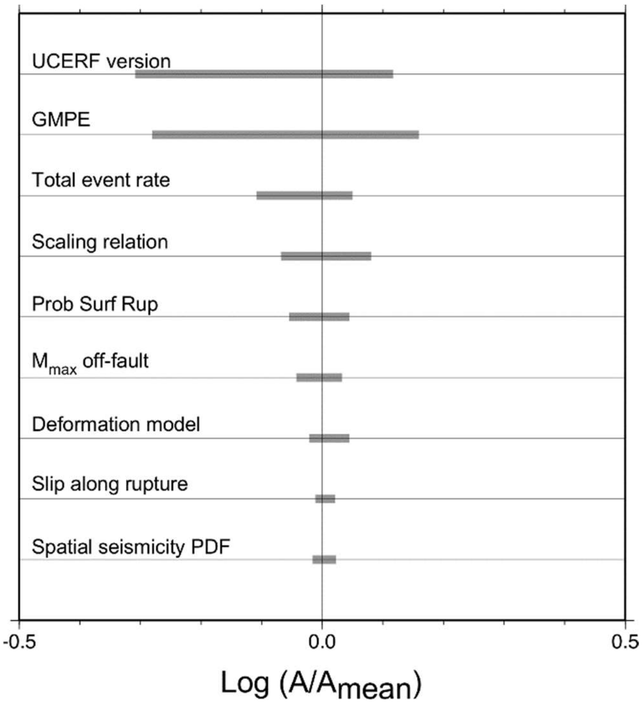

FIG 22. Tornado plot for a PFDHA in southern California ([146], with permission).

Currently, there is no specific guideline related to how to treat and consider epistemic uncertainties in PFDHA. However, the U.S. Nuclear Regulatory Commission (NRC) NUREG-2213 [145] and ANSI/ANS-2.30 [94], which provide methodology and procedure to address uncertainties in PSHA, are useful references when considering uncertainties in PFDHA.

3.4.2. Quality assurance and peer review

Adhering to a programme of quality assurance (QA) and peer review are required steps in PFDHA to ensure that an appropriate process in the hazard computation and epistemic uncertainty assessment has been conducted during the PFDHA, as well as to ensure that the final documentation is complete and traceable. Herein, these steps provided in the document ANSI/ANS-2.30 [94] are followed as described below: "Requirement for implementing a formal QA program may be established by the project sponsor. The sponsor shall identify the QA standards that must be met."

ANSI/ANS-2.30 recommends some applicable standards:

> "Quality assurance provisions may be specified to address document control, analysis control, software, validation and verification, procurement and audits, and nonconformance and corrective actions. PFDHA peer review requirements may be a subset of the QA provisions. Computer codes shall have a demonstrated and documented record of validity and accuracy but do not necessarily have to be formally licensed. Specific requirements on the computer code may be formulated by the sponsor on a case-by-case basis." [94].

The IAEA provides international peer review services for the safety of nuclear installations against seismic hazards [147] although a PFDHA peer review has not yet been requested by Member States. If it will be conducted in the future, PFDHA needs to be reviewed on the basis of SSG-9 [2], and QA needs to follow the recommendations for the management system in the IAEA peer review services.

3.4.3. Application of results for sites of interest

In most current applications, the PFDHA provides an understanding of the relationship between annual exceedance frequency and displacement amplitude for a site of interest. The results typically do not contain specific information about the exact location, width, localization, displacement direction, or earth forces exerted from the calculated displacement amount. For example, Eq. (7) estimates the conditional probability of a displacement at a site of dimension z a distance r from the principal rupture. This conditional probability, however, has no information on where within a site of dimension z the displacement might occur, or what the orientation of the displacement will be. Likewise, Eqs (8) and (9) make no prediction of the relative amounts of strike-slip versus dip-slip displacement other than the fact that the displacement prediction equations are typically selected according to the general style of faulting.

Accordingly, assessments of the performance of engineered structures to the displacement hazard commonly require additional site-specific geological and geotechnical input to provide details of the expected fault displacement. Examples of this additional input include: (1) the uncertainty zone, or zones across the site where the faulting might occur; (2) the extent to which the displacement might be localized or distributed within the uncertainty zone; (3) the near-surface strike, dip, and rake of displacement, so that horizontal and vertical components of displacement might be estimated; and (4) the geotechnical properties of the near-surface soils expected to exert forces on the engineered structure. Depending on the engineering application, one or more of the above items might be important to evaluate the impact of the hazard. In some instances, such as described in the case history for the Diablo Canyon Power Plant (Section 4.2), simple, highly conservative assumptions about the fault displacement are made in order to demonstrate the maximum impact the displacement might have on the safety of the installation. In other cases, a PFDHA might be conducted in order to understand the general shape and position of the hazard curves in order to evaluate whether fault displacement hazard might be screened out entirely.

For situations where a project desires an evaluation of the performance of engineered structures to fault displacement, site-specific geological and geotechnical studies might assist in providing this additional detail. Fault trenching near the site of interest, even if unable to provide information about the timing and amount of past displacements (i.e., to use the displacement approach), might be extremely useful to a project if it can document the location of faulting and the characteristics of the fault zone (including the fault zone width, the strike and dip of major fault planes, and kinematic information such as the fault rake). Fault trenching might be conducted in combination with other field methods such as geological and geomorphic mapping, image interpretation (from LiDAR or other topographic survey data and aerial photography), and other exploration methods such as inclined or vertical borings, cone penetrometers, or geophysical methods.

Even with the collection of site-specific information, there are often remaining uncertainties about future locations, widths, and directions of fault displacement. In these cases, it is common practice to estimate the uncertainties in these parameters and convey these uncertainties to engineers evaluating the performance of the engineered structures. Commonly, uncertainties in faulting parameters are inferred by observations of historical earthquakes that occurred elsewhere but arguably in similar tectonic and geological environments.

4. CASE STUDIES

In this Section, three case studies are introduced in where PFDHA has been performed to support the evaluation of nuclear installations. These case studies provide examples of conducting PFDHA with different project objectives and in different tectonic settings. In all situations, the PFDHAs were implemented with the empirical approaches described in Section 3, but different data needs and data inputs were required. The examples also highlight ways of capturing uncertainty in hazard and performing sensitivity analyses to document what displacement hazard parameters have the greatest impact on hazard uncertainty. The case studies provide readers with useful information for conducting site-specific PFDHA for existing nuclear installations or other critical facilities, even if each individual case is unique due to its peculiar characteristics.

The Yucca Mountain case study reports the pioneering PFDHA analyses performed in the mid-1990s for the proposed Yucca Mountain underground geological repository (Basin and Range Province, USA), that led to the development of a methodological approach in extensional tectonic domains [58, 148]. The study introduced the classification of a fault displacement hazard as either from principal or distributed faulting. The study implemented an approach whereby multiple expert teams investigated and calculated the hazard in parallel as a means of capturing epistemic uncertainty. The relatively large team-to-team differences in calculated the hazard was mainly due to the lack of an established methodology and to the limited data to constrain fault parameters.

The Diablo Canyon case study provides an application of the PFDHA methodology for distributed fault displacement hazard to a specific, safety-related engineered structure at an existing nuclear installation located away from the principal fault trace. The Diablo Canyon Power Plant (Central California, USA) is located in a transpressional tectonic setting, dominated at the regional scale by the San Andreas strike-slip fault. The applied methodology follows the general formulation in [27]. In this study, epistemic uncertainty in model parameterization was explored as separate iterations of the PFDHA, rather than as alternative logic-tree branch values and weights. The potential impact of a distributed fault displacement hazard to the nuclear installation is explored by examining annual exceedance frequencies corresponding to specific test displacement amplitudes, rather than by focusing on displacements that correspond to specified hazard levels.

The Krško (Slovenia) case study provides a probabilistic perspective on an assessment of fault capability for two sites being considered for a future nuclear power plant. This case study is out of scope because the scope of this publication is to provide PFDHA methodologies and case studies for existing nuclear installation sites. However, since examples applied to proposed nuclear facilities will help to evaluate and improve the present PFDHA methodologies in the future, the Krško (Slovenia) case study was presented here as one example for the future. The site vicinity is characterized by transpressional tectonics related to complex interactions among microplates and tectonic domains in the convergence zone between the African and European plates. A PFDHA was performed to provide additional information and context for regulatory decision-making with respect to possible fault capability.

4.1. CASE STUDY: YUCCA MOUNTAIN, NEVADA (USA)

In search of a long-term solution for the disposal of spent nuclear fuel and high-level radioactive waste, the U.S. beginning in the 1970s evaluated a potential underground geological repository near Yucca Mountain about 160 km northwest of Las Vegas, Nevada (Figure 23). From 1994 to 1998, probabilistic seismic hazard analyses were performed for both strong ground shaking and fault displacement [148]. The analyses were carried out by six teams of three experts each for seismic source and fault displacement (SSFD) characterization, and seven individual experts for ground motion characterization. The Yucca Mountain seismic hazard investigations represented the first Senior Seismic Hazard Advisory Committee [149] Level 4 study ever performed. The following, which is wholly extracted in [148], describes and summarizes the pioneering analyses performed for Yucca Mountain that led to modern PFDHA [58].

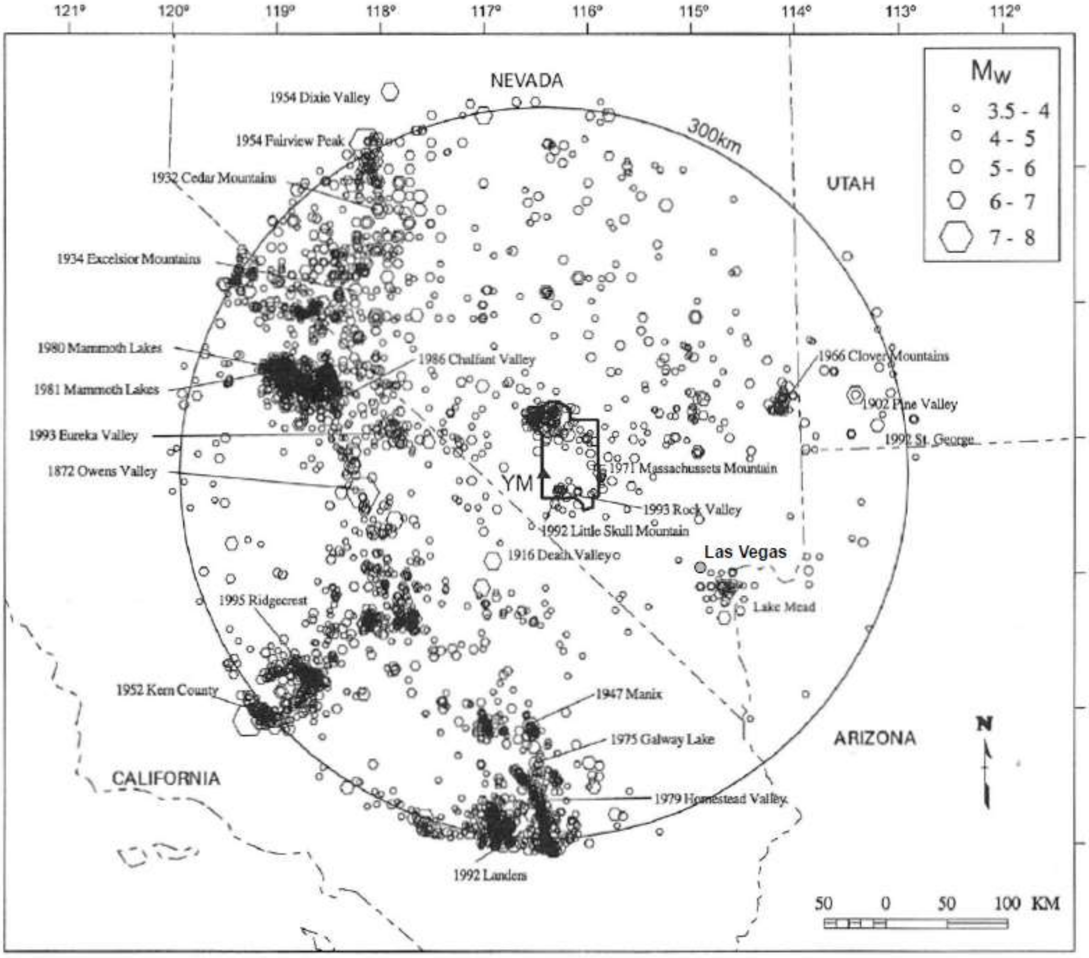

FIG 23. Historical seismicity (1868 to 1996) M_W 3.5 or Modified Mercalli Intensity III or greater within 300 km of Yucca Mountain. Significant earthquakes are noted ([148], with permission).

4.1.1. Seismotectonic setting and local faults

Yucca Mountain is located in the southern Basin and Range Province of the western U.S. The province is tectonically active in extension at a low strain rate and is characterized by late-Quaternary normal faulting and a moderate level of historical seismicity (Figure 23). Paleoseismic investigations indicate that earthquakes up to M_W 7 and larger have occurred in the past along numerous Quaternary faults within 100 km of the site (Figure 24). Yucca Mountain is a north-striking and east-dipping fault block and is one of several sub-parallel blocks bounded by typical Basin-and-Range high-angle normal faults caused by extension. The proposed repository site (indicated by the dotted line and 'Emplacement Area' label in Figures 24 and 25) is bounded on the west by the Solitario Canyon fault and on the east by the Bow Ridge fault. Intrablock faults close to the site include the Ghost Dance, Sundance, and Drill Hole Wash faults.

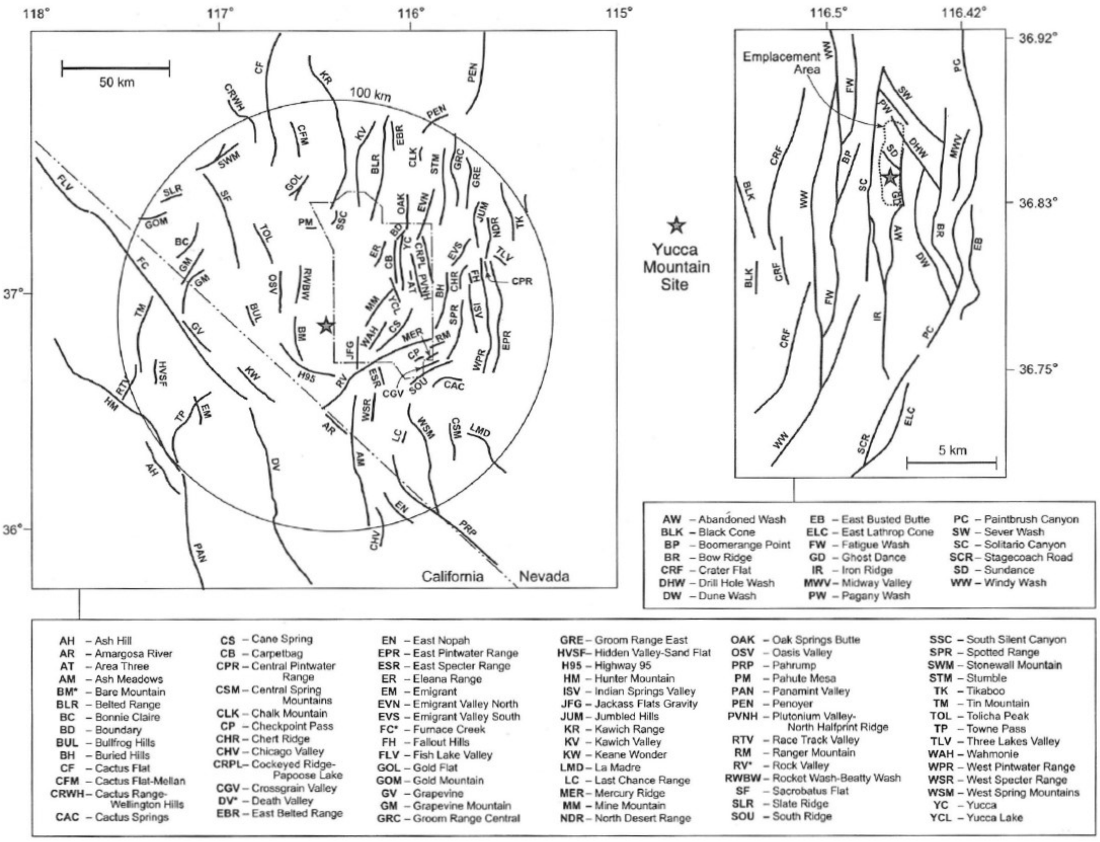

FIG 24. Known or suspected Quaternary faults within 100 km of Yucca Mountain. Local faults are shown on the right. Boundary of the Nevada Test Site is also shown ([148], with permission).

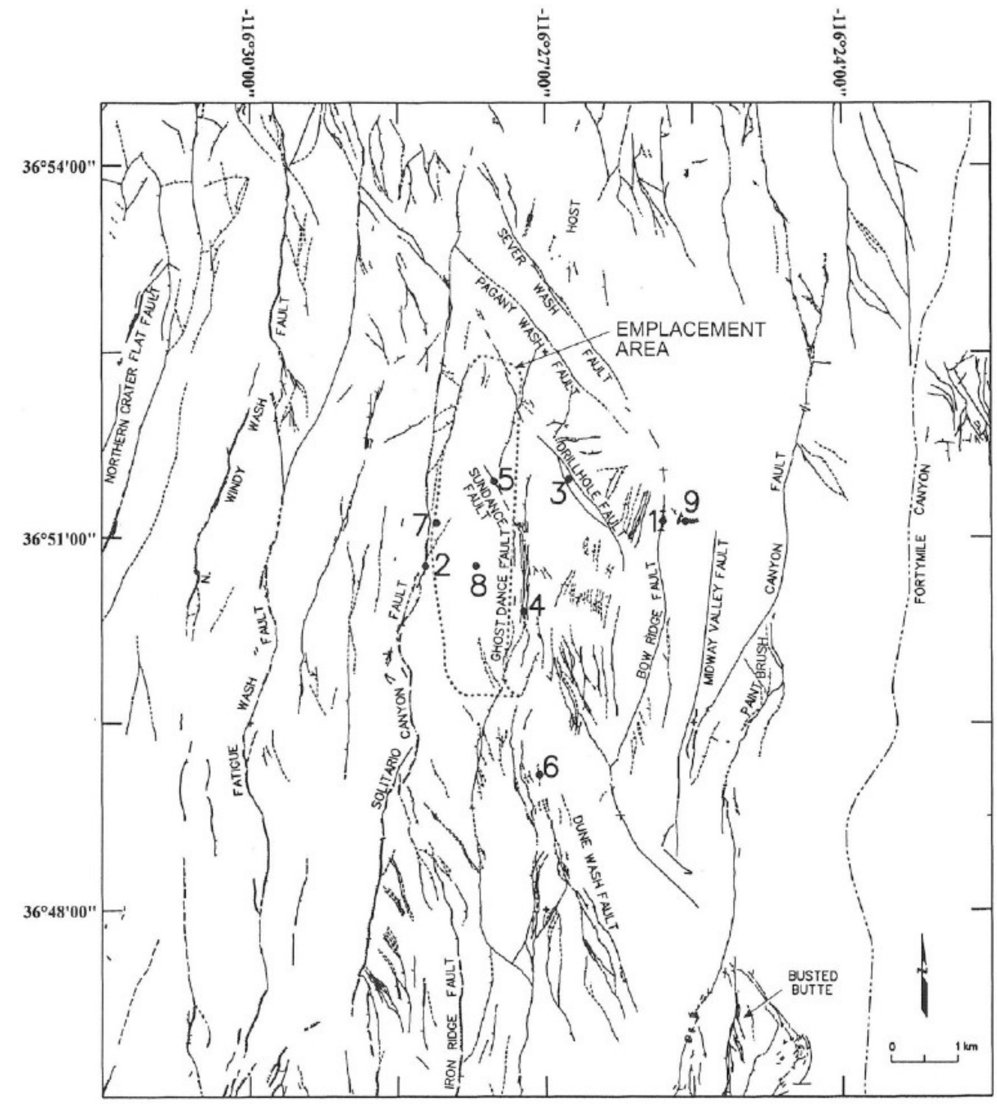

FIG 25. Nine locations for demonstration of fault displacement hazard assessment. Yucca Mountain is bounded on the west by the Solitario Canyon fault and on the east by the Bow Ridge fault. Potential waste emplacement area is also shown ([148], with permission).

Extensive geologic, geophysical, and paleoseismic analyses were performed to investigate the local faults within approximately 10 to 20 km of the site. These analyses included detailed geological and structural mapping and paleoseismic fault trenching, logging, and age-dating of deposits. The faults fall into one of three categories (Figure 25): (1) north-striking, block-bounding faults which show evidence for multiple displacements during the Quaternary; (2) northwest-striking faults that show no evidence for Quaternary movement; and (3) north-to northeast-striking intrablock faults that also do not appear to have moved during the Quaternary. The close spacing between faults, their anastomosing pattern, and their relatively short lengths indicate that the local faults might be structurally interconnected along the strike, or at depth, and thus might rupture either partially or fully together.

The most significant local faults with respect to seismic hazard are listed in Table 4 along with the general range of fault source parameters interpreted by the six SSFD expert teams. All these faults show evidence of multiple surface-rupturing earthquakes during the Quaternary. The mapped fault lengths are 27 km or shorter. The preferred slip rates are 0.001 to 0.05 mm/a (Table 4). Paleoseismic trenching indicates that simultaneous ruptures on some of the subparallel faults might have occurred several times during the Quaternary within the resolution of the dating. In addition to fault length and slip rate, the SSFD expert teams also assigned fault source parameters such as fault dip, sense of slip, maximum magnitude, and rupture behaviour. With regards to the latter, the expert teams decided whether the local faults acted as independent seismic sources (ruptured separately) or ruptured simultaneously with adjacent faults.

TABLE 4. FAULT PARAMETERS OF SIGNIFICANT LOCAL FAULTS AS CHARACTERIZED BY SSFD EXPERT TEAMS ([148], REPRODUCED WITH PERMISSION).

Fault Name	Rupture Length (km)	Distance† (km)	Sense of Slip‡	Fault Dip	Slip Rate§ (mm/a)	Probability of Activity
Solitario Canyon	16-19	1	LL-N	60º	0.01-0.03	1.0
Iron Ridge	6-9	2.5	LL-N	60º	0.002-0.004	0.1-1.0
Bow Ridge	6-8	2.5	LL-N	60º	0.002-0.003	0.4-1.0
Fatigue Wash	9-17	3.5	LL-N	60º	0.002-0.009	0.9-1.0
Paintbrush Canyon	12-19	4	LL-N	60º	0.002-0.017	1.0
Windy Wash	5-27	4.5	LL-N	60º	0.003-0.03	0.6-1.0
North Crater Flat	6-13	6	LL-N	60º	0.001-0.003	0.5-1.0
South Crater Flat	6-8	8	LL-N	60º	0.001-0.008	0.5-1.0
Stagecoach Road	4-10	10	LL-N	60º	0.016-0.05	1.0

† Approximate shortest distance to repository.

‡ LL=left-lateral strike-slip; N=normal.

§ Average or range of best estimate values interpreted by the expert teams.

4.1.2. PFDHA methodology

The SSFD expert teams developed original approaches to model and characterize the fault displacement potential for input to the PFDHA. Those approaches are described in [58], and in Section 3.1 of this publication. Important concepts introduced from the Yucca Mountain study include the classification of fault displacement hazard as either from principal or distributed faulting (Section 2.3), and the alternative methods to model hazard consisting of the displacement approach (Section 3.1) and the earthquake approach (Section 3.1). The earthquake approach to PFDHA developed at Yucca Mountain includes the definition of the conditional probability of the slip at the site of interest (represented in this publication by the two terms $P[sr \neq 0|m]$ and either $P[D \neq 0|z, sr \neq 0]$ or $P[d \neq 0|sr \neq 0]$ in Section 3.1), and the conditional probability of exceedance, (represented in this publication by $P[D \geq D_0 \mid l/L, m, D \neq 0]$ for principal faulting or $P[d > d_0 \mid r, m, d \neq 0]$ for distributed faulting in Section

3.1). The displacement approach is slightly different, as the direct observation of the paleoseismic surface-fault ruptures at (or near) the site of interest is used to develop a mean rate of surface-rupturing displacement events, λ_{DE}, and the conditional probability of exceedance simplifies to $P(D > d \mid Slip)$.

Under the earthquake approach, the SSFD expert teams defined the rate of surface-fault ruptures on principal faults at a site based on the frequency of the earthquake they had evaluated for the ground motion analysis and the conditional probability of the slip. As stated above, the conditional probability of a slip at the site of interest included both, the probability that the event beneath the site ruptured the ground surface and the probability of rupture at the site, which they described as the along-strike intersection probability. Most of the expert teams used an empirical model based on historical ruptures to compute the probability of a surface rupture as a function of magnitude (Section 3.3.1). The along-strike intersection probability was computed numerically (rather than empirically) using the rupture length estimated from the event magnitude randomly located along the length of the fault. For distributed faulting, the SSFD expert teams relied on empirical relations based on observations of historical ruptures from the Basin and Range. The conditional probability of a distributed slip was found to correlate with both earthquake magnitude and distance from the principal rupture (Section 3.3.2.2 and Appendix I). Logistic regressions for the probability of a distributed slip within a site of square dimensions 0.5 km × 0.5 km were developed for hanging wall and footwall settings. The SSFD teams also explored the effect of the angular difference between a principal and secondary fault on the conditional probability of distributed slip.

The preferred method under the earthquake approach to estimate the conditional probability of displacement exceedance at a site on a principal fault was to define a distribution for the maximum surface-fault displacement based on either the magnitude or the rupture length (Section 3.3.2.3). This distribution was convolved with a distribution for the ratio of displacement at a site along a surface-fault rupture to the maximum displacement to compute estimates of the mean slip and aleatory variability. Similar relations were developed by some of the SSFD expert teams based on empirical relations between average displacement and rupture length or average displacement and magnitude. For distributed faulting, the expert teams found very few empirical observations of distributed displacement on which to base displacement exceedance functions. A variety of approaches were developed, including relations using the largest distributed displacement normalized to the maximum principal fault displacement. These normalized data appeared to show a decrease as a function of distance from the principal fault.

For the displacement approach, similar methods were used for calculating the hazard of both principal faulting and distributed faulting. The preferred method for estimating the rate of surface-rupturing events, λ_{DE}, used the fault slip rate divided by the average displacement per event. This approach was used commonly instead of direct paleo-earthquake age data from paleoseismology by necessity, as quantitative data on event timing was difficult to obtain. The average displacement per event was estimated based on direct paleoseismic observations or empirical relations between displacement and fault length and/or cumulative fault offset, with the scaling factors in the empirical relations specifically developed for the Yucca Mountain area using local or sub-regional data. The SSFD expert teams used a number of approaches to evaluate the conditional probability of displacement exceedance, which consists of defining an average and variability about the average. The approaches focused on normalizing individual paleo-earthquake displacement observations at the Yucca Mountain site to a variety of factors, including pooled Yucca Mountain paleoseismic data, empirical displacement-length relations and empirical displacement-cumulative fault offset relations.

In aggregate, the six SSFD expert teams slightly preferred (as reflected in the logic-tree branch weights) the displacement approach over the earthquake approach for purposes of characterizing the hazard at Yucca Mountain. The expert teams were most uncertain in their characterization of distributed faulting using the earthquake approach. The widest variation in approaches were those for assessing the distribution for displacement per event on the distributed ruptures.

4.1.3. PFDHA results

The PFDHA was calculated at nine demonstration sites on representative locations within the potential repository facility area, as shown in Figure 25 and listed in Table 5. Locations 1 and 2 are on the block-bounding Bow Ridge and Solitario Canyon faults, respectively, and are sites where the hazard derives from principal faulting. Locations 3 to 9 are sites where the hazard is from distributed faulting. Locations 7 and 8 have four alternative displacement histories specified to represent fault and fracture conditions that have been mapped at Yucca Mountain (2 m small fault, 10 cm-shear, fracture, and intact rock). The SSFD expert teams varied widely in their assessments of distributed faulting that could occur at Locations 3 to 9 which are away from the block-bounding faults.

TABLE 5. MEAN DISPLACEMENT HAZARD AT NINE DEMONSTRATION LOCATIONS (*[148]*, REPRODUCED WITH PERMISSION).

		Displacement (cm)	
Location	**Location Description**	**10^{-4} AEP†**	**10^{-5} AEP**
1	Bow Ridge fault	<0.1	7.8
2	Solitario Canyon fault	<0.1	32
3	Drill Hole Wash fault	<0.1	<0.1
4	Ghost Dance fault	<0.1	<0.1
5	Sundance fault	<0.1	<0.1
6	Unnamed fault west of Dune Wash	<0.1	<0.1
7	100 m east of Solitario Canyon fault		
7a	2-m small fault	<0.1	<0.1
7b	10-cm shear	<0.1	<0.1

Location	Location Description	Displacement (cm) 10^{-4} AEP†	10^{-5} AEP
7c	Fracture	<0.1	<0.1
7d	Intact rock	<0.1	<0.1
8	Between Solitario Canyon and Ghost Dance faults		
8a	2-m small fault	<0.1	<0.1
8b	10-cm shear	<0.1	<0.1
8c	Fracture	<0.1	<0.1
8d	Intact rock	<0.1	<0.1
9	Midway Valley	<0.1	0.1

† AEP = annual exceedance probability.

The integrated hazard curves derived from the SSFD expert team inputs and their uncertainties are shown in Figures 26 and 27 for three locations. Figure 26 shows the results for Location 1 on the Bow Ridge fault and Location 2 on the Solitario Canyon fault, both block-bounding faults (Figures 24 and 25). With the exception of these results, the fault displacements were all 0.1 cm or less for a return period of 100 000 years (10^{-5} a^{-1} annual exceedance frequency). The results for all nine locations are summarized in Table 5.

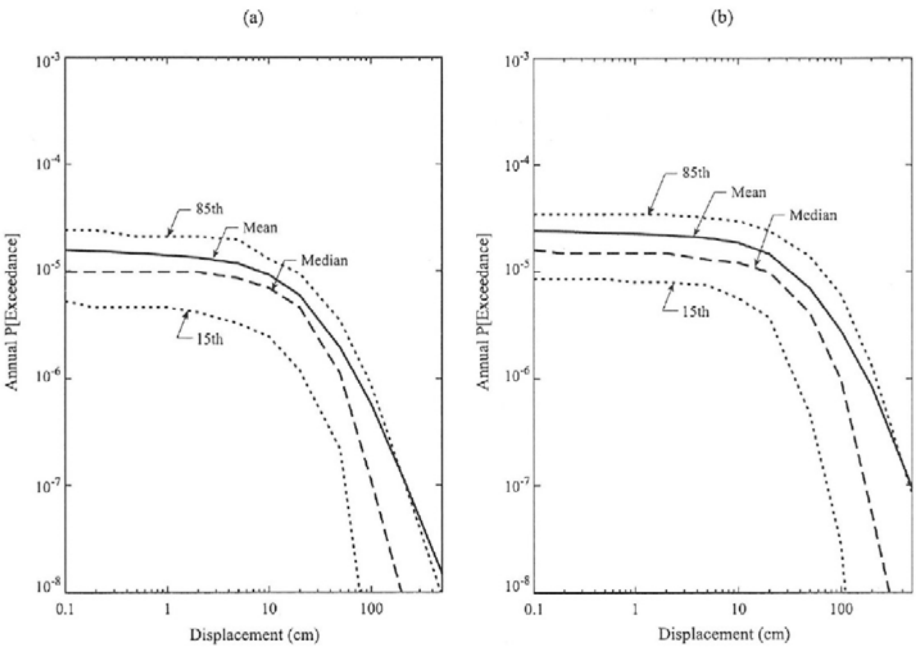

FIG 26. Summary hazard curves for (a) Location 1, Bow Ridge fault, and (b) Location 2, Solitario Canyon fault ([148], with permission).

The uncertainties in the fault displacement hazard (Figures 26 and 27) are quite large. Figure 28 shows the relatively large team-to-team epistemic uncertainty in the mean displacement hazard for Location 1. This could be attributed to the limited data to constrain the fault parameters, the difference in background and expertise of the teams, and the lack of a standard of practice for PFDHA. Following the completion of the study, the fault displacement hazard was taken into account in assessing the pre-closure and post-closure safety of the proposed repository.

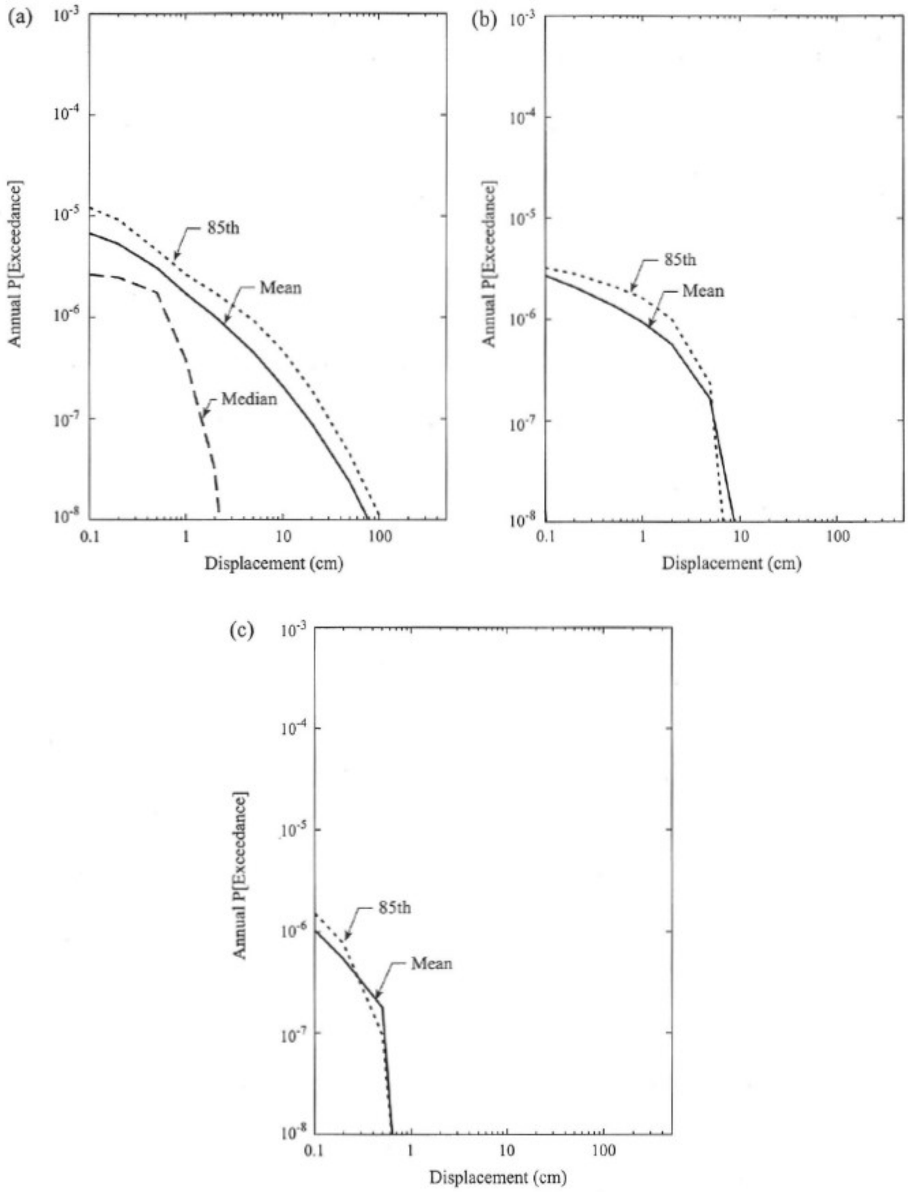

FIG 27. Summary hazard curves for Location 8, midway between Ghost Dance and Solitario Canyon faults: (a) 2 m cumulative displacement, (b) 10 cm cumulative displacement, and (c) no measurable cumulative displacement ([148], with permission).

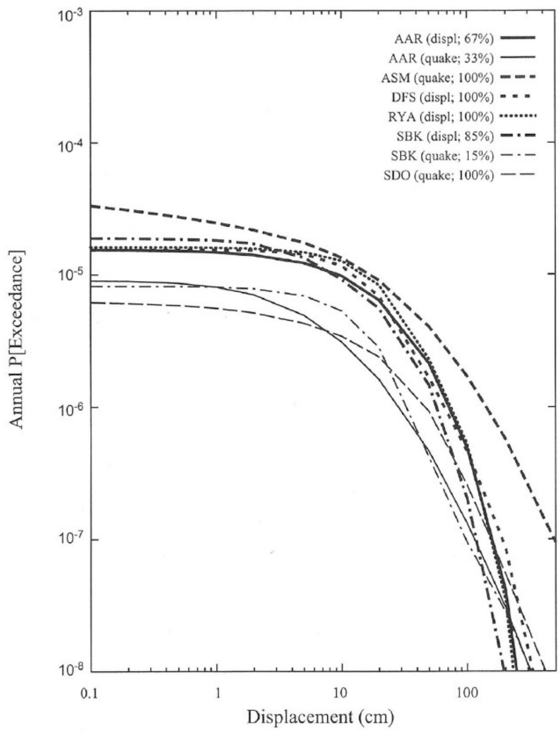

FIG 28. Mean hazard curves by team for Location 1, Bow Ridge fault ([148], with permission).

4.2. CASE STUDY: DIABLO CANYON POWER PLANT, CALIFORNIA (USA)

The Diablo Canyon Power Plant (DCPP), which generates electricity from two 1 100 MW pressurized-water reactors, is located on the central California coast, approximately half-way between the Los Angeles and San Francisco metropolitan areas (Figure 29). The recognition in 2008 of an alignment of small earthquakes led to the discovery of the Shoreline fault, a strike-slip fault that is located offshore less than one kilometre from DCPP [150, 151]. As part of the initial investigations to understand the seismic hazard and risk of the Shoreline fault to the DCPP, a PFDHA was conducted for the plant's auxiliary saltwater intake pipes, which are safety-related structures that were determined to be vulnerable to small permanent ground displacements [152, 153]. This case study summarizes the PFDHA conducted for DCPP, which implemented the hazard formulation for strike-slip faulting environments developed in [27]. The case study presents an example application of the PFDHA methodology for distributed fault displacement hazard to a specific, safety-related engineered structure at an existing nuclear installation located away from the principal fault trace.

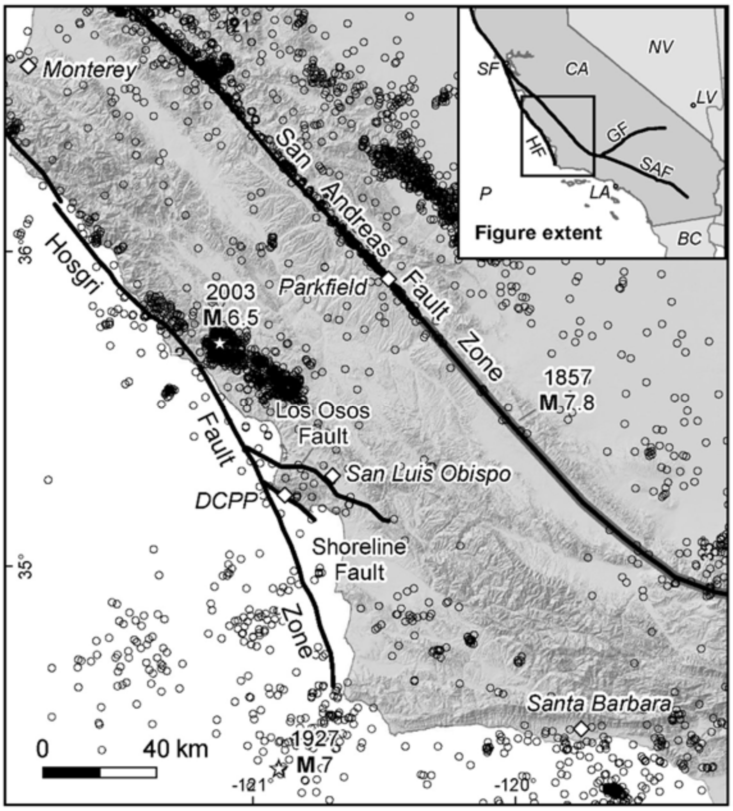

FIG 29. Shaded-relief digital topography of central coastal California showing the Diablo Canyon Power Plant (DCPP) in relation to selected faults and historical seismicity. Circles are earthquakes M≥2.5 from U.S. Geological Survey [154]. Stars mark epicenters of the 1927 M_S7.0 Lompoc earthquake and 2003 M_W6.5 San Simeon earthquake. Both earthquakes were near, but not on, the Hosgri fault zone. Extent of 1857 M_W7.8 Fort Tejon earthquake fault rupture on the southern San Andreas fault indicated by grey highlight. (Inset) BC, Baja California; CA, California; GF, Garlock Fault; HF, Hosgri fault, LA, Los Angeles; LV, Los Vegas; NV, Nevada; P, Pacific Ocean; SAF, San Andreas fault; SF, San Francisco.

4.2.1. Seismotectonic setting and discovery of the Shoreline fault

The DCPP is situated within central coastal California, a mountainous region of steep hillsides and rugged coastlines that extends approximately from the Monterey Peninsula in the north to Santa Barbara in the south (Figure 29). The region is situated primarily west of the strike-slip San Andreas Fault and is a seismically and tectonically active area of transpression (consisting of strike-slip, reverse-slip, and strike-slip-oblique faulting). The longest and most remarkable fault within the DCPP vicinity is the strike-slip Hosgri fault, which is located offshore and approximately 5 km from the plant at closest approach (Figures 29 and 30). In addition to the Hosgri fault, which has a slip rate of 1 to 5 mm/a [155, 156], DCPP is also located within the hanging wall of the southwest-dipping reverse- to oblique-slip Los Osos fault and the northeast-dipping reverse-slip San Luis Bay fault (Figure 29 and 30). The late quaternary slip rates of the Los Osos and San Luis Bay faults are approximately 0.1 to 0.3 mm/a [157], which are similar to the slip rates of other faults east of the Hosgri fault in the DCPP vicinity [158, 159]. Notable large, historic earthquakes in the DCPP region include the offshore 1927 shear-wave magnitude (MS) 7.0 Lompoc earthquake [160] and the onshore 2003 M_W 6.5 San Simeon earthquake [161] (Figure 29).

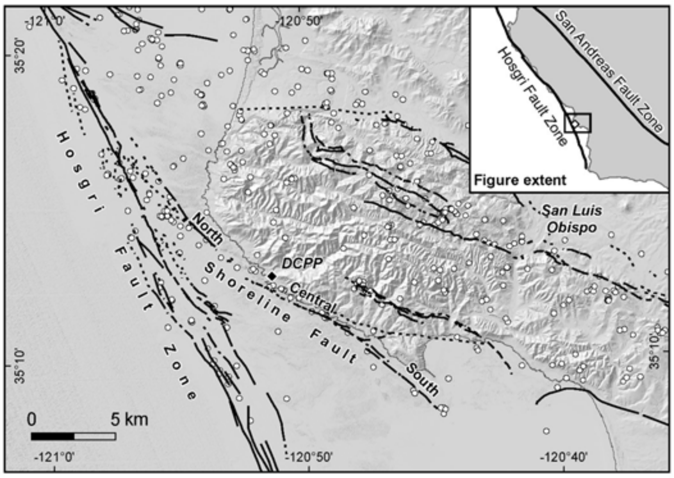

FIG 30. Shaded-relief digital topography and bathymetry of the DCPP area. Open circles are small (0 ≤ M ≤ 3.5) earthquake epicentres based on double-difference techniques from [150]. Traces of the Hosgri, Shoreline, and other faults from [159] as recognized in 2010, shortly after the discovery of the seismicity lineament. The North, Central, and South segments of the Shoreline fault are labelled.

As part of its ongoing licensing condition with the U.S. Nuclear Regulatory Commission (NRC), Pacific Gas and Electric Company (PG&E) has been proactively studying seismic hazards at DCPP since the plant began its operation in the mid-1980s [162]. In 2008, an alignment of small earthquakes (magnitudes <1 to 3.5; occurring between 1987 and 2007) was recognized offshore of DCPP between the coastline and the Hosgri fault [150]. The seismicity lineament was recognizable in large part due to the dense seismic network installed and maintained by PG&E along the California coast that produced an earthquake catalogue suitable for double-difference hypocentral re-location techniques. Subsequent investigations by PG&E, which included additional seismicity analyses, the collection and interpretation of high-resolution bathymetric data from a multibeam echo sounder (MBES) survey, gravity and magnetic geophysical data collection and interpretation, detailed geological mapping and the creation of an onshore-offshore geological map, confirmed the presence of a previously unrecognized, strike-slip Shoreline fault [151].

The preliminary assessment of the Shoreline fault recognized a total fault length of approximately 20 km that was divided into three geometric segments: the north (6-9 km long), central (8 km long), and southern (6 km long) (Figure 30). The segments were recognized based on distinct patterns of microseismicity, expression in MBES bathymetric data and geophysics, and a segmentation model was applied to the fault for the purpose of magnitude assessment. The most credible interpretations for purpose of deterministic seismic hazard assessment for DCPP were considered in [151] to be the rupture of the central segment only (M_W 6.0), and a combined central and southern segment rupture (M_W 6.25).

The location of the central segment of the Shoreline fault with respect to the DCPP was well constrained by the bathymetric data, which shows an abrupt, linear west-facing scarp in the bedrock offshore of the plant (Figure 31). The fault is located 600 m from the DCPP power block and 300 m from the cooling water intake. Initially – prior to completion of the geological and geophysical studies – there was concern that a zone of weaker rock (tertiary shale, claystone, and siltstone) that underlies the intake pipes might be susceptible to secondary fault displacement during earthquakes on the Shoreline fault. Specifically, it was recognized that dresser couplings along the auxiliary saltwater pipes that cross the zone of weaker rock were vulnerable to small displacements. As the pipes represent the only safety-related structures, systems, and components vulnerable to small displacements close to the Shoreline fault, PG&E conducted a PFDHA of the secondary fault deformation occurring at any of the dresser coupling sections [152]. The NRC reviewed PG&Es calculation and performed an independent confirmatory analysis to evaluate the displacement hazard and the resulting potential effect to the annual frequency of core damage at the DCPP [153]. After further geological mapping and analysis of available geological and geomorphological data, PG&E in 2011 [151] concluded that the weaker rock underlying the intake was not part of a through-going shear zone, and that the fault displacement hazard could be ruled out on a deterministic basis.

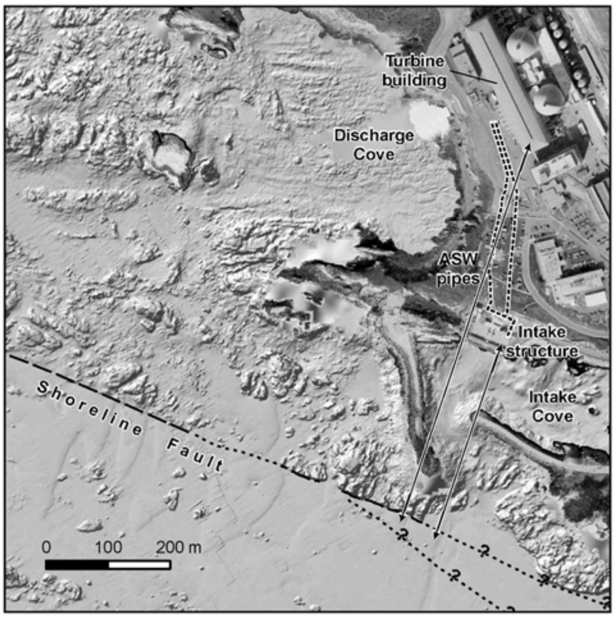

FIG 31. Map of the DCPP and offshore area showing relationship between the Shoreline fault and the plant. Offshore areas displayed using artificial shaded-relief bathymetric data from high-resolution MBES data [152]; onshore areas are displayed using a high-resolution aerial photograph. The central segment of the Shoreline fault is clearly expressed in the bathymetry as a linear southwest-facing scarp. Auxiliary saltwater pipes containing the fragile dresser couplings are indicated by dashed lines. Closest distances from the Shoreline fault to the intake structure and turbine building are 300 m and 600 m, respectively, as indicated by the arrows; these distances are used for the r values in the PFDHA.

4.2.2. PFDHA methodology

The approach used in [152] to perform the PFDHA calculation relied on an Association of the Society of Civil Engineers (ASCE) conference proceedings paper that reported findings of a study, funded through the Pacific Earthquake Engineering Research (PEER) Institute, in [163]. The final project results were later published in [27]. Between [163] and [27], some model parameters changed. The NRC, in their confirmatory analysis [153], considered both the information used in [152] and the subsequently published parameters in [27].

Petersen et al. [27] relies on the general form of the earthquake approach to PFDHA, as presented in Section 3.1.2 of this publication. In the formulation, the annual exceedance frequency for distributed fault displacement *d* resulting from an earthquake of magnitude *m* and occurring at a site with a footprint of dimension *z* at a distance *r* from the principal fault is (reproduced from Eq. (9)):

$$\lambda\left(d \geq d_0\right)_{xyz} = \alpha \int_{m,s} f_{M,S}\left(m,s\right) P\left[sr \neq 0 \middle| m\right] \times \int_{r} f_R\left(r\right) P\left[d \neq 0 \middle| r,z,sr \neq 0\right] \times P\left[d \geq d_0 \middle| r,m,d \neq 0\right] drdmds \tag{14}$$

For the DCPP study, PG&E assumed that the Shoreline fault rupture always passes through the portion of the fault plane nearest to the plant (i.e., $f_s(s)$ = 1), and fixed the distance between the fault trace and the site of interest to be a constant (i.e., the distance PDF $f_R(r)$ was modelled as a delta function). With these assumptions, Eq. (9) was simplified to:

$$\lambda\left(d \geq d_0\right)_{xyz} = \alpha \int_{m=M_{\min}}^{M_{\max}} f_M\left(m\right) P\left[sr \neq 0 \middle| m\right] P\left[d \neq 0 \middle| r,z,sr \neq 0\right] P\left[d \geq d_0 \middle| r,m,d \neq 0\right] dm \tag{15}$$

The term in Eq. (15) and notes on implementation as stated in [152] are provided in Table 6. The first three items in Table 6 constitute the characterization of the fault source by defining the location of the fault relative to the site and the magnitude-frequency distribution. The second two terms are conditional probabilities that define the probability of surface rupture for the Shoreline fault and for the site located away from the primary fault. The last term describes the probability of displacement exceedance given the occurrence of distributed fault displacement at the site.

TABLE 6. TERMS AND NOTES ON IMPLEMENTATION FOR THE DCPP CASE STUDY PFDHA.

Term	Explanation	Notes on Implementation
Fault Source Characterization		
r	Distance from the fault to the site of interest	PG&E in 2010 [152] assumed constant r = 600 m; NRC [153] considered alternative constants r = 600 m and r = 300 m in confirmatory calculation.
$f_M\left(m\right)$	Probability density function (pdf) for the magnitude-frequency distribution	Youngs and Coppersmith characteristic model used [164]. Characteristic magnitude (M_{char}) defined from fault dimensions; $M_{\max} = M_{\text{char}}$ + 0.25 magnitude units.
α	Earthquake activity rate, defined as the ratio of the rate of total accumulated moment on the fault to the average moment release per earthquake	Defined based on moment balancing between fault slip rate and fault area and the Youngs and Coppersmith magnitude PDF [164]. Bounding maximum and minimum slip rate estimates used in moment balancing to derive the activity rate parameter.
Conditional Probabilities of Surface Rupture		

Term	Explanation	Notes on Implementation
$P\left[sr \neq 0 \middle| m\right]$	Conditional probability of surface rupture given magnitude m, which recognizes that not all earthquakes produce surface-fault rupture	Used empirical magnitude-area scaling and fault dimensions to derive the probability of surface rupture based on magnitude. Did not use logistic regression from empirical data on magnitude and presence or absence of surface-fault rupture [58]. NRC in 2012 [153] noted magnitude-area scaling approach of PG&E is more conservative.
$P\left[d \neq 0 \middle| r, z, sr \neq 0\right]$	Conditional probability of non-zero displacement at a location of distance r with dimensions z and given an event with surface rupture ($sr \neq 0$)	PG&E in 2010 [152] developed probability by considering information in [163] for 50m × 50 m footprint, selected case to represent the Shoreline fault setting, and then adjusted the 50m × 50 m probability to account for the reduced probability of faults intersecting the dresser coupling intersections only. NRC in 2012 [153] adopted 50m × 50 m probability in [27] and also adjusted for smaller area of possible dresser coupling-fault intersection.
Probability of Displacement Exceedance		
$P\left[d \geq 0 \middle| r, m, d \neq 0\right]$	Conditional probability of secondary displacement d greater than or equal to a test amplitude d_0 given an earthquake of magnitude m that produces displacement at a location of distance r	PG&E in 2010 [152] developed equations based on secondary displacements normalized to maximum principal fault displacement presented in [163]. NRC in 2012 [153] implemented the equations in [27].

4.2.3. Model parameterization

The parameterization of Eq. (15) is described below as follows: the fault source characterization elements (Section 4.2.3.1), conditional probabilities of rupture (Section 4.2.3.2) and probability of displacement exceedance (Section 4.2.3.3).

4.2.3.1. Fault source characterization

Two alternative fixed distances between the Shoreline fault and the application site of the PFDHA were considered: a distance of 600 m, representing the closest distance from the Shoreline fault to the power block, and a distance of 300 m, representing the closest distance from the fault to the intake structure [153]. The weaker rock unit that underlies the dresser couplings of the auxiliary saltwater pipes is located between these two distances (Figure 31).

The PFDHA used a simplified fault source characterization to develop the magnitude-recurrence distribution based on a preliminary evaluation of the Shoreline fault [152]. Later seismic hazard studies for DCPP developed more sophisticated fault source characterizations of the Shoreline fault for input to

PSHA that emphasized epistemic uncertainty [152, 159]. Fault source parameters used for fault dimensions, estimates of characteristic earthquake magnitudes (M_{char}) for the Youngs and Coppersmith probability distribution [164], and moment balancing to calculate the activity rate and the magnitude-frequency distribution are provided in Table 7.

TABLE 7. FAULT SOURCE PARAMETERS USED FOR THE DCPP STUDY.

Parameter	Value	Justification
Style of faulting	Strike-slip	Based on focal mechanism and vertical alignment of microseismicity.
Length of characteristic fault rupture	8 km (central segment only) 14 km (central and southern segments) 20 km (entire Shoreline fault)	Alternative rupture lengths consider the segmentation defined for the Shoreline fault in [152]; the full fault length was only considered in [153] for their confirmatory analysis.
Fault dip and seismogenic thickness	Vertical 10 km (central segment only) 12 km (central and southern segments) 12 km (entire fault)	Microseismicity along the Shoreline fault suggests vertical fault plane; thicknesses based on depth of seismicity observed along the fault and in the region.
Functional form of the magnitude-frequency distribution	Youngs and Coppersmith (1985) characteristic earthquake model	Commonly used in practice to describe the magnitude-frequency distribution on faults.
Characteristic magnitude (M_{char})	M_W 6.0 (southern segment only) M_W 6.25 (central and southern segments) M_W 6.7 (entire Shoreline fault)	Based on empirical magnitude-area relations. M_W 6.7 case explored only in [153] for their confirmatory analysis
Magnitude range	$M_{min} = M_W$ 5.0 $M_{max} = M_{char} + 0.25$	Magnitudes below M_W 5.0 on the Shoreline fault not expected to produce surface-fault displacement. Upper limit is defined in [164].
Slip rate	0.01 to 0.3 mm/a	Preliminary judgment based on comparison to other faults and geomorphic expression in MBES bathymetric data.

Epistemic uncertainty in the magnitude-recurrence relationship is represented by the two cases of M_{char} (M_W 6.0 and M_W 6.25, representing the two alternative characteristic rupture scenarios) and by the bounding estimates of fault slip rate (0.01 and 0.3 mm/a). Rather than assign logic-tree branch weights to these alternative values capture epistemic uncertainty in a mean hazard calculation, PG&E in 2010 [152] adopted the approach of considering these four source characterization cases (two characteristic magnitudes times two slip rates) in separate implementations of the PFDHA. The approach is consistent with the objective of this preliminary PFDHA, which was to evaluate the potential impact of the fault displacement hazard to the overall safety of the plant.

In their confirmatory calculation, NRC in 2012 [153] considered the same seismic source characterization parameters as PG&E (the fixed r distance of 300 m, the Youngs and Coppersmith magnitude distribution functional form [164], the M_W 6.0 and M_W 6.25 M_{char} values, and the bounding 0.01 and 0.3 mm/a slip rates), but also evaluated the case of a larger, M_W 6.7 characteristic magnitude that would be consistent with a rupture along the entire 20 km fault (Figure 30). Differences between the PG&E calculation and the NRC confirmatory analysis in the fault displacement prediction equations are discussed in Section 4.2.3.2 below.

4.2.3.2. Conditional probabilities of rupture

The PFDHA of the Shoreline fault includes two conditional probabilities of surface rupture, the probability of surface rupture given earthquake magnitude, $P[sr \neq 0|m]$, and the probability of non-zero surface rupture within the site of interest, $P[d \neq 0|r, z, sr \neq 0]$ (Section 3.1). The conditional probability of surface rupture accounts for the fact that not all active faults rupture to the surface, and the probability of surface-fault rupture increases with earthquake size. The conditional probability of non-zero surface rupture within the site accounts for the fact that distributed fault displacement will not always occur within a size of dimension z occurring a distance $r > 0$ away from the primary rupture trace. Both conditional probabilities have the effect of scaling the annual rate of ruptures impacting the site.

Several papers discuss the use of logistic regressions of global empirical data to develop the probability that surface rupture will occur given an earthquake of magnitude m on the fault (Sections 3.3.1 and 3.3.2.2). PG&E in 2010 [152] adopted a different approach of considering the likelihood of a surface-fault rupture for the Shoreline fault based on the fault dimensions and well-established empirical scaling relations between the log of the rupture area and the magnitude [5]. The rationale for this alternative approach is that the Shoreline fault is vertical and has a well constrained maximum seismogenic thickness of 10-12 km, whereas much of the global data used to derive the logistic regressions include faults with much greater seismogenic widths. Therefore, these global relations have the potential to underestimate the probability of surface rupture for faults with narrower widths.

For the conditional probability of a non-zero distributed surface rupture at the site of interest, PG&E in 2010 [152] evaluated the available data in [163] on the likelihood of distributed displacement occurring within a square footprint of 50 m × 50 m, as a function of distance r from the principal rupture. The 50 m square footprint size was selected because that was the approximate length of the auxiliary saltwater intake pipes within the weaker geological unit. Several considerations were taken for the selection of the conditional probability. First, as mentioned in Section 3.3.2.1, Petersen et al.

probabilities in [163] are based on the evaluation of eight historical strike-slip earthquakes with mapped principal and distributed surface displacements. The data show a broad range of probabilities of non-zero distributed fault displacement from the different earthquakes. In reviewing this broad range, PG&E considered the epistemic uncertainty of how distributed fault displacement on the Shoreline fault behaves relative to the global observations. PG&E in 2010 [152] judged that distributed displacement on the Shoreline fault near the DCPP was less likely to occur than the average of the global data based on the straight and simple trace of the central segment of the Shoreline fault compared to locally significant fault trace complexity observed in the global data. Accordingly, PG&E adopted a 50 m × 50 m rupture probability that represented the lower range of the global data compiled in [163]. The NRC in 2012 [153] acknowledged this reasoning, but elected to use the updated regression analysis in [27] and performed their calculation using the median predicted rupture probability. This median resulted in a probability that was about a factor of two larger than the PG&E assumption for the 600 m distance, and about a factor of four larger for the 300 m distance.

Next, PG&E in 2010 [152] noted that within the 50 m × 50 m footprint size, the specific structural elements that were vulnerable to small displacements—the dresser couplings—made up only a small portion. Accordingly, [152] and [153] adjusted the probability based on the length of the dresser couplings relative to the 50 m pipeline length.

4.2.3.3. Displacement exceedance probability

The displacement exceedance probability $P[d \geq d_0 \mid r, m, d \neq 0]$ defines the average displacement and the natural variability about the average expected given an earthquake of magnitude m ruptures within the site. As [27, 163] define a lognormal distribution for displacement variability, the general form of the displacement exceedance equation can be written as:

$$P\left[d \geq d_0 \middle| r, m, d \neq 0\right] = 1 - \Phi\left[\frac{\log_{10}\left(d_0\right) - \log_{10}\left(d_{med}\right)}{\sigma_d}\right] \tag{16}$$

where Φ is the standard normal cumulative distribution, d_{med} represents the median predicted distributed displacement, and σ_d represents the aleatory variability in distributed displacement about the average, expressed as a standard deviation in $\log_{10}$ units.

Petersen et al. in 2011 [27] defined alternative approaches to estimate the average and standard deviation of distributed fault displacement, including both a direct prediction of d as a function of distance r and magnitude m, and a normalized displacement model whereby off-fault distributed fault displacement is normalized by the average displacement expected given the earthquake magnitude (i.e., d/AD), and the displacement ratio is a function of distance r. Petersen et al. in 2004 [163] provided observations of distributed fault displacement normalized by the maximum displacement D_{max} observed for each historical event studied. The 2004 plot did not indicate an r dependence from the primary fault on the normalized displacements d/D_{max}. Accordingly, PG&E in 2010 [152] adopted an approach that predicts $d(m)$ from $d/MD \times MD(m)$, where MD was estimated from the Wells and Coppersmith [5] global empirical $\log_{10}MD - M_W$ model for strike-slip faults. NRC in 2012 [153] compared PG&E's approach with the later Petersen et al. [27] regression results that showed a weak r dependence on d/AD, and predicted $d(m)$ from $d/AD \times AD(m)$, where AD was estimated from the Wells and Coppersmith global empirical $\log_{10}AD$ - M_W model for strike-slip fault ruptures [5].

Thus, for the median displacement and standard deviation, both studies solved for:

$$\log_{10} d_{med} = \log_{10} d / D^* + \log_{10} D^* \quad (17)$$

and

$$\sigma_{\log_{10} d} = \sqrt{\sigma^2_{\log_{10} d/D^*} + \sigma^2_{\log_{10} D^*}} \quad (18)$$

where D^* represents MD or AD, depending on the study, and the total standard deviation is the square root of the sine of the standard deviations for the normalized displacements and the average of maximum displacements as published in [5].

4.2.4. PFDHA results

The PFDHA was calculated at two test amplitudes d_0, 1 cm and 2 cm, to reflect the estimated displacement capacity of the dresser couplings along the auxiliary saltwater pipes. Annual exceedance frequencies were calculated for 28 implementations of the PFDHA (Table 8), including 8 implementations of the PFDHA in [152] representing the two test amplitudes, two estimates of M_{char} (M_W 6.0 and M_W 6.25) and the two end-member estimates of fault slip rate (0.01 and 0.3 mm/a). NRC in 2012 [153] provided 20 implementations representing the equivalent PG&E in [152] but with different selections of secondary displacement probabilities (Section 4.2.3.2) and displacement normalization schemes (Section 4.2.3.3), with the alternative r = 300 m distance, and the M_{char} of M_W 6.7 case. As stated in Section 4.2.3.1, epistemic uncertainty in the PFDHA in these studies was not captured in a logic tree (with alternative branch values and weights) but rather as separate implementations in order to more easily explore the range of possible hazard levels at the test amplitudes, and thereby estimate in general terms the potential change in core damage frequency from the risk of surface-fault rupture hazard.

The results of the analyses broadly show that the annual exceedance frequency of 1 cm displacement is approximately 2.0×10^{-7} to 2.6×10^{-10} a^{-1}, with the highest hazard resulting from the combination of highest slip rate, largest magnitude, and shortest distance (Table 8). The annual exceedance frequency decreased by a factor of less than two for the larger test amplitude of 2 cm. The NRC's calculated values are about a factor of 6 larger than those of PG&E for the M_W 6.0 case, and about a factor of 4 larger than those of PG&E for the M_W 6.25 case. For the NRC results, the M_W 6.7 cases resulted in a factor of less than 1.5 higher than the equivalent M_W 6.25 cases.

TABLE 8. ANNUAL EXCEEDANCE PROBABILITIES FOR TWO DISPLACEMENT AMPLITUDES AT THE DRESSER COUPLINGS.

Characteristic Magnitude	Slip Rate (mm/a)	Annual Probability of Exceedance					
		PG&E Distance = 600 m		NRC Distance = 600 m		NRC Distance = 300 m	
		$d \geq 1.0$ cm	$d \geq 2.0$ cm	$d \geq 1.0$ cm	$d \geq 2.0$ cm	$d \geq 1.0$ cm	$d \geq 2.0$ cm
M_W 6.0	0.01	2.6E-10	1.4E-10	1.5E-9	7.9E-10	3.2E-9	1.7E-9
	0.03	7.8E-9	4.1E-9	4.6E-08	2.4E-8	9.5E-8	5.1E-8
M_W 6.25	0.01	6.0E-10	3.5E-10	2.5E-9	1.6E-9	5.4E-9	3.3E-9
	0.03	1.8E-8	1.1E-8	7.9E-8	4.7E-8	1.6E-7	9.8E-8
M_W 6.7	0.03	--	--	9.9E-8	7.0E-8	2.0E-7	1.4E-7

The results in Table 8 can be used to generally look at what parameter uncertainties have the greatest effect on the hazard. As discussed, the differences in the probability of a non-zero distributed surface rupture and displacement exceedance probabilities selected between [152] and [153] implementations result in a difference in the hazard of a factor of four to six, which is greater than the differences between characteristic magnitude selections (typically have differences in hazard less than a factor of two). Uncertainty in slip rate, however, results in a factor of 30 difference, which is a direct result of the factor of 30 difference between the low (0.01 mm/a) and high (0.3 mm/a) slip rate ranges. These differences underscore the importance in probabilistic hazard studies of performing sensitivity analyses to understand what epistemic uncertainties contribute most to the total hazard uncertainty.

4.2.5. Discussion

The hazard results in the DCPP case study of the Shoreline fault PFDHA were presented as annual exceedance frequencies associated with specific displacement amplitudes (1 and 2 cm), given a range of epistemic assumptions about the magnitude-frequency distribution for the Shoreline fault, the probability of secondary displacement at the site, and the appropriate fault displacement prediction equations for distributed fault displacement away from a primary fault. As stated, the approach in [152] to explore the epistemic alternatives as separate iterations of the PFDHA, rather than as alternative logic tree branch values and weights, is appropriate for this application as it is exploring the potential impacts to the DCPP.

The approach to presenting hazard results as exceedance probabilities at test amplitudes differs from the more typical approach of reporting the hazard as an amplitude (e.g., ground motion acceleration or velocity for PSHA and displacement for PFDHA) at one or more specified annual exceedance probabilities. For example, the Yucca Mountain case study (Section 4.1) notes that the results were tabulated as displacements that correspond to the 10^{-4} or 10^{-5} annual exceedance probabilities. The motivation for reporting the results as annual probabilities corresponding to specific test amplitudes for the DCPP case study rather than visa-versa is a direct result of the objective of the PFDHA: to assess the potential impact of secondary fault displacements to the calculated annual frequency of core damage at the DCPP. In the DCPP case, a review of the safety-related structures, systems, and components located near the Shoreline fault conducted by PG&E determined that the dresser couplings on the auxiliary saltwater pipes were the only vulnerable structures to small amounts of fault displacement, and preliminary deformation analyses suggested that the couplings could tolerate only 1 or 2 cm of the abrupt displacement. This preliminary fragility assessment allowed the hazard assessment to focus on the hazard and risk implications of specific structures. In the case of DCPP, the annual exceedance probabilities at the two test amplitudes (1 and 2 cm) were compared to the annual core damage frequency of the plant as a way of understanding the maximum potential impacts to the risk accepted under the operating license. Both [152] and [153] concluded that the risk from a surface-fault rupture was approximately two orders of magnitude or more (i.e., < 1%) of the annual frequency of a core damage, and thus the fault displacement hazard is a negligible contribution to the overall risk of the DCPP. Both studies noted that the risk comparison also makes two highly conservative assumptions: first, that the displacement always results in the failure of the dresser coupling; second, that the compromised dresser coupling always leads to core damage.

Alternative objectives of a PFDHA can and need to result in alternative ways of reporting the hazard results. For example, the NRC allows for events with less than 10^{-8} annual exceedance frequency to be excluded from the risk assessment for Yucca Mountain; such screening criteria might be defined for a project that can be used as a basis for evaluating the surface-displacement hazard for site development. In other cases, different hazard levels might be considered for the guidance in the design of new structures or retrofit of existing structures to be safe from the hazard of fault displacement. These decisions can be made with consideration of overall performance and risk goals for the project.

4.3. CASE STUDY: KRŠKO 2 PROPOSED NUCLEAR POWER PLANT (SLOVENIA)

The Krško Nuclear Power Plant is located in south-eastern Slovenia, about 80 km east of Ljubljana, and about 12 km from the border with Croatia. It is composed of one pressurized water reactor, which has been under operation since 1982.

The PFDHA study performed between 2012 and 2014 by RIZZO for *GEN energija* was related to a proposed new power plant (Krško 2) on a site adjacent to the existing nuclear power plant. Two possible locations ('East' and 'West' sites), a few hundred metres apart, were considered for the new installation. As faults had been identified in the area surrounding the East and West sites, the PFDHA was undertaken in part to better assess the suitability of the alternative sites. This brief summary of the PFDHA is based mainly on two reports [165, 166] and a case study presented at a conference [167].

Site characterization investigations used to support the site suitability assessment were carried out from 2007 to 2010 by a consortium led by the Bureau de Recherches Géologiques et Minières (BRGM) [168]. In addition to BRGM, the consortium included Geološki zavod Slovenije (GeoZS), Institut de Radioprotection et de Sûreté Nucléaire (IRSN), and Zavod za gradbeništvo Slovenije (ZAG). The site characterization studies included tectonic geomorphic analyses, paleoseismic trenching, geochronology for constraints on faulting; high-resolution seismic (refraction and reflection) surveys to identify the extent of faulting in the site vicinity and geotechnical field investigations. One primary focus of the site characterization studies was the Libna fault, which is mapped near the proposed East site.

4.3.1. Seismotectonic setting and local faults

The Krško site vicinity is characterized by transpressional tectonics related to complex interactions among microplates and tectonic domains in the convergence zone between the African and European plates (Figure 32). In the Krško basin, Neogene and Quaternary sediments are known to be deformed, but evidence for surface and near-surface faulting is unclear. The compressive stress is oriented approximately north-south. At the time of the PFDHA, strike-slip faulting was interpreted to dominate with some reverse faulting. In the vicinity of the proposed sites for the Krško 2 Nuclear Power Plant, several faults were known from previous investigations, and some of them were specifically studied for the purpose of assessing fault rupture capability. As considerable uncertainty remained following the geological investigations regarding the locations and capabilities of nearby faults, a PFDHA was carried out to help place the uncertainties in a probabilistic framework.

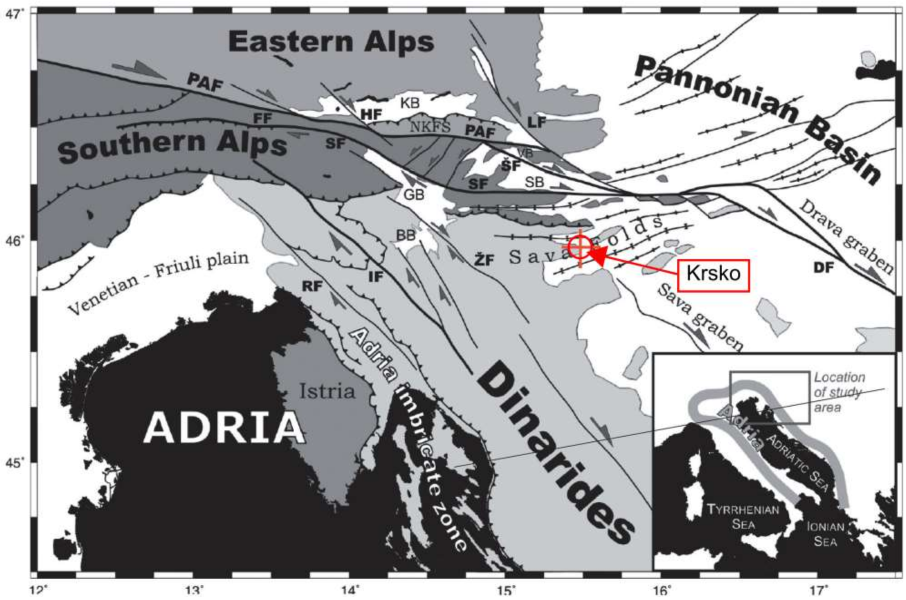

FIG 32. Simplified tectonic map of the Krško region. White: Neogene; IF: Idrija fault; PAF: Periadriatic fault; SF: Sava fault ([169], reproduced with permission).

4.3.2. PFDHA methodology

The PFDHA for the Krško 2 sites follows the earthquake approach proposed in [27] for strike-slip faulting environments (Section 3.1). The analysis considered the accuracy of fault mapping and fault complexity in the formulation of the PFDHA and included the hazards due to both principal-fault displacement and distributed-fault displacement. A logic-tree framework was used to represent epistemic uncertainties.

Fault characterization data were compiled from previous field studies. These data included: surface trace location, fault length, slip rate, seismogenic depth, and fault dip. From these data, 21 fault sources were included in the PFDHA representing different faults and fault extents within approximately 10 km of the Krško 2 sites (Figure 33). For each fault source, the input parameters such as probability of fault activity, fault geometry, slip rate, and maximum magnitude (M_{max}) were developed with alternative logic-tree values and weights to incorporate the parameter uncertainty. M_{max} was assessed for each fault source using the empirical relations in [5] between M_W and fault dimensions (length and area).

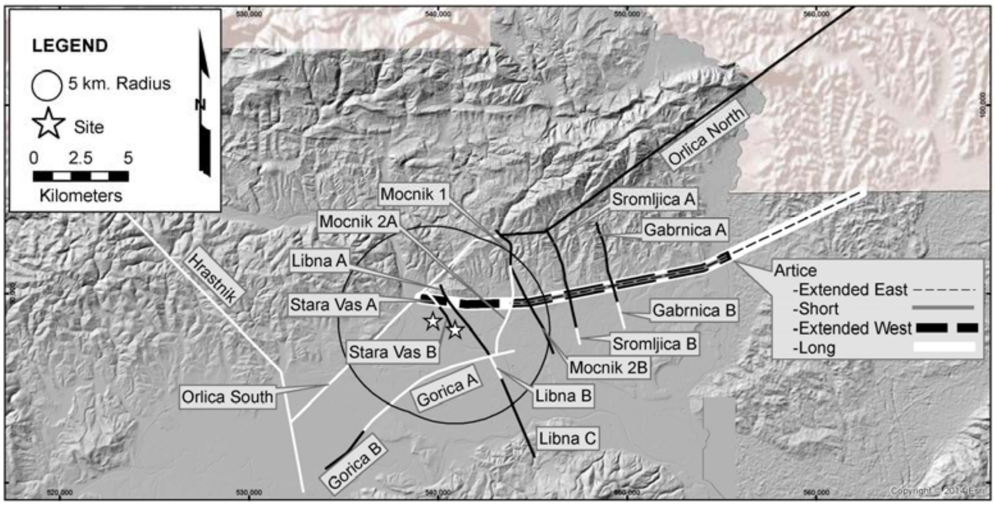

FIG 33. Fault model used in the Krško 2 PFDHA ([167], reproduced with permission).

The following assumptions were made regarding the fault displacement prediction equations:

(1) Displacement models in [27] were developed for strike-slip faulting, whereas the faults in the Krško 2 site vicinity were interpreted at the time of the PFDHA as possibly exhibiting an oblique component. Because the database used in [27] included measurements of oblique-slip surface displacement, the models were assumed to be reasonably adopted for the use for the Krško 2 PFDHA.

(2) The magnitude range for the database in [27] is M_W 6.4 to 7.9. The M_{max} values assessed for faults modelled in the PFDHA of Krško are generally lower than M_W 6.4. These models were deemed acceptable for lower magnitudes considering trends in their residuals.

(3) Considering that the faults in the vicinity of the Krško 2 sites have little or no surface expression, the category for uncertainty in distance from a future fault displacement to the sites was taken as 'inferred and complex'.

The input parameters and uncertainties were assessed by experts from RIZZO and GeoZS, taking into account concepts from the Senior Seismic Hazard Analysis Committee (SSHAC) guidance [149]. The PFDHA was reviewed by a peer review panel composed of three independent experts from outside the study. To address the peer review comments, a sensitivity study was performed to explore the influence on the fault displacement hazard of possible variations in the evaluation of each parameter. In general, the sensitivity cases examined the impact of conservative assumptions.

4.3.3. PFDHA results

The PFDHA was calculated for a 200 m × 200 m cell at each of the two proposed Krško 2 sites (Figure 34). The mean total hazard curves show that a surface-fault displacement of 0.001 m (1 mm) has a mean annual frequency of exceedance of approximately 10^{-6} a^{-1}. The hazard curve for the West site is lower than the curve for the East site at greater displacement values such that hazard at the East site is approximately a factor of 4 higher than hazard at the West site for a displacement amplitude of 0.1 m (Figure 34). At the West site, the total hazard is dominated by the distributed-fault displacement hazard, with contributions from several nearby fault sources [167]. At the East site, the total hazard is dominated by distributed-fault displacement from several fault sources at low displacements (≤ 0.02 m); at displacements greater than about 0.02 m, however, the contribution of principal-fault displacement hazard becomes more important. The source of the principal-fault displacement hazard for the East site is a postulated longer version of the Stara Vas fault, which comes close to the East site (Figure 33). This longer version of the Stara Vas fault is given a very low weight (0.1) in the logic tree.

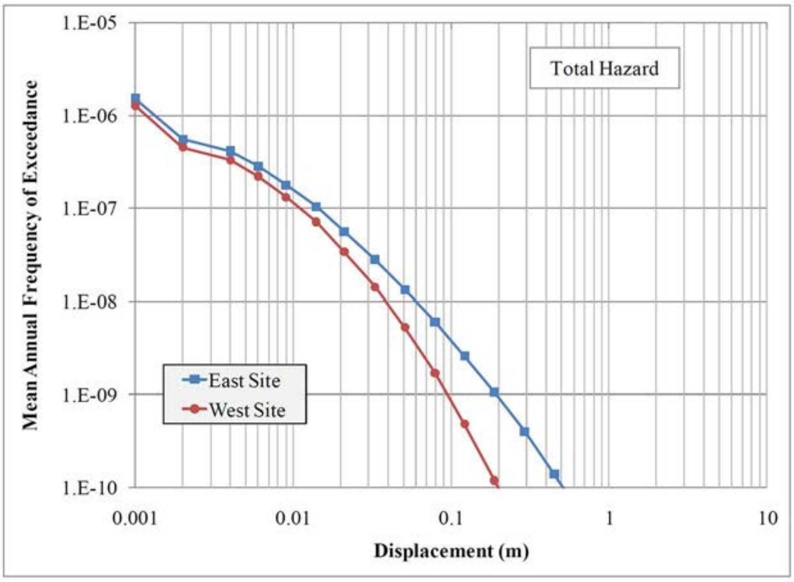

FIG 34. Results of the Krško 2 PFDHA for the base case ([166], reproduced with permission).

The study concluded that for surface displacements of engineering significance, which they defined as approximately 5 cm, the mean annual frequencies of exceedance at both sites are less than about 10^{-7} a^{-1}. The sensitivity cases indicated that fault displacement hazard is most sensitive to changes that reduce the distance between a fault and site, especially for the faults closest to the sites.

After the PFDHA study was completed, RIZZO performed additional field and laboratory studies in the vicinity of the proposed Krško 2 sites that included tectonic geomorphic analysis, high-resolution seismic reflection and refraction, and a multi-method geochronology [165]. Results from this study were then compiled with other available data, with an emphasis on the Libna fault, the Stara Vas fault (the two closest faults to the Krško 2 sites), as well as several other faults considered in the PFDHA study. This follow-up fault characterization report concluded that the age constraint for the timing of the most recent displacement on the Libna fault has changed from younger than 140 000 years to younger than 1.8 million years or more. The report also concluded that the Stara Vas fault, if it exists, is currently not capable, and therefore need not to be included in a PSHA or PFDHA.

Work has continued to investigate faults and the tectonic setting of the proposed Krško 2 sites. If the PFDHA is updated, the new results will be taken into account.

5. CONCLUSIONS

As stated in Section 1, the objectives of this publication are to describe the state-of-the-art research and practice related to PFDHA and to assist Member States in following the recommendations of SSG-9 [2] for reevaluating fault displacement hazards at existing nuclear installations. These objectives are accomplished through detailed discussions that are organized into three sections: 1) surface faulting characteristics and data collection for PFDHA (Section 2); 2) PFDHA methodology (Section 3); and 3) case studies in which PFDHA was applied to nuclear installations (Section 4). In this final section, a brief summary is provided with discussions of state-of-practice, limitations, and recent developments in PFDHA.

Characteristics of co-seismic surface rupture are discussed in Section 2. Basic concepts of fault activity are introduced, including capable faults that have significant potential for displacement at or near the surface. Phenomena associated with co-seismic surface rupture are shown with examples. A classification of surface rupture is introduced that may be elucidated by considering an earthquake fault rupture that nucleates at depth and propagates laterally and toward the surface. During propagation, this earthquake may generate principal fault rupture on one or multiple stepping fault segments, parallel or subparallel fault planes, or branches with varying dip angles. Besides these principal ruptures, distributed coseismic displacement may also occur on minor faults or shears that are near but distinct from the principal faults where most of the seismic moment release occurred. Current PFDHA addresses the hazard associated with the principal fault rupture and distributed fault rupture as described above. In addition, a large earthquake may trigger rupture on distant faults. The phenomenon of the trigger is likely related to propagating seismic waves or strain, but currently there is no consensus on an objective classification for triggered rupture, and its inclusion in PFDHA models depends on the study. In their analyses of distributed displacement, Youngs et al. in 2003 [58] included triggered ruptures, whereas Petersen et al. in 2011 [27] and Nurminen et al. in 2020 [59] excluded them. Earthquakes may also lead to ground deformation in the form of folds, flexural scarps or bending and warping of surfaces, depending on fault dip and/or local geology. However, this publication does not address these broader manifestations of co-seismic deformation.

Methods for collecting surface rupture data are also discussed in Section 2. These methods include traditional field mapping and more recently developed remote-sensing techniques. Field mapping gives directly fundamental sources of data for describing morphological features and surface faulting from field observations. Therefore, traditional field methods provide reliable measurements of localized displacements, and offer insights into local interactions between the landscape, near-surface soil and rock conditions, and surface rupture. Remote-sensing techniques increase data coverage and data precision significantly, making it possible to sample both on-fault and off-fault displacement in a uniform and systematic way. The combination of traditional field mapping and newer remote sensing techniques contributes to the development of robust surface rupture datasets.

Observations show that surface rupturing accompanying earthquakes is a complex phenomenon. The occurrence of surface rupture and the amplitude of displacement are influenced by the local geological environment, including fault geometry and shallow subsurface conditions. Available surface faulting datasets for PFDHA, however, are scarce as discussed in Section 2.5. Existing datasets mostly do not provide detailed descriptions of the complexity of surface faulting, nor do they include characterization of subsurface or near-surface material properties. Often the only parameters included are earthquake magnitude, focal mechanism, and site location relative to the fault. Because these existing datasets are based on measurements on discrete offset features encountered along the rupture, they do not provide the resolution to quantify ground deformation along the rupture between discrete features, nor do they provide information to quantify large-aperture deformation in a broader zone across the fault.

As discussed in Section 2.6, recent efforts have been made to build worldwide and unified databases of surface rupture for fault displacement hazard analyses. Two such efforts include the European-led SURE database project and the U.S.-led FDHI project. The SURE database includes three tables: a displacement observation point table, a rupture section table, and an earthquake table [62]. It also includes geo-referenced GIS files of surface rupture. The FDHI project led by the University of California at Los Angeles has developed a structured relational database that can accommodate both older data from field measurements and newer, high resolution, imagery-based datasets [63]. These two database building efforts have increased the amount of offset displacement data available for future PFDHA modelling efforts and have provided database structures that improve data reliability and quantification of uncertainty. These databases have also increased the type of information available for future modelling efforts, such as the inclusion of inelastic strain measurements, a wider range of slip parameters, and site-specific parameters such as geology.

PFDHA methodologies are described in Section 3. There are two basic approaches: the earthquake approach and the displacement approach (also known as the direct approach). The earthquake approach is similar to the standard PSHA for evaluating ground motion hazards. In the earthquake approach, rupture displacement is related to the occurrence of earthquakes through scaling relations and/or displacement distribution functions. In the calculation, traditional ground motion attenuation relations are replaced by magnitude- and position-dependent fault displacement distribution functions, and hazard is computed through integration over magnitude, rupture location, rupture distance, and probability distributions for displacement. In contrast to the earthquake approach, the displacement approach to PFDHA assesses annual exceedance frequency directly from displacement observations at a site and the associated rate of occurrences. The displacement approach is recommended if there are sufficient paleoseismic data to determine recurrence intervals and amplitudes of displacement events. This is because exceedance probability can be calculated by directly integrating a displacement probability density function that is established using fault- and site-specific displacement data, and there are fewer assumptions to be made about the applicability of ergodic models to a particular site.

PFDHA equations can be separated into source characterization and fault displacement model components. Source characterization for the displacement approach can be as simple as measuring the amplitudes of displacement events and determining frequency or rate of displacement events by dating offset features. Rate of displacement events may also be estimated from fault slip rate and average displacement of each event at the site. Source characterization for the earthquake approach is similar to source characterization for PSHA. Therefore, established source models for PSHA can be adopted for PFDHA and existing guidance documents in PSHA can be valuable references for PFDHA. Source characterization for the earthquake approach often consists of two main components, source geometry and earthquake recurrence models, with the latter consisting of three main elements: temporal recurrence model, the magnitude distribution, and the overall moment rate, as discussed in detail in Section 3.2 of this publication.

Fault displacement models are the essential components that are unique to PFDHA. Currently available earthquake-approach fault displacement models for principal and distributed displacements are empirically based. These models include terms that characterize the conditional probability of displacement at a site of interest, and the displacement exceedance probability given the occurrence of non-zero displacement. The displacement exceedance probabilities currently available use common statistical forms including the Gamma distribution, Beta distribution, and log-normal distribution. Model parameters for these forms are empirically determined from fault displacement data. Using the example form of a log-normal distribution, median displacement and standard deviation are calculated using empirical attenuation relationships that are functions of earthquake magnitude (or average displacement estimates given magnitudes), location on or off a fault, and other parameters.

As a pre-condition for PFDHA, it is necessary to have a quality map of fault traces in the area surrounding the site of interest so that sources may be identified and the location of the site relative to known faults can be measured. In Section 3.3.2, methods to incorporate rupture location uncertainty in PFDHA are discussed. Location uncertainty, like many other uncertainties, includes an epistemic component and an aleatory component. Hazard estimates from PFDHA can be improved if epistemic location uncertainty is reduced by improving the accuracy of mapped fault traces and if aleatory variability is adequately quantified from site-specific studies.

Physics-based numerical simulations are discussed in Section 3.3.4 as potential tools to improve models of surface rupture probability and displacement amount for both principal and distributed faulting. These models accounted for fault geometry, physical rupture criteria to break the free surface, the 3-D stress field, and geological site conditions, and their use may help fill in gaps in empirical datasets or help evaluate model uncertainties. Key issues needed to constrain such models include selection of frictional constitutive laws and seismologically important parameters such as stress drop and fracture energy. The importance of software verification and numerical model validation are also emphasized.

Hazard results, uncertainties, and their application for sites of interest are discussed in Section 3.4. Preparation of well-defined and clearly documented inputs that incorporate aleatory and epistemic uncertainties are emphasized. NUREG-2213 [145] can be referenced for guidance on proper documentation and procedure for incorporating uncertainties in PFDHA. Applications of PFDHA results often require additional site-specific geological and geotechnical information that needs to be determined on a case-by-case basis.

Three case studies are provided in Section 4 to illustrate the application of PFDHA for proposed or existing nuclear installations. These include the proposed geological repository for high-level nuclear waste at Yucca Mountain (Nevada, USA), the Diablo Canyon Power Plant (California, USA), and the Krško Nuclear Power Plant (Slovenia).

For the Yucca Mountain case study, both the earthquake approach and the displacement approach were applied. Estimated fault displacements were 0.1 cm or less for a return period of 100 000 years (annual frequency of exceedance of 10^{-5}), except for block-bounding faults (the Bow Ridge and the Solitario Canyon faults). There were large uncertainties in hazard estimates due, partly, to large differences in mean displacement estimates by different expert teams. The uncertain results were also attributed to lack of experience in assessing fault displacement hazards and limited data to constrain fault parameters.

In the Diablo Canyon Power Plant case, PFDHA was performed to estimate secondary displacement hazard from a newly discovered offshore strike-slip fault less than 1 km away. Results were presented as annual frequency of exceedance associated with specific displacement amplitudes that the structural components can tolerate. Comparison of the annual frequency of exceedance at these test displacement amplitudes with the annual core damage frequency of the plant led to a conclusion that fault displacement hazard is negligible.

The Krško Nuclear Power Plant is located in south-eastern Slovenia. This region is characterized by transpressional tectonics related to complex interactions among microplates and tectonic domains in the convergence zone between the African and European plates. Several faults near the plant were studied specifically for the purpose of assessing fault displacement hazards using the earthquake approach of PFDHA. The study concluded that the mean annual exceedance probabilities were less than 10^{-7} a^{-1} for surface displacements of engineering significance (about 5 cm). Sensitivity analyses indicated that estimated fault displacement hazard is most sensitive to site-to-fault distance, especially for the faults closest to the sites, illustrating the importance of locating faults accurately for displacement hazard assessment.

These case studies demonstrated techniques of PFDHA application with different project objectives and in different tectonic settings. Each case had different data needs, required different data inputs, and faced difference challenges. In all cases, the PFDHA implemented the empirical approaches described in Section 3. Together, these cases portray a realistic picture of the current state of PFDHA application that relies on empirical equations developed using limited amount of data from traditional field measurements and mapping without consideration of shallow subsurface condition.

Available empirical models for distributed displacement analyze offset on discrete features that may account for only a portion of the total off-fault deformation associated with an earthquake. Although the topic is beyond the scope of this publication, earthquake fault ruptures may produce non-discrete surface deformation (in addition to, or instead of, discrete displacements) that can be damaging to structures built on top of the deformation zone. The American Nuclear Society Standards Committee Working Group ANS-2.30 [94] distinguished discrete surface fault rupture from tectonic surface deformation and provides guides for probabilistic hazard assessment for both.

Decades of dedicated data collection and well-coordinated research and model development efforts have led to a wide range of sophisticated empirical and physics-based models to characterize ground motion hazard and associated uncertainties. In contrast, available fault displacement data and models are limited and not nearly as well developed, which makes adequate assessment of mean hazard and hazard uncertainty challenging. Fault displacement models usually have simple functional forms and are easy to implement in PFDHA. However, careful examination of underlying data and model limitations is strongly recommended when applying these models. Available region-, fault-, and site-specific data can be used to augment or modify available models. For example, in the Diablo Canyon Power Plant case, the conditional probability of surface rupture was determined based on site-specific knowledge of the fault thickness and dip rather than global empirical models.

Some recent research developments discussed in Sections 2 and 3 have great potential for application in PFDHA, including the rapidly increasing amount of high-resolution imagery-based data, physics-based simulation models, and consideration of shallow subsurface geology. Considerable progress in PFDHA can be expected in the near future as the SURE and FDHI database building efforts provide reliable data to improve empirical models and help guide physics-based modelling efforts.

APPENDIX I. EXAMPLE OF EXTENSIVELY DOCUMENTED EARTHQUAKE SURFACE RUPTURES; THE 2016 AMATRICE AND NORCIA EARTHQUAKES IN CENTRAL ITALY

Between August 2016 and February 2017, Central Italy was severely shaken and damaged by a sequence of nine earthquakes with magnitudes M_W ranging between 5.0 and 6.5. The first event (24 August 2016, M_W 6.0 Amatrice) led to a ~5 km long surface rupture with a maximum and average offset of 30 and 12 cm, respectively, along the so-called Mt. Vettore fault system, as revealed by to the field survey of the Open EMERGEO task force, an international team of experts from major Italian research institutes and universities dealing with active tectonics, led by Italian Institute for Geophysics and Volcanology [170]. After the two subsequent large events (26 October 2016, M_W 5.9 Visso, and 30 October 2016, M_W 6.5 Norcia), ground breaks appeared across a very wide (> 400 km^2) and steep slope area, and were mapped due to the collaborative work of many geologists from different groups and countries within the Open EMERGEO task force [25]. The fault rupture extended over a distance of 28 km and its complex faulting pattern could be described due to a large set of oblique aerial pictures taken from a helicopter. A very large dataset of 7000 observation points has been gathered, with ~5000 measurements of offset: this is perhaps the most documented earthquake surface rupture ever recorded.

Figure 35 shows (i) purple and yellow ruptures associated, respectively, with the 24 August and 26 October events, which reactivation by the 30 October mainshock caused an increase in displacements; (ii) red ruptures that were formed exclusively by the 30 October earthquake.

The entire pattern of surface ruptures on the west-dipping primary fault is almost continuous along 2 to 4 km long segments and average displacement is around 30 cm with a kilometre-long sections above 1 m and in a few exceptional instances up to 2.5 m. The surface rupture map, besides the major rupture, shows many secondary ruptures of different types and position relative to the main fault. Several continuous (≥ 1 km) synthetic or antithetic segments appear less than 2 km off the main fault with typically 10−50 cm offsets, whereas several short to very short segments with centimetre scale displacement are mapped up to 12 km west of the major rupture.

As observed in other earthquakes worldwide (1954 M_W 7.1 Fairview Peak, 1983 M_W 6.8 Borah Peak), the Central Italy sequence has shown that mapped surface ruptures during normal faulting events can be significantly complex in detail, especially in earthquakes of M_W 6.5, and larger.

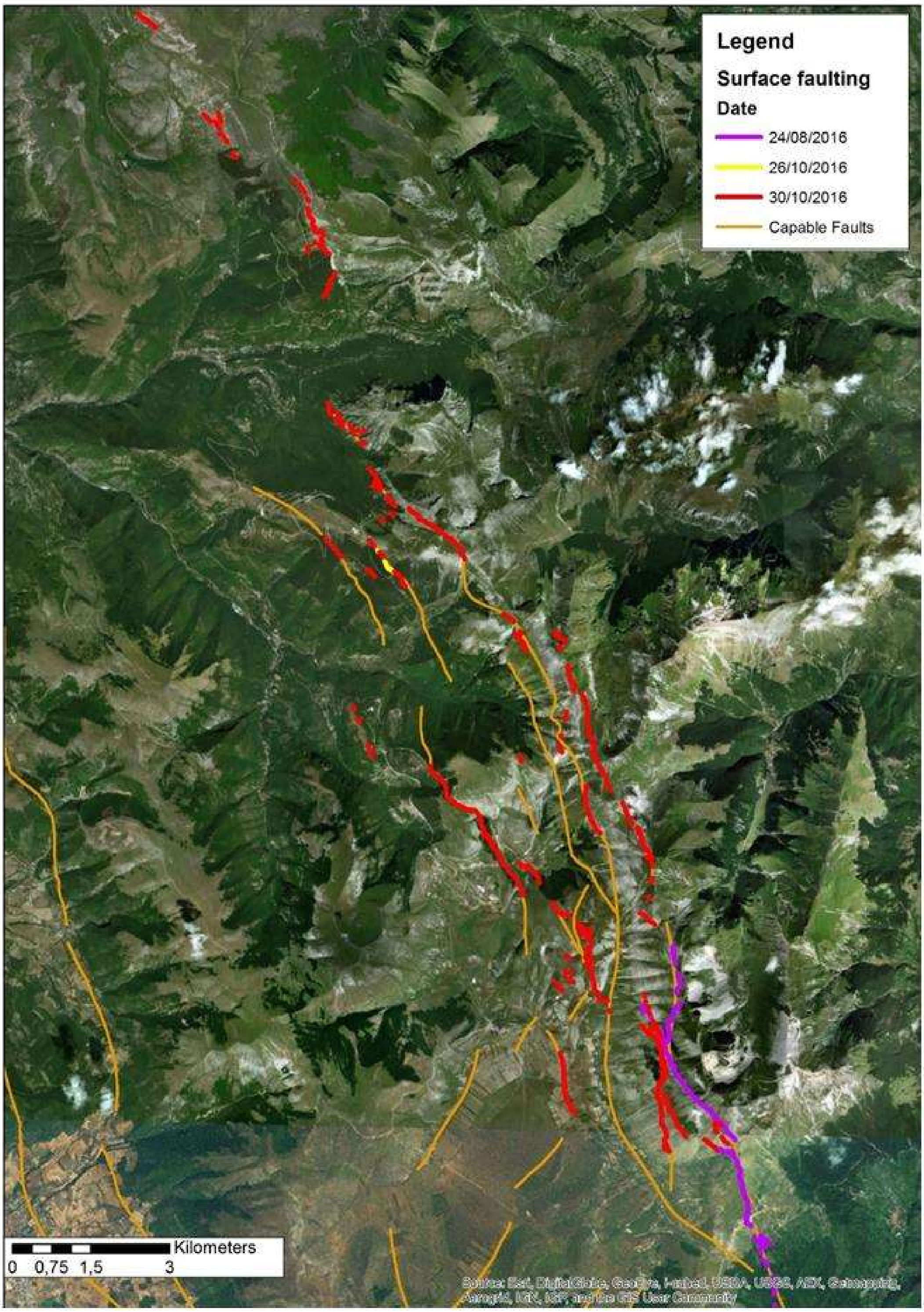

FIG 35. Summary map of surface faulting associated to the 2016 seismic sequence in Central Italy. In purple are pointed out the ruptures formed in the southern sector by the 24 August event (M_W 6.0 Amatrice), in yellow the ruptures associated to the 26 October event (M_W 5.9 Visso) in the northern sector, in red the ruptures formed by the 30 October earthquake (M_W 6.5 Norcia) [25]. Other capable faults in the area are mapped as orange lines.

APPENDIX II. DETAILED INFORMATION FOR EARTHQUAKE APPROACH

This appendix presents the detailed information for earthquake approach such as the probability density function and the conditional probability for PFDHA. Appendix II.1 provides information for the principal fault and Appendix II.2 gives information for the distributed fault.

II.1. PRINCIPAL FAULT

II.1.1. Probability of surface rupture of principal fault

A probability of surface rupture of a principal fault for a given magnitude is described by the following logistic function:

$$P\left[sr \neq 0 \middle| m\right] = \frac{e^{a+bm}}{1+e^{a+bm}} \tag{19}$$

Table 9 shows the coefficients of Eq. (19).

TABLE 9. COEFFICIENTS FOR EQ. (19).

a	***b***	**Faulting type**	**Reference**
-12.51	2.053	All slip	[5, 28]
-12.53	1.921	Normal slip	[58]
-7.30	1.03	Reverse slip	[36]
-32.03	4.90	Reverse and strike slip of Japan	[29]

Figure 12 indicates the probability of a surface rupture. The detailed descriptions of Figure 12 are provided in Section 3.3.1. The Japanese data in [29] shows a lower probability of surface faulting at small magnitudes (less than M_W 6.0), but significantly increasing the tendency from M_W 6.0 and more compare to other models. In addition, Takao et al. in 2013 [29] did not distinguish reverse faults from strike-slip faults since there is little difference between their probabilities derived from the Japanese data.

II.1.2. Slip exceedance probability of principal fault

Displacement along principal faults are normalized by either the maximum displacement *MD* or the average displacement *AD*, which are estimated by applying an empirical equation, such as Wells and Coppersmith [5]. The reason why normalized displacement is adopted is to be able to treat the disparate data equally. If large amounts of displacement data are compiled in the future, it will be possible to treat displacement data without normalizing. The conditional probability of slip exceedance $P[D > D_0 \mid l/L, m, D \neq 0]$ in Eq. (8) can be obtained by numerically convolving the probability distribution for displacements normalized by D/MD or displacements normalized by D/AD with log-normal distributions for *MD* or *AD*.

Youngs et al. in 2003 [58] derived displacement distributions for normal faulting, and Moss and Ross [36] proposed displacement distributions for reverse faulting. Takao et al. in 2013 [29] also proposed relationships for reverse and strike-slip faulting in Japan in terms of the maximum and the average displacement. The papers mentioned above used a beta distribution for a maximum displacement scaling, which is bound between 0 and 1. The beta distribution is expressed by Eq. (20):

$$F(y) = \frac{\Gamma(a+b)}{\Gamma(a)+\Gamma(b)} \int_0^y z^{a-1} (1-z)^{b-1}\, dz \tag{20}$$

where $F(y)$ is the cumulative probability that variable Y is less than or equal to a specific value y, $\Gamma(\cdot)$ is the gamma function, y is equal to D/MD, a and b are shape parameter and scale parameter of beta distribution and are functions of l/L.

The coefficients of Eq. (20) are shown in Table 10.

TABLE 10. COEFFICIENTS FOR EQ. (20).

a	***b***	**Faulting type**	**Reference**
exp (-0.705 + 1.138 l/L)	exp (0.421 - 0.257 l/L)	Normal slip	[58]
exp (0.713 + 0.901 l/L)	exp (1.74 - 1.86 l/L)	Reverse slip	[36]
exp (0.70 - 0.87 l/L)	exp (2.30 - 3.84 l/L)	Reverse and strike slip of Japanese (L more than 10 km)	[29]
0.91	1.90	Reverse and strike slip of Japanese (L less than 10 km)	

As for the average displacement, [58], [36] and [29] used a gamma distribution. The gamma distribution has the following form:

$$F(y) = \frac{1}{\Gamma(a)} \int_0^{y/b} e^{-t} t^{a-1} dt \tag{21}$$

where $F(y)$ is the cumulative probability that variable Y is less than or equal to a specific value y, $\Gamma(\cdot)$ is the gamma function, y is equal to D/AD, a and b are shape parameter and scale parameter of gamma distribution, respectively, and are functions of l/L.

The coefficients of Eq. (21) are shown in Table 11.

Compiled data in [58] are shown from Figures 36 to 39. As shown in Figure 38 and 39, Takao et al. in 2013 [29] divided the displacement distribution function into two groups (more than 10 km and less than 10 km) on the basis of the tendency that the relationship between the position along the principal fault and displacement is weak when the length of the principal fault is less than 10 km. Graphs comparing among these three papers are drawn in Figure 40 for *D*/*MD*, and in Figure 41 for *D*/*AD*, respectively.

TABLE 11. COEFFICIENTS FOR EQ. (21) FOR PRINCIPAL FAULT DISPLACEMENT.

a	***b***	**Faulting type**	**Reference**
exp (-0.193 + 1.628 l/L)	exp (0.009 - 0.476 l/L)	Normal slip	[58]
exp (0.574 - 2.29 l/L + 19.9 $(l/L)^2$ - 30.4 $(l/L)^3$)	exp (-1.05 + 6.60 l/L - 34.6 $(l/L)^2$ + 50.3$(l/L)^3$)	Reverse slip	[36]
exp (0.70+0.34 l/L)	exp (-1.40+1.82 l/L)	Reverse and strike slip of Japanese (*L* more than 10 km)	[29]
1.53	0.58	Reverse and strike slip of Japanese (*L* less than 10 km)	

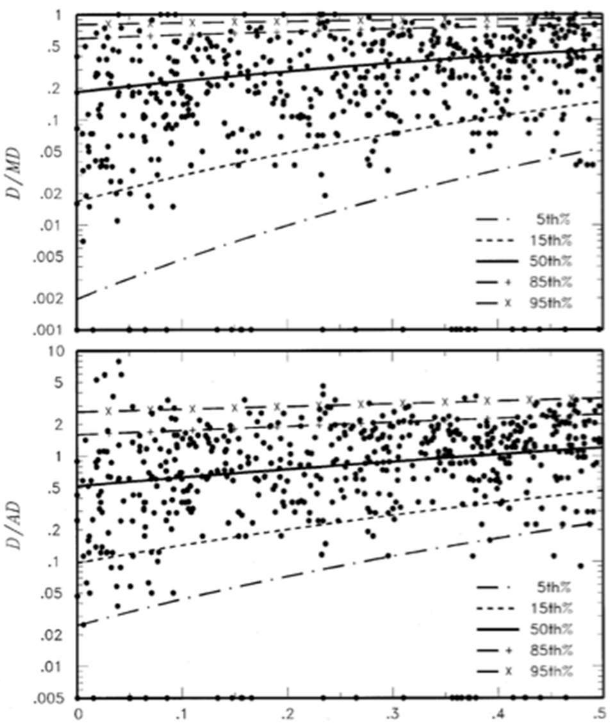

FIG 36. Combined data set for D/MD and D/AD from [171] for 11 normal faulting earthquakes. The curves show the percentiles of the beta (D/MD, Eq. (20)) and gamma (D/AD, Eq. (21)) distributions fit to the data (reproduced with permission from [58]).

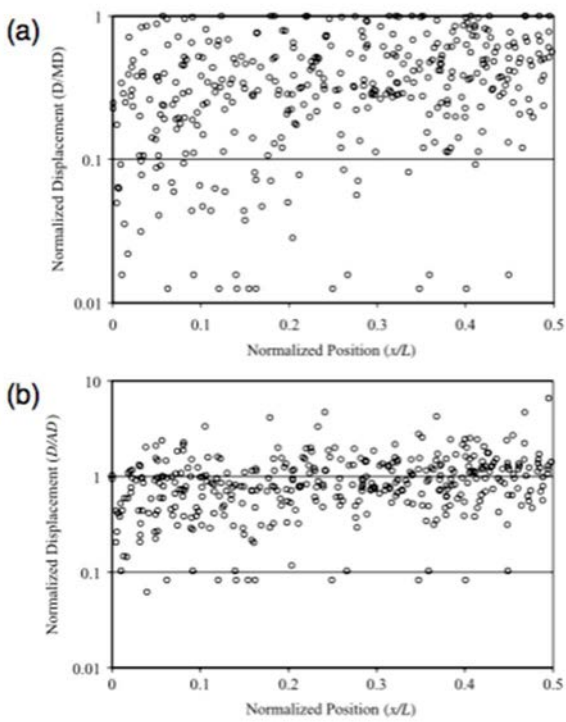

FIG 37. Combined dataset for normalized slip measurements from nine reverse faulting events plotted as a function of x/L; x/L=0 is treated as the beginning (or end) of the fault rupture. (a) Displacement normalized by the average surface displacement. (b) Displacement normalized by the maximum surface displacement measured. The beta distribution of (a) and gamma distributions of (b) correspond to Eq. (20) and Eq. (21), respectively (from [36] with permission).

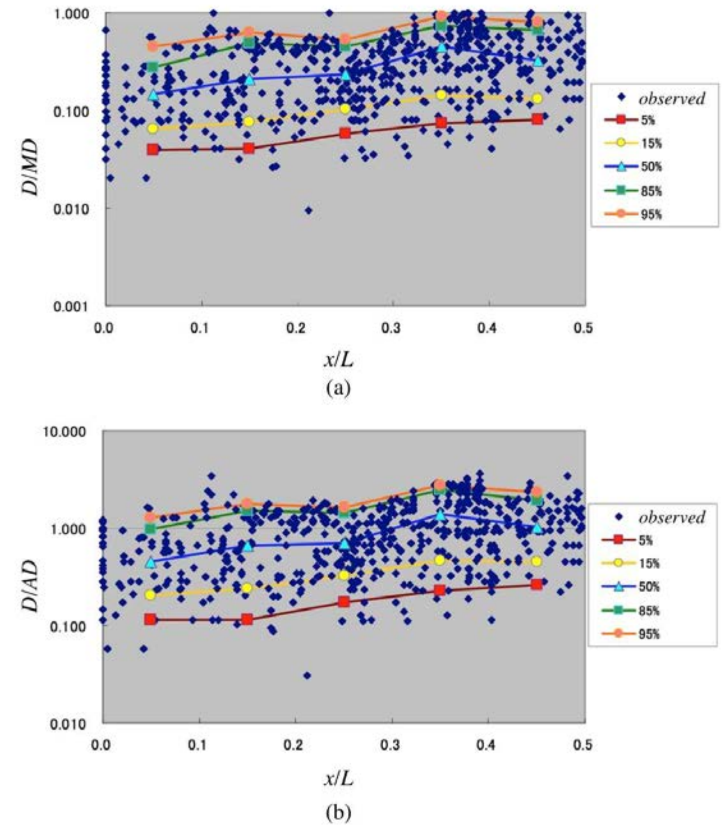

FIG 38. Combined dataset for normalized slip measurements from Japanese earthquakes (L more than 10km). (a) Displacement normalized by the maximum surface displacement (b) Displacement normalized by the average surface displacement. The solid lines in the figure represent each percentile of the observed data. The beta distribution of (a) and gamma distributions of (b) correspond to Eq. (20) and Eq. (21), respectively (from [29] with permission).

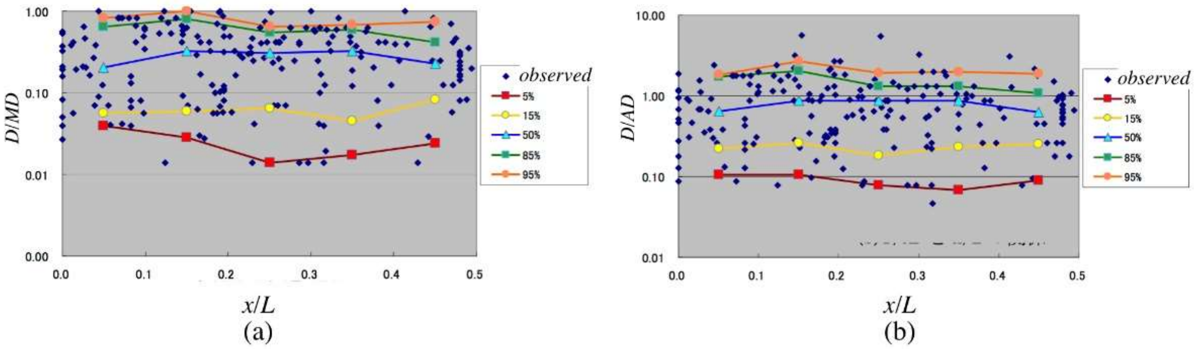

FIG 39. Combined dataset for normalized slip measurements from Japanese earthquakes (L less than 10km). (a) Displacement normalized by the maximum surface displacement (b) Displacement normalized by the average surface displacement. The solid lines in the figure represent each percentile of the observed data. The beta distribution of (a) and gamma distributions of (b) correspond to Eq. (20) and Eq. (21), respectively (from [29] with permission).

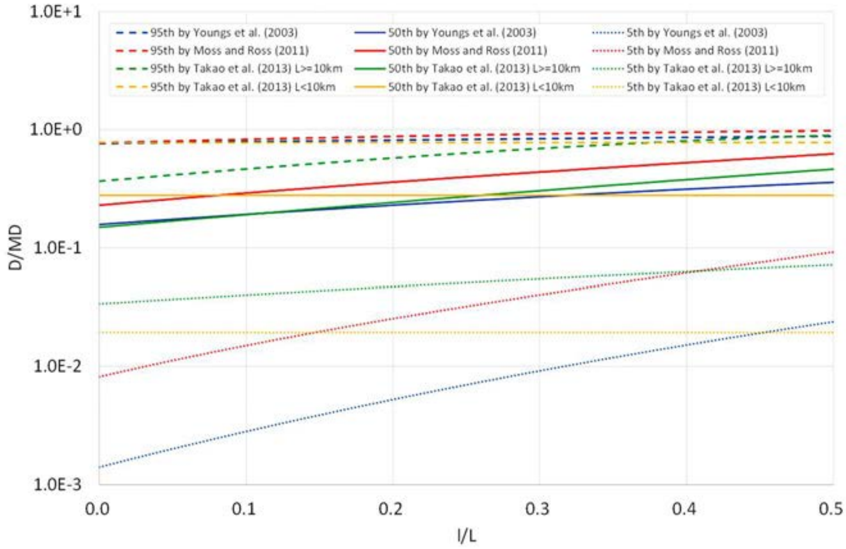

FIG 40. Distribution of D/MD along the principal fault.

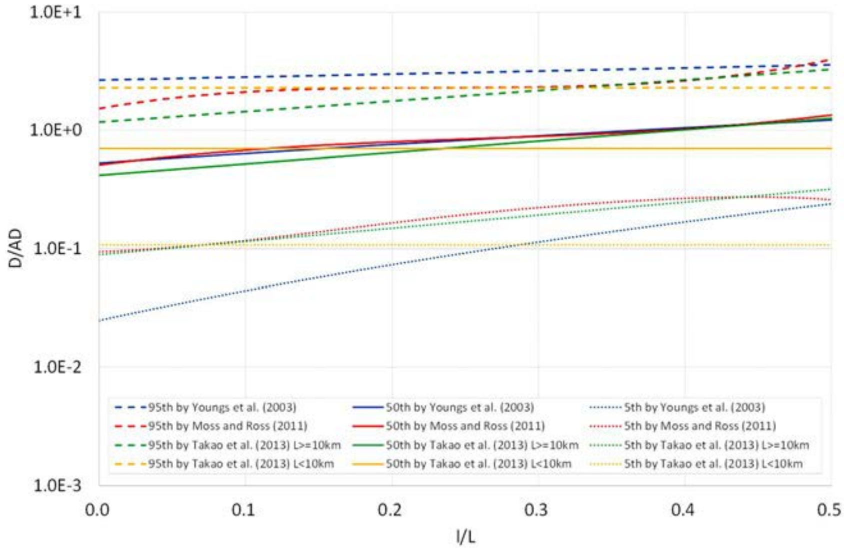

FIG 41. Distribution of D/AD along the principal fault.

Petersen et al. in 2011 [27] proposed three types of equations regarding *D*/*AD* that can consider a taper tendency of the displacement when approaching the ends of the fault:

$$\ln\left(D/AD\right)=\begin{cases}8.2525(l/L)-2.3010, & l/L<0.3008\\ 0.1816, & l/L\geq 0.3008\end{cases} \tag{22}$$

$$\ln\left(D/AD\right)=14.2824(l/L)-19.8833(l/L)^2-2.6279 \tag{23}$$

$$\ln\left(D/AD\right)=3.2699\sqrt{1-\frac{1}{0.5^2}\left[(l/L)-0.5\right]^2}-3.2749 \tag{24}$$

The standard deviations of Eqs (22), (23) and (24) are 1.2962 (l/L < 0.3008), 1.0013 (l/L > 0.3008), 1.1419 and 1.1419 in ln (natural log) unit, respectively. Petersen et al. in 2011 [27] also provided an attenuation relation for non-normalized displacements:

$$\ln\left(D\right)=\begin{cases}1.7969m+8.5206(l/L)-10.2855, & l/L<0.28041-3.6500\times10^{-3}m\\ 1.7658m-7.8962 & l/L\geq 0.28041-3.6500\times10^{-3}m\end{cases} \tag{25}$$

$$\ln(D)=1.7895m+14.4696(l/L)-20.1723(l/L)^2-10.54512 \tag{26}$$

$$\ln(D)=3.3041\sqrt{1-\frac{1}{0.5^2}\left[\left(l/L\right)-0.5\right]^2}+1.7927m-11.2192 \tag{27}$$

where m is earthquake magnitude and D is in centimetres. The standard deviations of Eqs (25), (26) and (27) are 1.2906 ($l/L < 0.28041 - 3.6500 \times 10^{-3}\ m$), 0.9624 ($l/L > 0.28041 - 3.6500 \times 10^{-3}\ m$), 1.1346 and 1.1348 in ln unit, respectively. Figure 42 and 43 show the principal-fault displacement data compiled in [27].

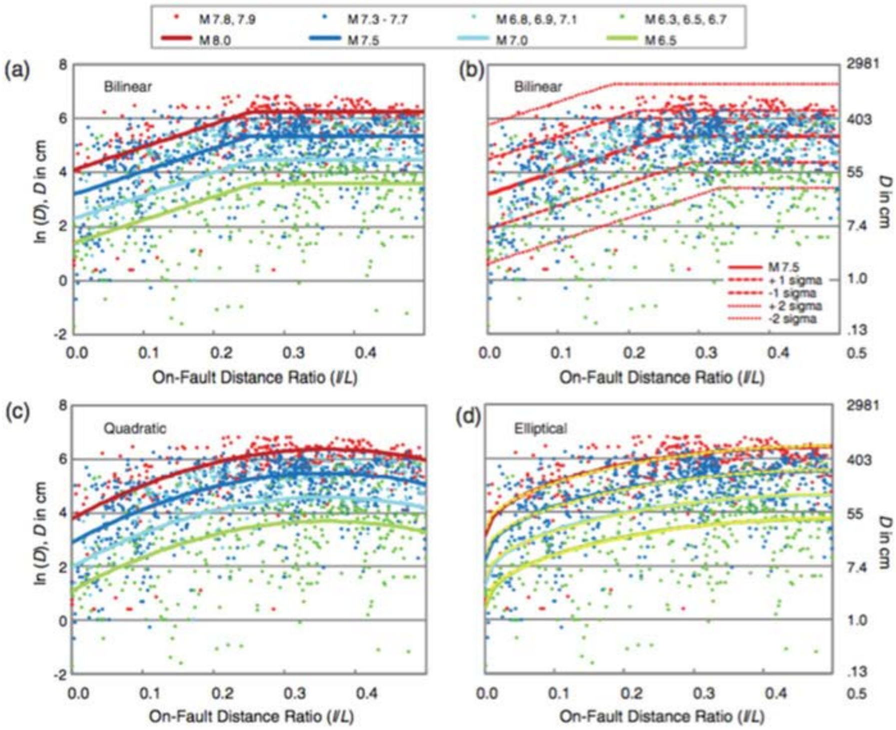

FIG 42. Principal-fault displacement data color-coded by magnitude and regression models (a) with bilinear regression lines for M_W 6.5 to 8.0, Eq. (25), (b) with the bilinear regression lines for M_W 7.5 and uncertainties of ± 1 and ± 2 standard deviations, (c) with quadratic regression curves for M_W 6.5-8.0, Eq. (26), (d) with the elliptical regression curves for M_W 6.5 to 8.0, Eq. (27) as well as regression curves based on [55] functional form (dashed yellow curves) (from [27] with permission).

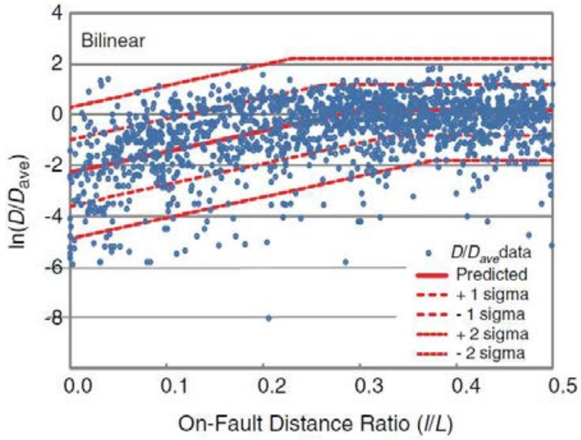

FIG 43. Normalized principal-fault displacement data (D/AD) with bilinear regression line (Eq. (22)) and uncertainties (± 1 and ± 2 standard deviations) (from [27] with permission).

The relationships between *l/L* and *D/AD* using bilinear, quadratic, and elliptical function are plotted in Figure 44. In addition, Petersen et al. in 2011 [27] employed a log-normal distribution, whereas other researchers adopted a gamma distribution for *D/AD*.

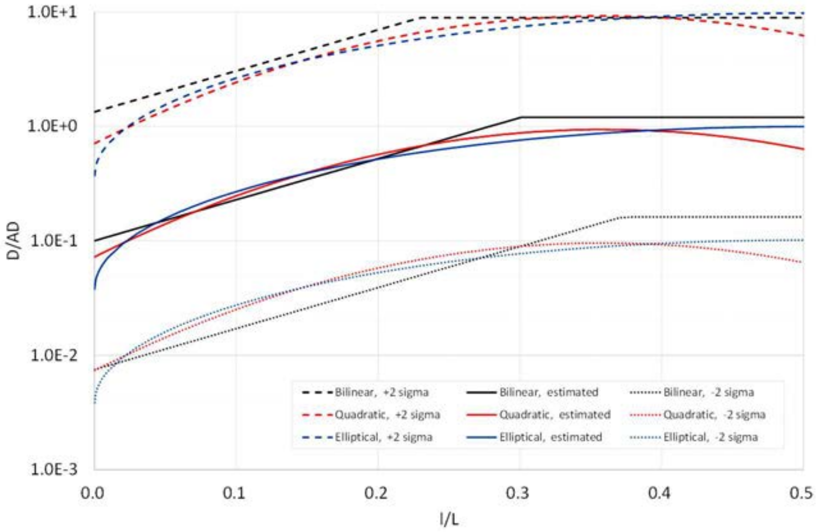

FIG 44. Distribution of D/AD using taper model.

While the aforementioned researchers proposed the equations which form symmetric displacement distribution about $l/L = 0.5$, Wesnousky in 2008 [57] described that asymmetric functions such as asymmetric sine, asymmetric ellipse, and asymmetric triangle, provide a better estimation of observed displacement distributions than flat or symmetric functions. However, if an asymmetric distribution was adopted in PFDHA, other issues, which have not been sufficiently solved, would arise, such as the largest point along the principal fault and the most appropriate function for distribution.

II.2. DISTRIBUTED FAULT

II.2.1. Surface rupture probability of distributed faulting

As described in [58], the distributed fault data were digitized by constructing a raster scan of each map using a 0.5 km ×0.5 km cell size, and other researchers performed in the same manner but the pixel size for the analysis depends on a study.

[58] and [29] derived an equation to calculate the probability of a surface rupture of the distributed faulting at a point using the logistic regression model as:

$$P\left[sr \neq 0 \middle| r, m\right] = \frac{e^{f(r,m)}}{1+e^{f(r,m)}} \tag{28}$$

Youngs et al. in 2003 [58] derived $f(r, m)$ for normal faults as:

$$f\left(r,m\right) = 2.06 + \left(-4.63 + 0.118m + 0.682h\right)\ln\left(r+3.32\right) \tag{29}$$

Where r is the distance from the principal fault to a distributed fault in kilometres, m is the earthquake magnitude, and h is an indicator variable taking the value of 1 for hanging wall side of the rupture and 0 for the footwall side of the rupture.

Figure 45 shows the surface rupture probability of distributed faulting in [58]. According to [29], for reverse and strike-slip faults in Japan, $f(r, m)$ is expressed as:

$$f\left(r,m\right)=-3.839+\left(-3.886+0.350m\right)\ln\left(r+0.200\right) \tag{30}$$

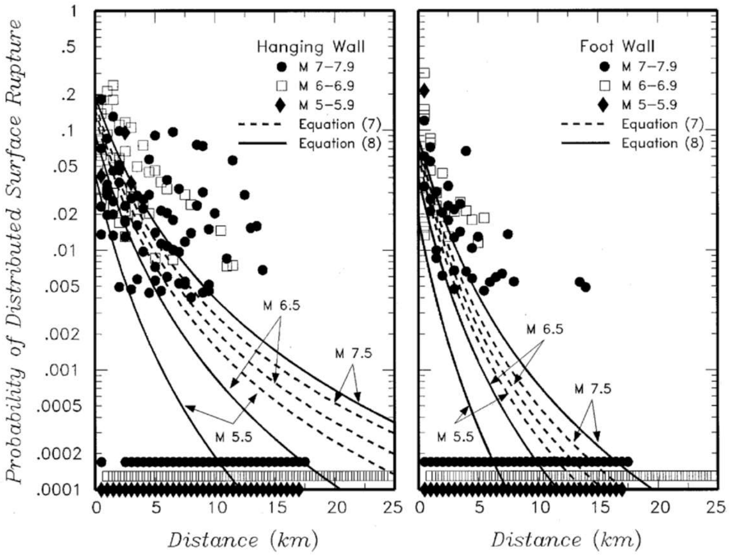

FIG 45. Conditional probability of slip for distributed faulting. Symbols show the rate of occurrence of distributed faulting for individual earthquakes by [35] (after [58]). Eq. (7) in the figure corresponds to Eq. (29).

In addition, Takao et al. in 2014 [61] proposed another type of equation which depends on the cell size (side length of a square considered for calculating the probability of a surface rupture), but does not depend on the magnitude:

$$f\left(r\right)=C_1+C_2\ln\left(r+C_3\right) \tag{31}$$

The coefficients of Eq. (31) are shown in Table 12.

TABLE 12. COEFFICIENTS FOR EQ. (31) (From *[61]*).

Cell size (m^2)	**C_1**	**C_2**	**C_3**
500 x 500	-3.859	-1.499	0.2
250 x 250	-4.903	-1.459	0.2
100 x 100	-6.135	-1.427	0.2
50 x 50	-6.988	-1.410	0.2

The surface rupture probability of distributed faulting in [29, 61] are shown in Figure 46 and 47, respectively.

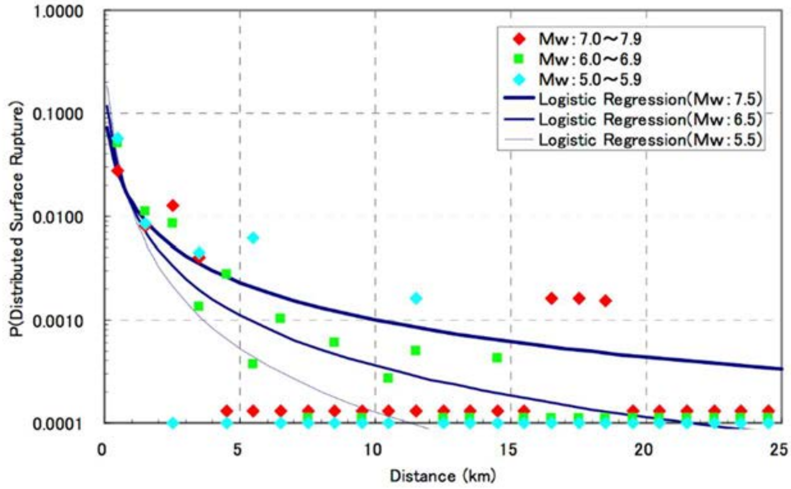

FIG 46. Probability of distributed fault rupture with regression equation and data averaged in bins for 500 m×500 m cells in accordance with Eq. (30) (from [29] with permission).

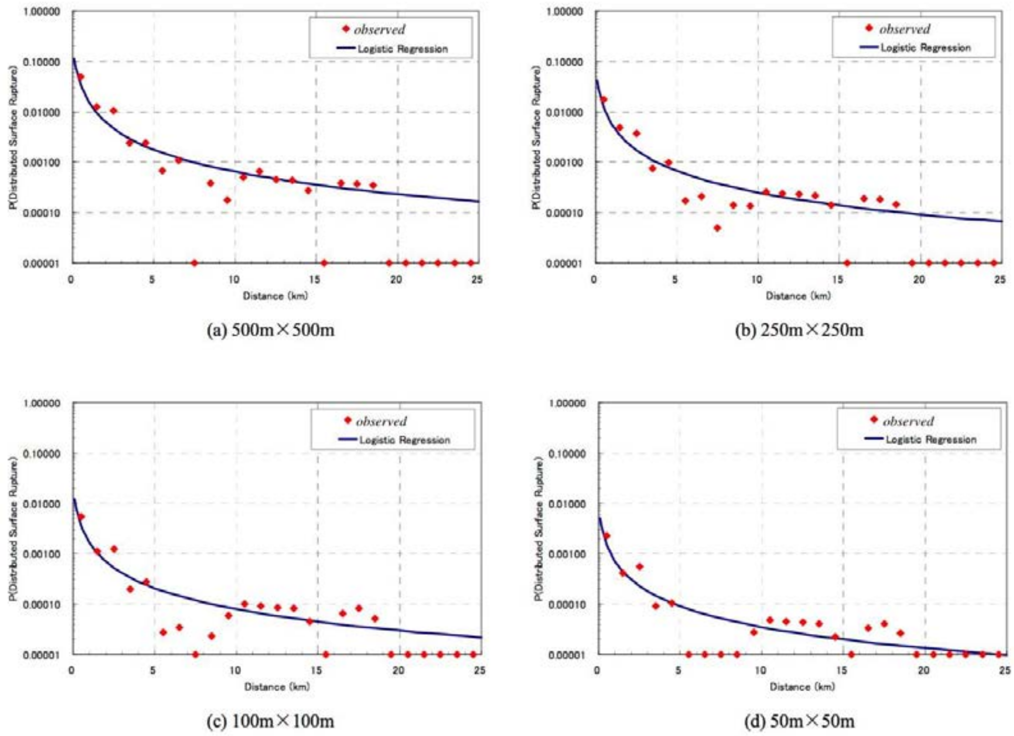

FIG 47. Probability of distributed fault rupture with regression Eq. (31) and data averaged in bins for (a) 500 m×500 m cells and (b) 250 m×250 m cells and (c) 100 m×100 m and (d) 50 m×50 m (from [61] with permission).

In contrast, to express the probability of a surface rupture of distributed faulting, Petersen et al. in 2011 [27] assumed a power function as:

$$\ln(P) = a(z)\ln(r) + b(z) \tag{32}$$

where $a(z)$ and $b(z)$ are the parameters that depend on the area (z) (see the interpolation points in [27] when calculating the probability in the area which is very close to the principal fault), r is the distance from the principal fault to a distributed fault in metres, and z is the cell size of the area considered for calculating the probability of a surface rupture.

The coefficients of Eq. (32) are shown in Table 13.

TABLE 13. COEFFICIENTS FOR EQ. (32) (From *[27]*).

Cell size (m^2)	***a***	***B***	**standard deviation**
200 x 200	-1.1538	4.2342	1.0177
150 x 150	-1.0934	3.5526	1.0188
100 x 100	-1.0114	2.5572	1.0917
50 x 50	-0.90000	0.9866	1.1470
25 x 25	-1.1470	2.1046	1.2508

The surface rupture probability of distributed faulting in [27] is shown in Figure 48. Figure 49 shows the comparison in terms of dependency on magnitude. Blue lines for reverse and strike-slip faults in [29] show relatively higher dependency on the magnitude, whereas the black and grey lines for normal faults in [58] indicate lower dependency on that. Figure 50 indicates the comparison regarding the dependency on the cell size. When comparing the red lines with the blue lines under the same condition (the same cell size), the probability based on [27] is higher than that in [61]. Regarding this difference, Suzuki and Annaka in 2018 [172] described as follows:

> "…surface fault displacements associated with earthquakes in Japan are more difficult to be found than those in other regions. The soft subsurface layer that exists widely in Japan may be the cause of those differences. The differences in vegetation and geomorphic characteristics may affect the detectability of small surface fault displacements." [172]

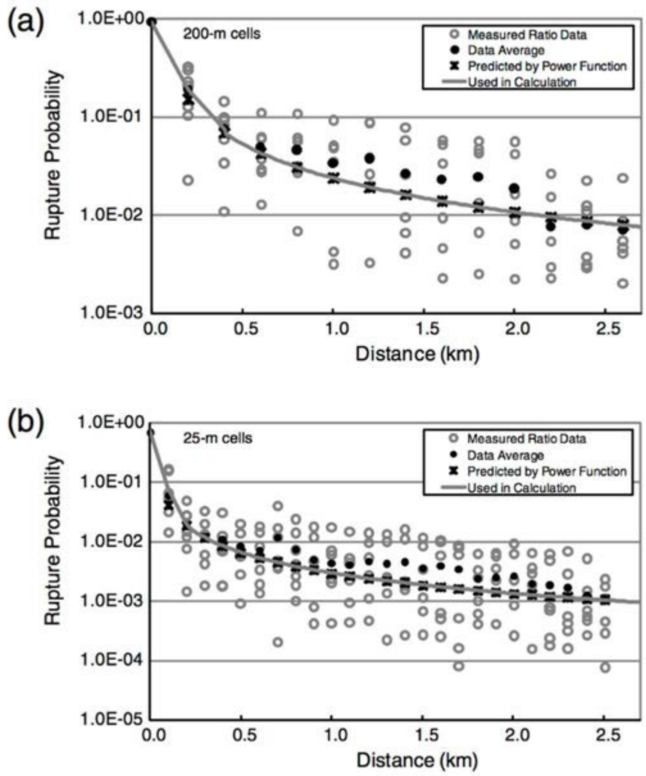

FIG 48. Probability of distributed-fault rupture displacement with regression Eq. (32) and data averaged in bins for (a) 200 m×200 m cells and (b) 25 m×25 m cells (from [27] whit permission).

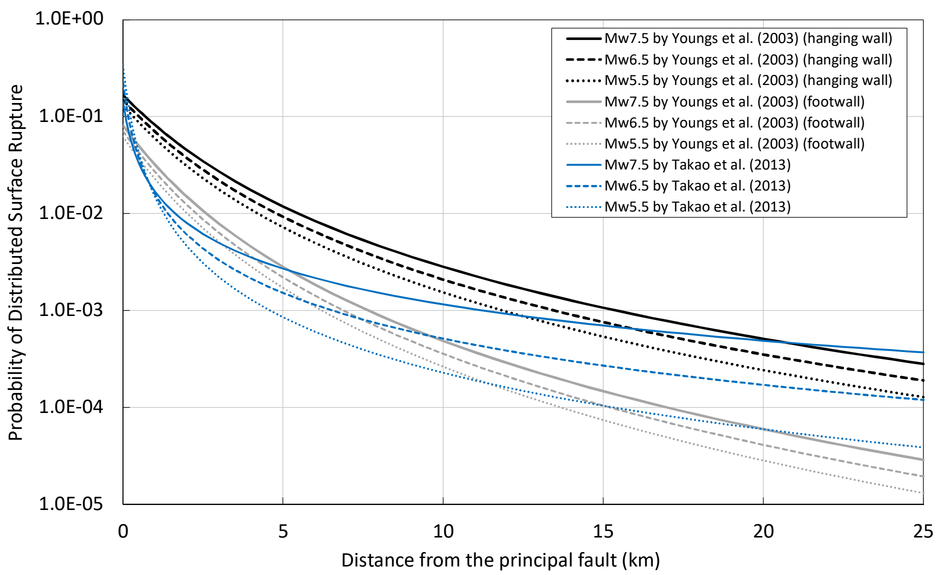

FIG 49. Probability of distributed surface rupture depending on Mw.

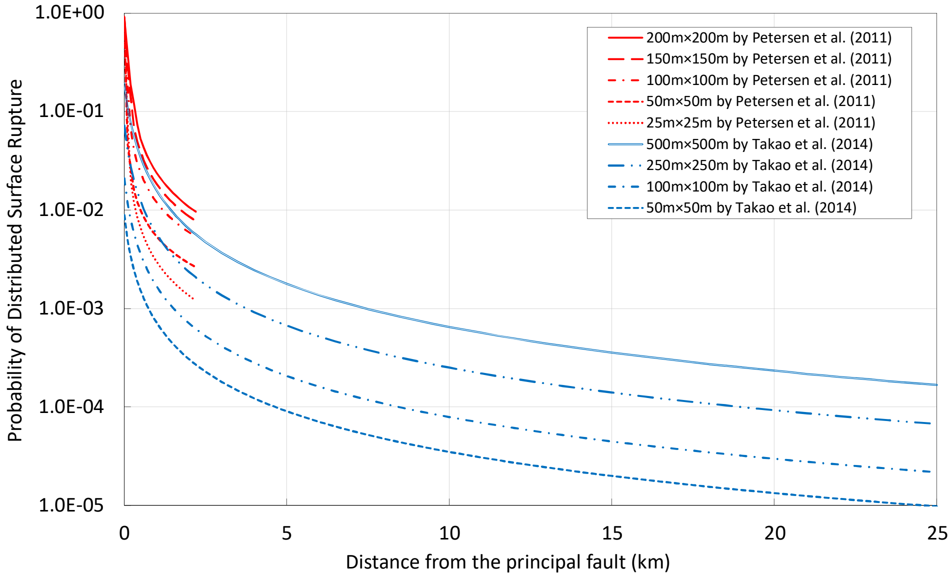

FIG 50. Probability of distributed surface rupture depending on cell size.

The methodology published in [59] proposes several methodological novelties. As an alternative to the ‘gridding’ approach the author proposed a new approach called ‘slicing’ (Figure 51). First, the distinction between the primary and the distributed rupture is done using a threshold distance of 5 m on both hanging wall and footwall sides of the primary fault, defining in total a 10 m wide zone within which all the surface ruptures are excluded from the analysis. Slicing allows the analysis of the distributed rupture, independently from the position along the strike of the primary fault, as it generalizes the distributed rupture occurrence considering only the distance to the principal fault. Adding a multinomial logistic model enables the computation of either occurrence or absence of distributed ruptures using a linear combination of prediction variables. The probability for at least a partial simple distributed rupture (*Pf*) is calculated from Eq. (33):

$$\ln(Pf\,/\,(1-Pf)) = a + b_1 X_1 + b_2 X_2 \tag{33}$$

where X_1 and X_2 are the magnitude and the distance from the principal fault, respectively, and the coefficients a, b_1 and b_2 are 8.5431, -1.5586, and 0.0099 for footwall, respectively, and 2.9179, -0.5566, and 0.0030 for hanging wall, respectively. Figure 52 illustrates the resulting probabilities for the three magnitude groups. Then, a Monte Carlo approach is used to estimate the probability of surface rupturing at a site located at some distance from the principal fault. For each Monte Carlo iteration, the distributed rupture length is sampled and randomly placed along the strike of the principal fault. The range of the lengths of the distributed ruptures, and the number of distributed ruptures that can be placed along the strike of the *Pf* is a random number extracted from a uniform distribution bounded by the minimum length of the distributed rupture and the total (or summed) expected length of the distributed ruptures divided by the maximum lengths. The summed (or total) length of the distributed ruptures along the strike of the principal fault is based on the observed ratio (*F*) between the lengths of the distributed rupture with respect to the length of the principal fault for each earthquake in the dataset. As the curves in Figure 53 unveil, the ratio *F* shows a rapid decay with distance from the primary fault. Thus, two *F*-

values were considered for both hanging wall and footwall, two for less than 100 m and two for more than 100 m. For a given rupture length of the principal fault, the summed or total length of the distributed rupture that can occur along the strike is then calculated (length of principal fault × F). It is important to note that, doing so, each distributed rupture can have different lengths compatible with the total expected length. The probability of having a distributed rupture at a specific site is then given by counting the times a distributed rupture intersects the site with respect to the number of Monte Carlo iterations.

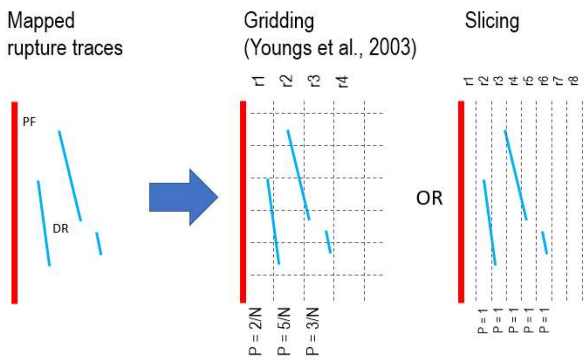

FIG 51. Principle of 'slicing' in comparison to gridding. From the map view the occurrence of the distributed ruptures (blue lines) is analysed in a cell (gridding) or within a slice (slicing) parallel to the principal fault (red line). The approach used for obtaining the probability of DR occurrence in slicing is independent of the fault-normal division into grids, and the completeness of the rupture tracing.

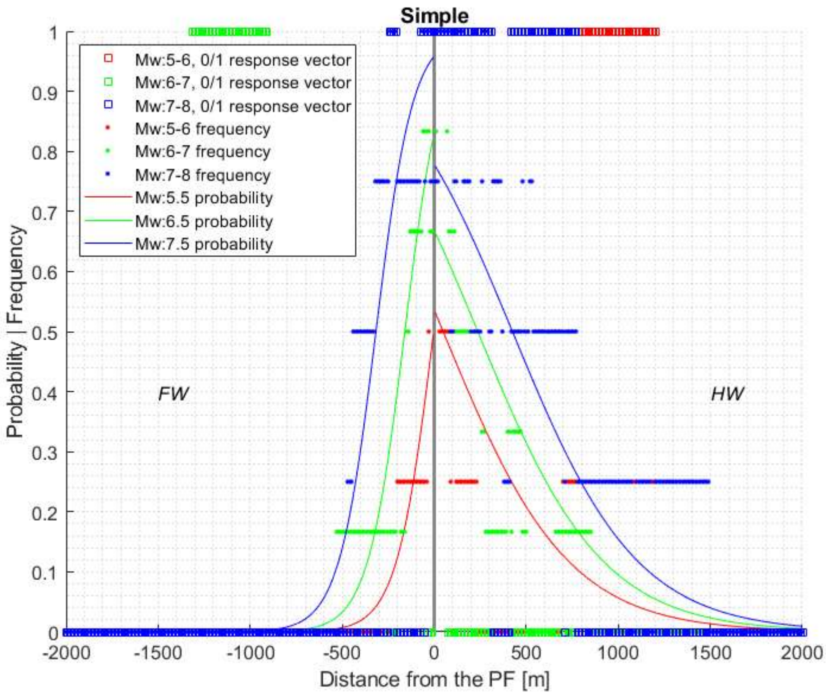

FIG 52. Logistic regressions of the distributed rupturing in the database indicating the probability of observing at least a partial distributed rupture (DR) as a function of distance from a principal fault (PF) on hanging wall (HW) and footwall (FW) sides. The squares show the response to the logistic regression of rupturing either occurring (1) or not occurring (0) at a given distance. The points show the DR frequency in respect to the total number of events int each Mw class, and the lines indicate the probability of at least a partial DR at a given distance.

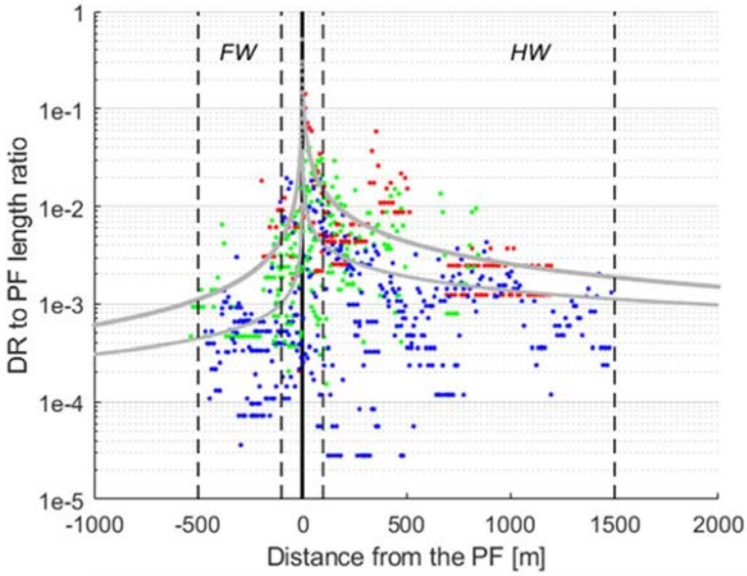

	F_{FW2}	F_{FW1}	F_{HW1}	F_{HW2}
Coefficient F	0.004	0.007	0.03	0.007
Validity range	100 – 500 m	5 – 100 m	5 – 100 m	100 – 1,500

FIG 53. Fraction of DRs lengths to PF lengths, and power fit as a function of distance from the PF: thicker fit to maximum value; thinner fit to "all" values, and the fixed values of coefficient F and their applicability range. Instead of considering either of the fit directly, the analysis is simplified using two values of F at two ranges of distance from the PF based vaguely on the maximum ratio. The events in the database are grouped according to their magnitude: M_W 5 -6 plotted in red, M_W 6 -7 in green, and M_W 7 -8 in blue. The dashed lines show the validity ranges in which the various coefficients F listed in the table are valid; the subscript of the coefficient F indicates the side on hanging wall (HW) or on footwall (FW), and order of the coefficient counted from the PF (1 or 2). Only simple type of DR is considered (rank 2 DR).

II.2.2. Slip exceedance probability of distributed fault

In accordance with to the previous studies, the displacements of the distributed faults (*d*) are generally normalized by the maximum displacement of the principal fault (*MD*) or the average displacement of the principal fault (*AD*). The reason why normalized displacement is adopted is the same as described in Section II.1.2. The conditional probability of slip exceedance of distributed faults ($P[d > d_0 \mid r, m, d \neq 0]$ in Eq. (5)) can be obtained by numerically convolving the gamma distribution for *d/MD* (or *d/AD*) with a log-normal distribution for *MD* (or *AD)* in the same manner as was done for the principal fault.

Two kinds of information are inevitable to calculate the conditional probability of slip exceedance of distributed faults. One is a distance attenuation equation for the normalized distributed displacement (*d/MD* or *d/AD*), and the other is a probability distribution for the normalized distributed displacement (*d/MD* or *d/AD*) at each distance from the principal fault to the distributed fault.

(1) Attenuation relationship

Youngs et al. in 2003 [58] adopted an exponential function with regard to the distance *r* as follows:

$$\frac{d}{MD} = 0.35e^{-0.091r} \quad \text{for hanging wall} \tag{34}$$

$$\frac{d}{MD} = 0.16e^{-0.137r} \quad \text{for foot wall} \tag{35}$$

For Japanese faults, [29, 61] also used the following expressions are:

$$\frac{d}{MD} = 0.55e^{-0.17r} \text{ based on field data} \tag{36}$$

$$\frac{d}{AD} = 1.9e^{-0.17r} \text{ based on field data} \tag{37}$$

$$\frac{d}{AD} = 1.6e^{-0.20r} \text{ based on field data, experiment, and calculation} \tag{38}$$

where r is in kilometres.

For strike-slip faults, Petersen et al. in 2011 [27] derived the following power function:

$$\ln(d) = 1.4016m - 0.1671\ln(r) - 6.7991 \tag{39}$$

$$\ln\left(\frac{d}{AD}\right) = -0.1826\ln(r) - 1.5471 \tag{40}$$

where d is in centimetres and r is in metres. The standard deviations of Eqs (39) and (40) are 1.1193 and 1.1388 in ln unit, respectively. Figures 54, 55 and 56 depict the distributed fault displacements in [27, 29, 58], respectively. A comparison between [58] and [29] for *d/MD* was made in Figure 57, and a comparison between [27] and [173] for *d/AD* was shown in Figure 58. Additionally, graphs based on [27] were plotted in the particular case that the distance is less than 3 km in accordance with the paper.

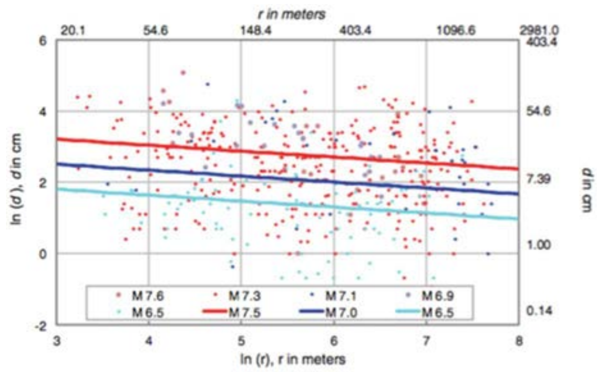

(a)

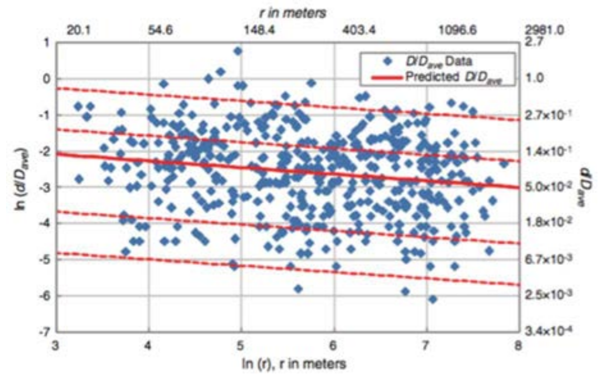

(b)

FIG 54. Distributed-fault displacement data and regression displacement color-coded magnitude with (a) bilinear line regression lines for Mw 6.5 to 7.5 with uncertainties (±1 and ±2 standard deviations, Eq. (39)) and (b) Normalized displacement with bilinear regression (Eq. (40)) (from [27] whit permission).

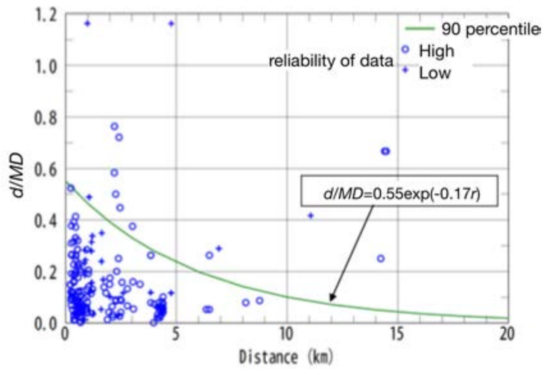

(a)

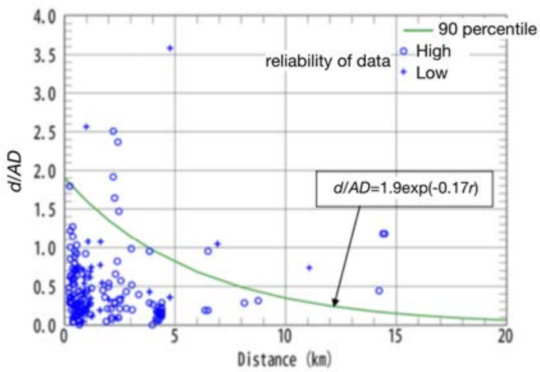

(b)

FIG 55. Data for displacements of distributed ruptures normalized by (a) the maximum displacement on the principal rupture, and (b) the average displacement of the principal rupture. The curves represent a high percentile (e.g. 90%) (from [29] reproduced with permission).

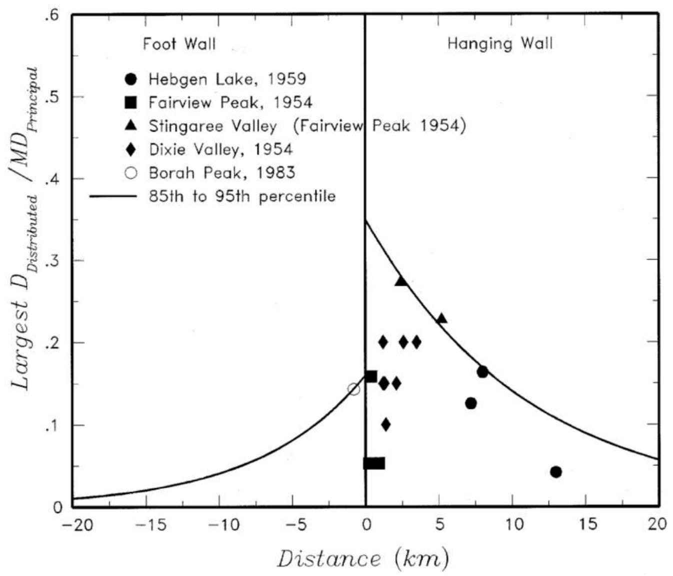

FIG 56. Data for larger displacements on distributed ruptures divided by the maximum displacement on the principal rupture. The curves represent a high percentile (e.g., 85th to 95th) of the distribution for D/MD. The data were compiled by C. dePolo for the Yucca Mountain PSHA (from [58] whit permission).

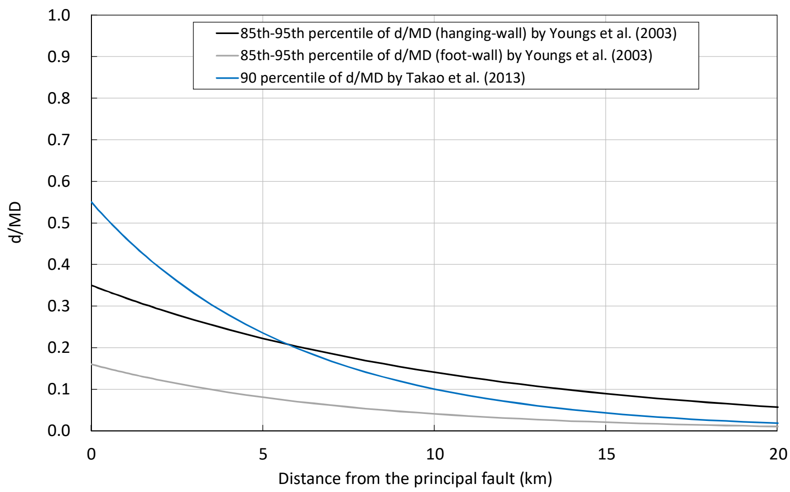

FIG 57. Distance attenuation of d/MD.

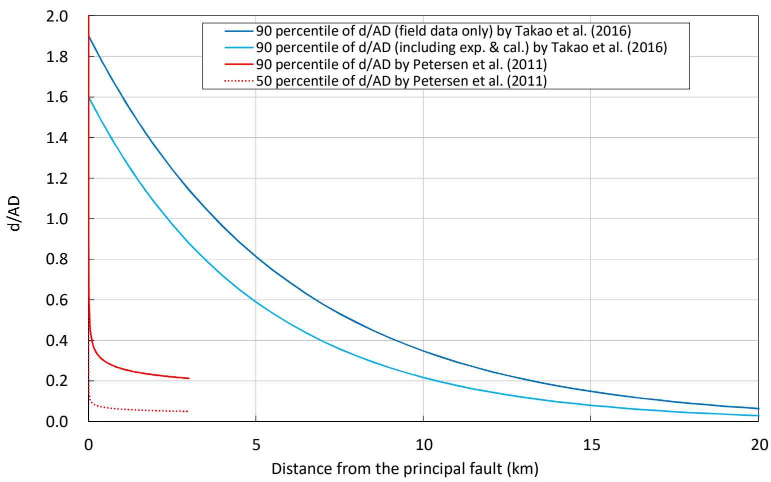

FIG 58. Distance attenuation of d/AD.

Nurminen et al. in 2020 [59] analysed the correlation between the displacement on the distributed rupture and the distance from the primary fault, the moment magnitude, and the displacement on the primary fault. The authors introduced a distance parameter, *s*, which indicates the distance between a point on the distributed rupture, with a measured vertical surface displacement, and the primary fault trace. Because to normalize to the maximum displacement does not consider the variability of the slip along the principal fault, which can be remarkable, especially in large events with long surface rupture length, the authors correlated the distributed displacement to the estimated local displacement along the principal fault. The authors introduced the parameter D_N that represents the estimated vertical slip along the principal fault strike. It is calculated for each displacement point along the distributed ruptures from the two nearest displacement values on principal fault, inversely weighted by their distance to the point on distributed rupture (Figure 59). To evaluate the expected mean value of vertical displacement (v_d) for distributed ruptures, Nurminen et al. in 2020 [59] performed a regression analysis on v_d and D_N, magnitude and distance *s* from the primary fault. The regression analysis is limited into a subset of the data within the distance in which the empirical database in use is seen the most complete, but the results are extrapolated also to further distances. The formula used for the regression calculation is:

$$\ln(Y) = a + b_1 \ln(s) + c_1 Ln\left(D_N\right) + d_1\left(m\right) \tag{41}$$

where *Y* is the median expectation of v_d, *s* is the distance parameter, D_N is the estimated displacement along the principal fault, *m is* the moment magnitude and the coefficients *a*, b_1, c_1 and d_1 are, respectively, -5.1043, -0.6483, 0.1983, and 0.9461 for footwall, and -4.2549, -0.1514, 0.4404, and 0.5711 for hanging wall.

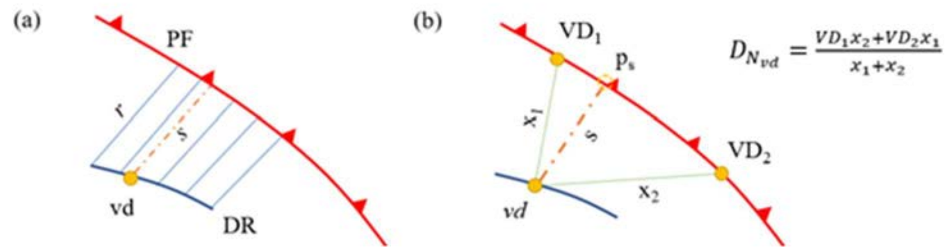

FIG 59. Measurements obtained from the georeferenced maps and displacement data of each earthquake in the dataset distinguishing the principal fault (PF; red line) and distributed ruptures (DR; thick blue line). (a) Definition of the distances 'r' and 's', and (b) Parameter DN estimating the slip along the PF near to the displacement vd, calculated considering the two nearest displacement points on PF (VD1 and VD2) and the corresponding distances, given more weight to the VD measured closer to the vd. ps indicates the other end of the segments.

(2) Probability distribution

Youngs et al. in 2003 [58] embraced the gamma distribution for *d/MD* and Takao et al. in 2013 [29] also adopted the same distribution for *d/MD* and *d/AD*. The form of the gamma distribution is expressed by Eq. (21), i.e., it has the same form as described in Section II.1.2 for the principal fault. Detailed information, such as shape parameter *a* and scale parameter *b* of the gamma distribution for the distributed fault, can be found in Table 14. In addition, Takao et al. in 2016 [173] revised the parameters

a and b for d/AD, which were proposed in [29], using the maximum likelihood method to improve the objectivity and reliability of the equation.

TABLE 14. COEFFICIENTS FOR EQ. (21) FOR DISTRIBUTED FAULT DISPLACEMENT.

Curve	*a*	*b*	Percentile	Reference
d/MD for hanging wall	2.5	0.35 exp (-0.091 r) / 5.535	95th	[58]
d/MD for footwall	2.5	0.16 exp (-0.137 r) / 5.535	95th	
d/MD for hanging wall	2.5	0.35 exp (-0.091 r) / 4.058	85th	
d/MD for footwall	2.5	0.16 exp (-0.137 r) / 4.058	85th	
d/MD	2.5	0.55 exp (-0.17 r) / 4.617	90th	[29]
d/AD	2.5	1.9 exp (-0.17 r) / 4.617	90th	
d/AD	1.282	0.644 exp (-0.17 r)	90th	[61]

In contrast, Petersen et al. in 2011 [27] employed the log-normal distribution, the standard deviation of which is 1.1388 in ln unit, to express the uncertainty of d/AD since they used the power function for the distance attenuation equation as described above. In this case, when calculating the conditional probability of slip exceedance ($P[d > d_0 \mid r, m, d \neq 0]$ in Eq. (9)), a numerical convolution will not be needed. Accordingly, the median and variance of the convolved log-normal distribution can be obtained by the following equations:

$$\log(d) = \log(AD) + \log\left(\frac{d}{AD}\right) \tag{42}$$

$$\sigma_{\log(d)} = \sqrt{\sigma_{\log(AD)}^{2} + \sigma_{\log(d/AD)}^{2}} \tag{43}$$

where $\sigma_{log(d)}$ is a standard deviation of log(d), $\sigma_{log(AD)}$ is a standard deviation of log(AD) and $\sigma_{log(d/AD)}$ is a standard deviation of log(d/AD).

The relationships between the cumulative probability and d/MD corresponding to some kind of the distance from the principal fault on the basis of [58] and [29] are demonstrated in Figure 60. As shown in the figure, Youngs et al. in 2003 [58] distinguished the hanging wall from the footwall, but Takao et al. in 2013 [29] did not. The relationships between the cumulative probability and d/AD based on [27] and [173] are plotted in Figure 61.

Figure 62 illustrates, as an example, the probability of exceeding a vertical displacement at a site at 500 m distance from the principal fault following the approach proposed by Nurminen et al. in 2020 [59]. The probability is modelled using a 3-sigma truncated distribution for two scenarios of M_W 7 and 7.4 and with the maximum vertical throw expected, respectively, of 2.3 m and 3.85 m on the principal fault. The probability is computed, for each scenario, for the site located on the hanging wall and the foot wall.

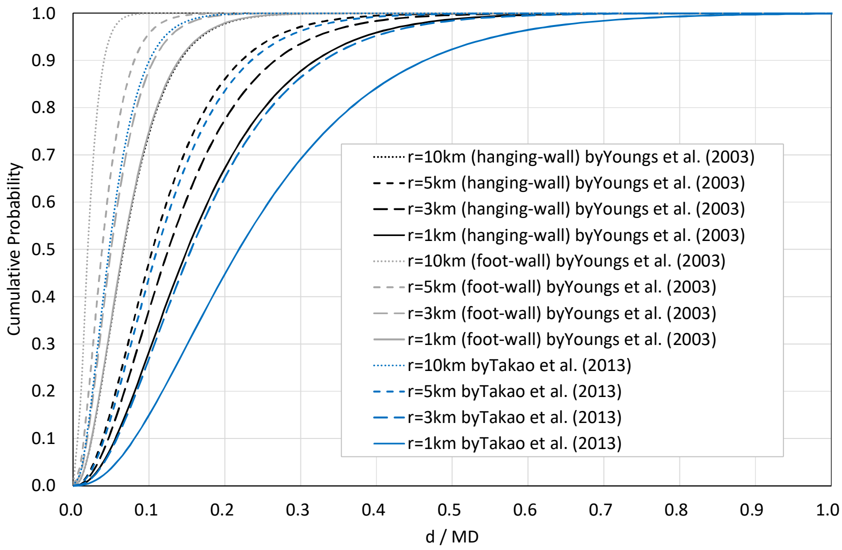

FIG 60. Cumulative probability of d/MD.

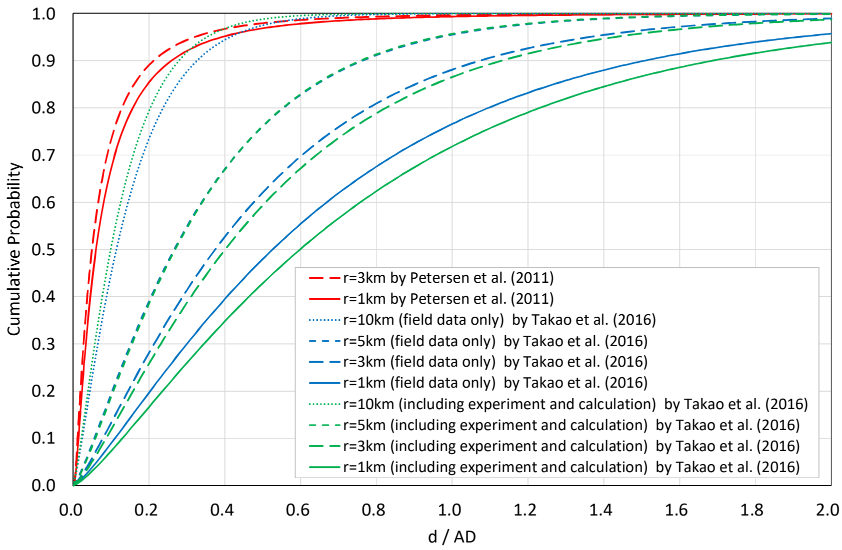

FIG 61. Cumulative probability of d/AD.

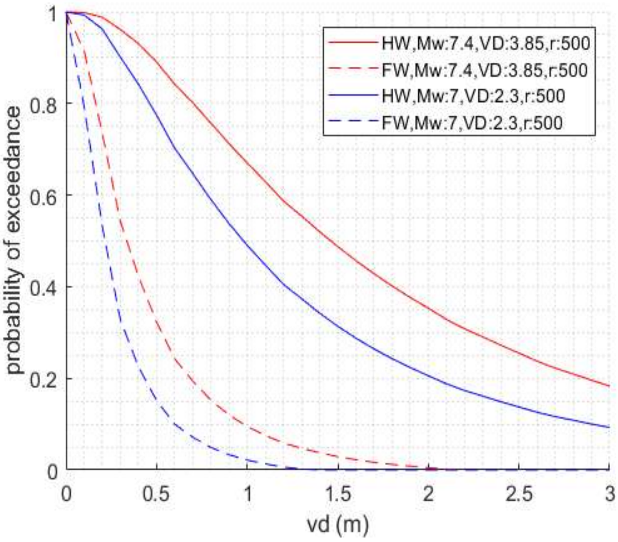

FIG 62. Curves for the probability of exceedance for given vertical displacement levels for hanging wall (HW; solid lines) and footwall (FW; dashed lines) for M_W 7 (blue lines) and M_W 7.4 (red lines) at a site in 500 m distance from the PF.

APPENDIX III. FUNDAMENTAL CONCEPTS FOR THE DYNAMIC RUPTURE APPROACH

III.1. VERIFICATION AND VALIDATION OF NUMERICAL METHODS

The verification of the software and validation of the numerical models need to be done before application in the PFDHA. The first step is the verification, which checks if the mathematical model used in a code conforms to the performed implementation. Thus, the verification checks the correctness of the implemented governing equations that are solving the imposed physics but does not confirm the validity of the mathematical model against natural earthquakes. It simply means that the implementation does not have any errors.

The mathematical model implemented in a simulation is subsequently used to build a model (or models) of natural earthquakes that use data from nature. This model, that highly depends on the input data, such as fault geometry, stress drop distribution, and geological structure, needs to pass a validation procedure. The validation of the earthquake model is the proof that the model solves the described problem with sufficient accuracy within its range of validity and considering the corresponding uncertainties. This means that the range of validity of the earthquake model is checked by comparing it against reality. Here, reality can be simulated by empirical data from observations of natural earthquakes. Figure 63 shows the overall principles of validation and verification.

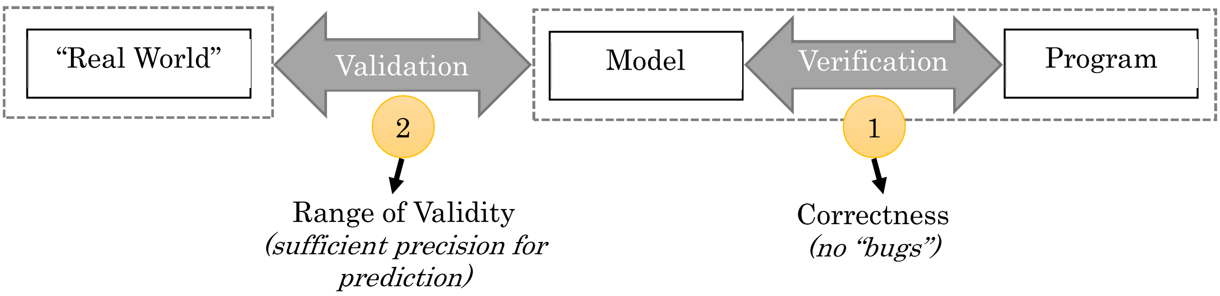

FIG 63. Principles of validation and verification.

III.1.1. Verification

The dynamic rupture models idealize natural earthquakes as a spontaneous propagation of shear cracks on a frictional interface. This idealization has proven to be a thorough foundation to evaluate natural earthquakes. But assessing the convergence and accuracy of the numerical methods that model these natural phenomena is challenging because there are no analytical solutions for this complex problem to compare [174]. An alternative solution to verify the numerical results of a given method is to assess comparisons with other independent numerical methods. The Southern California Earthquake Center/United State Geological Survey (SCEC/USGS) Spontaneous Rupture Code Verification Project [175, 176] has identified a series of benchmark problems, in which different numerical techniques compare results to verify if the methods are producing similar results when using the same model parameterization. Therefore, the numerical methods (software) planned to be used for PFDHA need to be verified in such a comparable framework.

III.1.2. Validation

The numerical models of natural earthquakes implemented in a given numerical technique (software) need to be validated with observed earthquakes. This process of validation is even more challenging than the verification procedure, as natural earthquakes are very complex and the inputs to the numerical model, such as from source and geological structures are full of uncertainties. Dynamic rupture model validations with empirical models have been developed in [136] and [137]. The SCEC Broadband Platform Project in 2015 [177] has also established a procedure to validate kinematic numerical models for ground motion prediction with empirical models and past earthquakes. In a similar way, synthetic fault displacement resulted from the numerical models can be compared with observed ones from real earthquakes. The main goal of this procedure is to check the plausibility of the results from numerical solutions by comparing the mean fault displacement with the observed earthquakes and empirical models.

III.2. DYNAMIC RUPTURE MODELS FOR PRINCIPAL FAULT

The main ingredient of the dynamic rupture models is the frictional constitutive law. There are essentially two types of friction laws used for dynamic rupture simulation: (1) the rate- and state-dependent friction and (2) slip-weakening friction models, both based on laboratory experiments. In Appendix IV.1, a brief description of these two types of friction laws is presented. Besides the site-specific data of the geological structure, the fault geometry and the stress field that are of relevant importance for a realistic earthquake simulation, the key element of the dynamic rupture models is the dynamic frictional parameterization and its distribution on the fault. The parameterization of the friction models is essentially defined by two parameters, the stress drop, and the fracture energy. For simplicity, Figure 64 shows the definition of these two parameters for the slip weakening friction model in the form given in [178]. The mean and the variability of these two parameters can be independently obtained from seismological observations (scaling laws from [179, 180]) and used for the dynamic rupture parameterization.

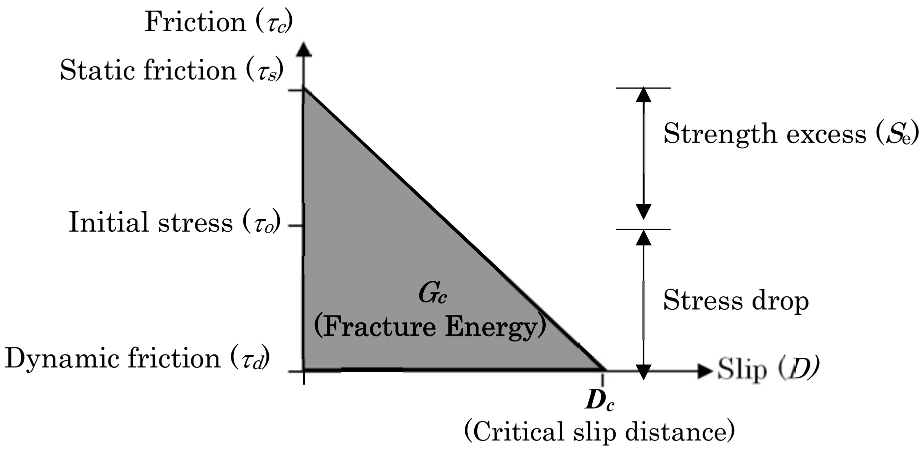

FIG 64. Slip weakening friction model in the form given by [178].

III.2.1. Stress drop distribution on fault

Since the purpose of the modelling is to evaluate potential future earthquakes, it is appropriate to use statistical properties of past earthquakes to constraint the stress drop distribution. Two approaches can be used, stochastic stress drop distribution and/or asperity models. For both cases, the fault dimensions (rupture area) are derived from empirical scaling relationship compatible to the area of study or from geological observation on the site of study.

Inversion of near-source ground motion [181] has revealed that slip distributions at seismogenic depths of past earthquakes are highly heterogeneous and follow some statistical distributions [182, 183]. These statistical distributions can then be used as constraints to generate a set of stochastic stress drop distribution models compatible to past earthquakes in a statistical sense [136, 137, 184, 185]. A brief description of the generation of stochastic slip distribution models can be found in Appendix IV.2.

Kinematic finite-fault rupture models characterized with asperity patches for strong ground motion prediction of scenario earthquakes is becoming the current practice and widely used in Japan for earthquake disaster mitigation of critical facilities [75, 186]. These models are constrained with the statistical properties of slip models from past earthquakes derived from source inversions [182]. In the same way, these asperity models have been also used to parameterize stress drop for fully physics-based dynamic rupture models [123, 133]. The stress drop distribution on the fault is therefore constrained with statistical characteristics of past earthquakes. A brief explanation of steps for stress drop parameterization of asperity models is presented in Appendix IV.3.

III.2.2. Fracture energy

The concept of fracture energy (G_c) is illustrated on Figure 64. G_c is a mesoscopic parameter, which contains all the dissipative processes in the volume around the rupture front (crack tip), such as off-fault yielding, damage, and micro-cracking. All these processes are mapped on the fault plane. Theoretical and empirical studies of fracture energy [180, 187–189] suggest that fracture energy is scale-dependent, varying with the spatial scale of the earthquake. These studies suggest that a large earthquake consumes more fracture energy as the rupture expands and reaches the free-surface, compared with a confined rupture. These independent previous studies help to define the values of critical slip distance (D_c) and strength excess (S_e), also defined in Figure 64.

III.2.3. Shallow layer zone

The shallow layer is the part of the crust between the top of the seismogenic zone and the surface. The thickness of the shallow layer zone might depend on the seismotectonic setting and the fault mechanism (Figure 3.29 from [190]). The rupture in the shallow layer influences the fault displacement as shown in [133, 191]. These authors developed dynamic rupture simulations of past earthquakes and found that the shallow layer zone properties strongly affect the fault displacement distribution and the very near-source ground motion. The rupture in the shallow layer zone might operate in a distinctive manner from the rest of the fault, as shown by the absence of earthquake nucleation in the shallower layers of the crust. This is due to the formation of incompetent fault gouge, cracking [192, 193], presence of thick surface deposits of sediments, fissured rocks and other forms of brittle rock damage that have evolved over many earthquake cycles and might even have formed flower-like zone structures with significant shallow damage [121, 122, 194]. This damage zone can be accumulated during the lifetime of a fault, either as the result of dynamic stress change induced by rupture during an earthquake [121, 122] or from quasi-static deformation during the life of a shear fault [195]. The main feature of this shallow layer zone is that during the rupture it operates with an enhanced energy absorption mechanism. This makes the frictional properties of the shallow layer zone distinct from those at deeper levels [196, 197].

For dynamic rupture simulation on the shallow layer zone, the frictional behaviour follows a mechanism of strength-hardening during frictional sliding that results in a negative stress drop. When using rate and state friction models, this zone can be evaluated following the velocity strengthening parameterization. If slip-weakening friction model is assumed, the mechanism of fault-strength hardening can be achieved, imposing negative stress drop in the friction parameterization [123, 133, 184].

The shallow layer zone plays an important role in the prediction of the fault displacement; therefore, it is relevant to introduce a detailed characterization of this zone for PFDHA based on physics-based rupture models.

APPENDIX IV. DETAILED INFORMATION FOR FRICTION LAWS, SLIP DISTRIBUTION AND STRESS DROP PARAMETERIZATIONS

IV.1. FRICTION LAWS FOR DYNAMIC RUPTURE MODELS

In general, the friction (frictional strength) τ_c is assumed to be proportional to normal stress σ_n. This can be expressed as follows:

$$\tau_c = \mu_f \sigma_n \tag{44}$$

where μ_f is the friction coefficient that can depend on slip, slip rate and other state variables. When the friction coefficient depends only on slip, Eq. (44) is named 'slip weakening friction law'. When the friction coefficient depends on slip rate and state variables, Eq. (44) is named 'rate and state friction law'. In the following, both friction models are briefly described.

IV.1.1. Slip weakening friction law

The slip-weakening model was first introduced in [198] and [199] by analogy to cohesive zone models of tensile fracture. Andrews in 1976 [178] used Ida's description of cohesive force and proposed a model in the form given in Figure 64. That is the linear slip-weakening form. Subsequently, this friction model was supported by laboratory experiments [200]. The slip weakening model is a simplified model widely used in seismology. Following the linear slip-weakening model in the form given in [178], the friction coefficient of Eq. (44) can be expressed as follows:

$$\mu_f = \begin{cases} \mu_s - (\mu_s - \mu_d)\dfrac{U}{D_c}, & U < D_C \\ \mu_{d,} & U \geq D_C \end{cases} \tag{45}$$

where μ_s and μ_d are coefficients of static and dynamic friction, respectively, U is slip and D_c is the critical slip-weakening distance. Following Eqs (44) and (45) and the definitions of frictional strengths shown in Figure 64, the static friction $\tau_s = \mu_s\sigma_n$ and the dynamic friction $\tau_d = \mu_d\sigma_d$. This model is extensively used for dynamic rupture simulation of earthquakes.

IV.1.2. Rate and state friction law

Dieterich in 1978 and 1979 [201, 202] proposed models of rate- and state-dependent friction to explain laboratory observations at relative low sliding of a variety of sliding phenomena of stick slip along simulated fault surfaces. These observations were fit by an empirical constitutive law in [202] and subsequently put into a rate- and state-dependent friction formulation in [203]. Several variations of rate- and state-dependent friction laws have been proposed [192]. The one presently in best agreement with experimental observations, called the Dieterich-Ruina, or 'slowness' law, states that friction depends both on the instantaneous sliding velocity (or slip rate) V and a time-dependent state variable θ:

$$\mu_f = \mu_0 + a\ln\left(\frac{V}{V_0}\right) + b\ln\left(\frac{V_0\theta}{L}\right) \tag{46}$$

in which the state variable θ evolves in accordance with Eq. (47):

$$\dot{\theta} = 1 - \left(\frac{V\theta}{L}\right) \tag{47}$$

where $\dot{\theta}$ is the derivative of θ with respect of time, L is the sliding distance for the evolution of θ (e.g., 10 mm for bare rock surfaces in the laboratory and up to 100 mm for gouge), and μ_0 and V_o are reference values at steady state of friction and velocity. The magnitude of the 'direct effect', i.e., the increase in strength with increasing slip velocity, is characterized by the parameter a. Instead, the magnitude of the 'evolution effect', i.e., the increase in strength with increasing total area and/or cohesiveness of points of contact, is characterized by the parameter b. Both a and b are positive and of order 10^{-2}. When $a - b < 0$, instable sliding due to velocity weakening occurs; this is the regime under which the earthquake can nucleate. When $a - b > 0$, stable sliding due to velocity strengthening occurs.

The rate and state friction model represented in Eq. (46) is known as the aging law model that can control the initiation, propagation, and healing process of the rupture, intrinsically exhibit strength restoration mechanism during quasi-static and quasi-dynamic slip (slow slip), strength weakening during dynamic instability (fast slip) and post-seismic slip (slow slip). It is a powerful and widely used model to study earthquake phenomena, that can simulate the entire process of an earthquake cycle that involve co-seismic and aseismic slip [204]. There are other rate and state friction models, such the so-called 'slip law' and 'slip law with strong velocity weakening' derived from high speed friction experiments that can be also used for dynamic rupture simulation [141, 205].

IV.2. SLIP DISTRIBUTION MODELS

The use of slip distribution models in PSHA have been pioneered by the Southern California Earthquake Center through the Cybershake Project [206] and have the potential to be applicable to PFDHA as well.

Slip distributions can be obtained using two approaches: kinematic and dynamic. In the kinematic approach, similar to the kinematic ground motion studies, the slip distributions are obtained guided from source inversions (slip images) of past earthquakes, without necessarily understanding the physics behind the rupture process. Dynamic approaches are true physics-based models, where the slip on the fault evolves from a set of initial stress conditions using constitutive relations. For simplicity, here, we focus primarily on the kinematic slip models for slip characterization that has its basis on slip images of past earthquakes. Slip models based on dynamic approach is discussed in Section 3.3.4.

Advanced numerical approaches for ground motion simulation use stochastic slip distribution models [207] constrained with statistical distributions of slip images from past earthquakes. These slip models use a spatial Fourier analysis approach, where the wavenumber spectra in the strike and dip direction follow a prescribed shape, such as a 2-D Butterworth filter [182] or a Von Karman correlation function [183], both with a $1/k^2$ drop-off. By randomizing the phase, a stochastic set of rupture models can be computed (Figure 65).

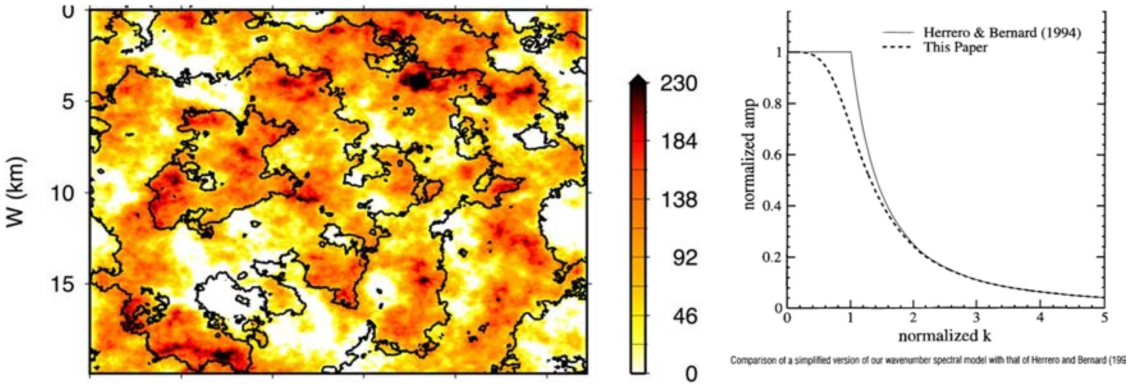

FIG 65. Example of a stochastic source model (left) generated using a $1/k^2$ wavenumber spectrum. On the right, examples of some simple spectral decay (whit permission from [182]).

An alternative method to the Fourier transform is the Karhunen-Loeve transformation [208], which is more versatile in allowing irregular fault geometries, and has been used for the modelling of tsunami sources. It holds a great promise for PFDHA because of its versatility and convenience for complex rupture planes, but currently no regressions of the actual slip models using this transformation have been carried out.

It needs to be noted that there is a fundamental difference between the source characterizations for ground motions and fault slip; the ground motions are very sensitive to rupture dynamics which might not necessarily correlate with the actual slip distribution. An example is the relationship between the slip and ground motions for the 2011 Tohoku earthquake. In this event, the largest slip was at the shallow zone, and the dominant seismic strong ground motions emanated from depth, a part of the fault hundreds of kilometres away from the largest area of slip.

The shallow slip distribution is obviously of most interest to PFDHA but is often poorly constrained by seismic inversions which tend to focus on the high-frequency radiation from deeper parts of the fault zone. Near-field geodetic data, such as Global Navigation Satellite System (GNSS) and InSAR data, provide much better constraints for the slip on the fault. Therefore, when carrying out the regressions to determine the wavenumber spectra to be used in numerical PFDHA, it is important to consider the data that was used to constrain the slip distributions.

IV.3. A PROCEDURE FOR STRESS DROP PARAMETERIZATION OF ASPERITIES

For stress drop parameterization of asperities, the following procedure is recommended:

(1) Define the rupture area following empirical relationship or from geological observation on the site of study.

(2) Define the asperity area. Use the characteristic slip models proposed in [182]. These authors analysed kinematic images from source inversions of past earthquakes and proposed two main statistical properties: 1) the average of combined asperity area is 0.22 times the total rupture area; and 2) the average slip on the combined asperities is 2 times the average slip over all the faults.

(3) Define the stress drop ratio between the average stress drop on asperity and background stress drop. Dalguer et al. in 2008 [123] estimated these ratios, calibrating asperity dynamic

rupture models that are statistically compatible with the kinematic slip models of past earthquakes characterized in [182].

(4) Constraint the average stress drop consistent with past earthquakes [123, 180].

(5) Develop a set of asperity models with the properties mentioned in (1) to (4).

REFERENCES

[1] INTERNATIONAL ATOMIC ENERGY AGENCY, Site Evaluation for Nuclear Installations, IAEA Safety Standards Series No. SSR-1, IAEA, Vienna (2019).

[2] INTERNATIONAL ATOMIC ENERGY AGENCY, Seismic Hazards in Site Evaluation for Nuclear Installations, IAEA Safety Standards Series No. SSG-9, IAEA, Vienna (2010).

[3] INTERNATIONAL ATOMIC ENERGY AGENCY, Evaluation of Seismic Safety for Existing Nuclear Installations, IAEA Safety Standards Series NS-G-2.13, IAEA, Vienna (2009).

[4] GUERRIERI, L., MICHETTI, A.M., SILVA, P.G., "EEE Catalogue: A Global Database of Earthquake Environmental Effects", Encyclopedia of Earthquake Engineering (BEER, M., KOUGIOUMTZOGLOU, I.A., PATELLI, E., AU, S.-K., Eds), Springer, Berlin, Heidelberg (2015) 932–944.

[5] WELLS, D.L., COPPERSMITH, K.J., New empirical relationships among magnitude, rupture length, rupture width, rupture area, and surface displacement, Bull. Seismol. Soc. Am. **84** 4 (1994) 974–1002.

[6] BIASI, G.P., WESNOUSKY, S.G., Bends and Ends of Surface Ruptures, Bull. Seismol. Soc. Am. **107** 6 (2017) 2543–2560.

[7] BIASI, G.P., WESNOUSKY, S.G., Steps and Gaps in Ground Ruptures: Empirical Bounds on Rupture Propagation, Bull. Seismol. Soc. Am. **106** 3 (2016) 1110–1124.

[8] MCCALPIN, J. (Ed), Paleoseismology, International geophysics series v. 95, 2nd ed., Academic Press, Burlington, MA (2009).

[9] STIRLING, M. et al., The Mw7.8 2016 Kaikoura earthquake: surface fault rupture and seismic hazard context, Bull. N. Z. Soc. Earthq. Eng. **50** 2 (2017) 73–84.

[10] ROCKWELL, T.K. et al., Reassessment of the 1892 Laguna Salada Earthquake: Fault Kinematics and Rupture Patterns, Bull. Seismol. Soc. Am. **105** 6 (2015) 2885–2893.

[11] CINTI, F.R. et al., Evidence for surface faulting events along the Paganica fault prior to the 6 April 2009 L'Aquila earthquake (central Italy), J. Geophys. Res. **116** B07308 (2011).

[12] GALADINI, F., GALLI, P., Paleoseismology of silent faults in the Central Apennines (Italy): the Mt. Vettore and Laga Mts. Faults, Ann Geophys **46** 5 (2003) 815.

[13] MARUYAMA, T. et al., Paleoseismological evidence for non-characteristic behavior of surface rupture associated with the 2004 Mid-Niigata Prefecture earthquake, central Japan, Tectonophysics **429** 1–2 (2007) 45–60.

[14] NISHIMURA, T. et al., Episodic growth of fault-related fold in northern Japan observed by SAR interferometry, Geophys. Res. Lett. **35** 13 (2008) L13301.

[15] LE BÉON, M. et al., Shallow geological structures triggered during the Mw 6.4 Meinong earthquake, southwestern Taiwan, Terr. Atmos. Ocean. Sci. **28** 5 (2017) 663-681.

[16] HARRIS, R.A., Large earthquakes and creeping faults, Rev. Geophys. **55** 1 (2017) 169–198.

[17] CHAUSSARD, E. et al., Interseismic coupling and refined earthquake potential on the Hayward-Calaveras fault zone, J. Geophys. Res. Solid Earth **120** 12 (2015) 8570–8590.

[18] THOMAS, M.Y., AVOUAC, J.-P., CHAMPENOIS, J., LEE, J.-C., KUO, L.-C., Spatiotemporal evolution of seismic and aseismic slip on the Longitudinal Valley Fault, Taiwan, J. Geophys. Res. Solid Earth **119** 6 (2014) 5114–5139.

[19] BESANA, G.M., ANDO, M., The central Philippine Fault Zone: Location of great earthquakes, slow events and creep activity, Earth Planets Space **57** 10 (2005) 987–994.

[20] LIENKAEMPER, J.J., DELONG, S.B., DOMROSE, C.J., ROSA, C.M., Afterslip Behavior following the 2014 M 6.0 South Napa Earthquake with Implications for Afterslip Forecasting on Other Seismogenic Faults, Seismol. Res. Lett. **87** 3 (2016) 609–619.

[21] LITCHFIELD, N.J., VAN DISSEN, R.J., HORNBLOW, S., QUIGLEY, M.C., ARCHIBALD, G., Detailed Analysis of Greendale Fault Ground Surface Rupture Displacements and Geometries, GNS Science Report 2013/18, Earthquake Commission of the New Zealand Government, (https://www.eqc.govt.nz/research/research-papers/detailed-analysis-of-greendale-fault-ground-surface-rupture-displacements-and-geometries).

[22] KELSON, K.I., KANG, K.-H., PAGE, W.D., LEE, C.-T., CLUFF, L.S., Representative Styles of Deformation along the Chelungpu Fault from the 1999 Chi-Chi (Taiwan) Earthquake: Geomorphic Characteristics and Responses of Man-Made Structures, Bull. Seismol. Soc. Am. **91** 5 (2001) 930–952.

[23] FLETCHER, J.M. et al., Assembly of a large earthquake from a complex fault system: Surface rupture kinematics of the 4 April 2010 El Mayor–Cucapah (Mexico) Mw 7.2 earthquake, Geosphere **10** 4 (2014) 797–827.

[24] CHIARALUCE, L. et al., The 2016 Central Italy Seismic Sequence: A First Look at the Mainshocks, Aftershocks, and Source Models, Seismol. Res. Lett. **88** 3 (2017) 757–771.

[25] CIVICO, R. et al., Surface ruptures following the 30 October 2016 Mw 6.5 Norcia earthquake, central Italy, J. Maps **14** 2 (2018) 151–160.

[26] RYMER, M.J. et al., Triggered Surface Slips in Southern California Associated with the 2010 El Mayor-Cucapah, Baja California, Mexico, Earthquake, USGS Numbered Series 2010–1333, Open-File Report, Vol. 2010–1333, U.S. Geological Survey, Reston, VA (2011).

[27] PETERSEN, M.D. et al., Fault Displacement Hazard for Strike-Slip Faults, Bull. Seismol. Soc. Am. **101** 2 (2011) 805–825. Electronic supplement available online (http://www.seismosoc.org/Publications/BSSA_html/bssa_101-2/2010035-esupp/index.html).

[28] WELLS, D., COPPERSMITH, K., Likelihood of surface rupture as a function of magnitude, Seismol. Res, Seismol. Res. Lett. **64** 1 (1993) 54.

[29] TAKAO, M., TSUCHIYAMA, J., ANNAKA, T., KURITA, T., Application of Probabilistic Fault Displacement Hazard Analysis in Japan, J. Jpn. Assoc. Earthq. Eng. **13** 1 (2013) 17–36.

[30] BONILLA, M.G., Minimum Earthquake Magnitude Associated with Coseismic Surface Faulting, Environ. Eng. Geosci. **xxv** 1 (1988) 17–29.

[31] CHAMPENOIS, J. et al., Evidences of Surface Rupture Associated With a Low-Magnitude (Mw5.0) Shallow Earthquake in the Ecuadorian Andes, J. Geophys. Res. Solid Earth **122** 10 (2017) 8446–8458.

[32] RITZ, J.-F. et al., Surface rupture and shallow fault reactivation during the 2019 Mw 4.9 Le Teil earthquake, France, Commun. Earth Environ. **1** 1 (2020) 1–11.

[33] MICHETTI, A.M. et al., Surface faulting and environmental effects accompanying the Dec. 26, 2018, Mw 4.9 Fleri earthquake, Mt. Etna volcano, Italy, INQUA Congr. 2019 (2019).

[34] CIVICO, R. et al., Surface ruptures following the 26 December 2018, Mw 4.9, Mt. Etna earthquake, Sicily (Italy), J. Maps **15** 2 (2019) 831–837.

[35] PEZZOPANE, S.K., DAWSON, T.E., Fault Displacement Hazard: A Summary of Issues and Information, in Seismotectonic Framework and Characterization of Faulting at Yucca Mountain, Nevada, U.S. Geological Survey Administrative Report prepared for the U.S. Department of Energy Chapter 9, (1996) page 160.

[36] MOSS, R.E.S., ROSS, Z.E., Probabilistic Fault Displacement Hazard Analysis for Reverse Faults, Bull. Seismol. Soc. Am. **101** 4 (2011) 1542–1553.

[37] BEANLAND, S., BERRYMAN, K.R., BLICK, G.H., Geological investigations of the 1987 Edgecumbe earthquake, New Zealand, N. Z. J. Geol. Geophys. **32** 1 (1989) 73–91.

[38] GRANDIN, R. et al., Rupture process of the Mw = 7.9 2015 Gorkha earthquake (Nepal): Insights into Himalayan megathrust segmentation, Geophys. Res. Lett. **42** 20 (2015) 8373–8382.

[39] CASKEY, S.J., WESNOUSKY, S.G., ZHANG, P., SLEMMONS, D.B., Surface faulting of the 1954 Fairview Peak (MS 7.2) and Dixie Valley (MS 6.8) earthquakes, central Nevada, Bull. Seismol. Soc. Am. **86** 3 (1996) 761–787.

[40] TERAN, O.J. et al., Geologic and structural controls on rupture zone fabric: A field-based study of the 2010 Mw 7.2 El Mayor–Cucapah earthquake surface rupture, Geosphere **11** 3 (2015) 899–920.

[41] MOSS, R.E.S., STANTON, K.V., BUELNA, M.I., The Impact of Material Stiffness on the Likelihood of Fault Rupture Propagating to the Ground Surface, Seismol. Res. Lett. **84** 3 (2013) 485–488.

[42] STANTON, K.V., Investigation of Parameters Influencing Reverse Fault Rupture Propagation to the Ground Surface, California Polytechnic State University, San Luis Obispo, Calif. (2013).

[43] THOMPSON, J. et al., Evidence of Previous Faulting along the 2019 Ridgecrest, California, Earthquake Ruptures, Bull. Seismol. Soc. Am. **110** 4 (2020) 1427–1456.

[44] SCHARER, K.M., SALISBURY, J.B., ARROWSMITH, J.R., ROCKWELL, T.K., Southern San Andreas Fault Evaluation Field Activity: Approaches to Measuring Small Geomorphic Offsets—Challenges and Recommendations for Active Fault Studies, Seismol. Res. Lett. **85** 1 (2014) 68–76.

[45] DUROSS, C.B. et al., Surface Displacement Distributions for the July 2019 Ridgecrest, California, Earthquake Ruptures, Bull. Seismol. Soc. Am. **110** 4 (2020) 1400–1418.

[46] PHILIP, H., MEGHRAOUI, M., Structural analysis and interpretation of the surface deformations of the El Asnam Earthquake of October 10, 1980, Tectonics **2** 1 (1983) 17–49.

[47] MASSONNET, D. et al., The displacement field of the Landers earthquake mapped by radar interferometry, Nature **364** (1993) 138–142.

[48] GOLD, P.O. et al., Coseismic slip variation assessed from terrestrial lidar scans of the El Mayor–Cucapah surface rupture, Earth Planet. Sci. Lett. **366** (2013) 151–162.

[49] SALISBURY, J.B. et al., Validation of meter-scale surface faulting offset measurements from high-resolution topographic data, Geosphere **11** 6 (2015) 1884–1901.

[50] DELONG, S.B. et al., Tearing the terroir: Details and implications of surface rupture and deformation from the 24 August 2014 M6.0 South Napa earthquake, California, Earth Space Sci. **3** 10 (2016) 416–430.

[51] VALLAGE, A., KLINGER, Y., GRANDIN, R., BHAT, H.S., PIERROT-DESEILLIGNY, M., Inelastic surface deformation during the 2013 Mw 7.7 Balochistan, Pakistan, earthquake, Geology **43** 12 (2015) 1079–1082.

[52] FUJIWARA, S. et al., Small-displacement linear surface ruptures of the 2016 Kumamoto earthquake sequence detected by ALOS-2 SAR interferometry, Earth Planets Space **68** 160 (2016).

[53] MILLINER, C.W.D. et al., Quantifying near-field and off-fault deformation patterns of the 1992 Mw 7.3 Landers earthquake, Geochem. Geophys. Geosystems **16** 5 (2015) 1577–1598.

[54] NICOL, A., VAN DISSEN, R.J., STIRLING, M.W., GERSTENBERGER, M.C., Quantifying the Incompleteness of New Zealand's Prehistoric Earthquake Record, EQC project 14/668 Final Report, (2017) 25p.

[55] BIASI, G.P., WELDON, R.J., Estimating Surface Rupture Length and Magnitude of Paleoearthquakes from Point Measurements of Rupture Displacement, Bull. Seismol. Soc. Am. **96** 5 (2006) 1612–1623.

[56] LETTIS, W.R., WELLS, D.L., BALDWIN, J.N., Empirical observations regarding reverse earthquakes, blind thrust faults, and quaternary deformation: Are blind thrust faults truly blind?, Bull. Seismol. Soc. Am. **87** 5 (1997) 1171–1198.

[57] WESNOUSKY, S.G., Displacement and Geometrical Characteristics of Earthquake Surface Ruptures: Issues and Implications for Seismic-Hazard Analysis and the Process of Earthquake Rupture, Bull. Seismol. Soc. Am. **98** 4 (2008) 1609–1632.

[58] YOUNGS, R.R. et al., A Methodology for Probabilistic Fault Displacement Hazard Analysis (PFDHA), *Earthquake Spectra*, **19** 1 (2003) pages 191–219.

[59] NURMINEN, F. et al., Probability of Occurrence and Displacement Regression of Distributed Surface Rupturing for Reverse Earthquakes, Front. Earth Sci. **8** (2020)581605.

[60] BAIZE, S. et al., Towards A Unified And Worldwide Database Of Surface Ruptures (Sure) For Fault Displacement Hazard Analyses, 8th International INQUA Meeting on Paleoseismology, Active Tectonics and Archeoseismology (PATA) (2017) 34–37.

[61] TAKAO, M. et al., Reliability Improvement of Probabilistic Fault Displacement Hazard Analysis, J. Jpn. Assoc. Earthq. Eng. **14** 2 (2014) 2_16-2_36.

[62] BAIZE, S. et al., A Worldwide and Unified Database of Surface Ruptures (SURE) for Fault Displacement Hazard Analyses, Seismol. Res. Lett. **91** 1 (2020) 499–520.

[63] SARMIENTO, A. et al., A New Model Database for Next-Generation Fault Displacement Hazard Analysis, Seismological Society of America Annual Meeting, (2019) Poster.

[64] BRANDENBERG, S.J. et al., Next-Generation Liquefaction (NGL) Case History Database Structure, Geotechnical Earthquake Engineering and Soil Dynamics V: Liquefaction Triggering, Consequences and Mitigation, Proceedings of a Meeting Held in Austin, Texas, 10–13 June 2018, Geotechnical Special Publication Number 290 (2018) 426–433.

[65] ANDERSON, J.G., BRUNE, J.N., Probabilistic Seismic Hazard Analysis without the Ergodic Assumption, Seismol. Res. Lett. **70** 1 (1999) 19–28.

[66] ANGELL, M.M., HANSON, K., SWAN, F.H., YOUNGS, R., ABRAMSON, H., Probabilistic Fault Displacement Hazard Assessment For Flowlines and Export Pipelines, Mad Dog and Atlantis Field Developments, Deepwater Gulf of Mexico, Offshore Technology Conference (2003).

[67] HECKER, S., ABRAHAMSON, N.A., WOODDELL, K.E., Variability of Displacement at a Point: Implications for Earthquake‐Size Distribution and Rupture Hazard on Faults, Bull. Seismol. Soc. Am. **103** 2A (2013) 651–674.

[68] INTERNATIONAL ATOMIC ENERGY AGENCY, Diffuse Seismicity in Seismic Hazard Assessment for Site Evaluation of Nuclear Installations, Safety Reports Series No. 89, IAEA, Vienna (2016).

[69] UTSU, T., "International Handbook of Earthquake and Engineering Seismology", An Imprint of Elsevier Science (2002) 733–746.

[70] SCORDILIS, E.M., Empirical Global Relations Converting MS and mb to Moment Magnitude, J. Seismol. **10** (2006) 225–236.

[71] KISHIDA, T., DARRAGH, R.B., BOZORGNIA, Y., KUO, C.-H., SI, H., Homogeneous Estimation of Moment Magnitude for Small‐to‐Moderate Magnitude Earthquakes Located near the Border between Japan and Taiwan, Seismol. Res. Lett. **89** 3 (2018) 1093–1100.

[72] LEONARD, M., Earthquake Fault Scaling: Self-Consistent Relating of Rupture Length, Width, Average Displacement, and Moment Release, Bull. Seismol. Soc. Am. **100** 5A (2010) 1971–1988.

[73] U.S. GEOLOGICAL SURVEY, Earthquake Probabilities in the San Francisco Bay Region: 2002–2031, Open-File Report 03–214, (2003) page Appendix D.

[74] IRIKURA, K., MIYAKE, H., Prediction of Strong Ground Motions for Scenario Earthquakes, Chigaku Zasshi **110** 6 (2001) 849–875.

[75] IRIKURA, K., MIYAKE, H., Recipe for Predicting Strong Ground Motion from Crustal Earthquake Scenarios, Pure Appl. Geophys. **168** (2011) 85–104.

[76] SHAW, B.E., Constant Stress Drop from Small to Great Earthquakes in Magnitude-Area Scaling - Short Note, Bull. Seismol. Soc. Am. **99** 2A (2009) 871–875.

[77] LEONARD, M., Self ‐ Consistent Earthquake Fault ‐ Scaling Relations: Update and Extension to Stable Continental Strike ‐ Slip Faults, Bull. Seismol. Soc. Am. **104** 6 (2014) 2953–2965.

[78] HANKS, T.C., BAKUN, W.H., A Bilinear Source-Scaling Model for M-log A Observations of Continental Earthquakes, Bull. Seismol. Soc. Am. **92** 5 (2002) 1841–1846.

[79] MIYAKOSHI, K. et al., Scaling Relationships of Source Parameters of Inland Crustal Earthquakes in Tectonically Active Regions, Pure Appl. Geophys. **177** (2020) 1917–1929.

[80] LUO, Y., AMPUERO, J.-P., MIYAKOSHI, K., IRIKURA, K., Surface Rupture Effects on Earthquake Moment-Area Scaling Relations, Pure Appl. Geophys. **174** (2017) 3331–3342.

[81] STIRLING, M., GODED, T., BERRYMAN, K., LITCHFIELD, N., Selection of Earthquake Scaling Relationships for Seismic ‐ Hazard Analysis, Bull. Seismol. Soc. Am. **103** 6 (2013) 2993–3011.

[82] CORNELL, C.A., Engineering seismic risk analysis, Bull. Seismol. Soc. Am. **58** 5 (1968) 1583–1606.

[83] MATTHEWS, M.V., ELLSWORTH, W.L., REASENBERG, P.A., A Brownian Model for Recurrent Earthquakes, Bull. Seismol. Soc. Am. **92** 6 (2002) 2233–2250.

[84] FIELD, E.H. et al., Long ‐ Term Time ‐ Dependent Probabilities for the Third Uniform California Earthquake Rupture Forecast (UCERF3), Bull. Seismol. Soc. Am. **105** 2A (2015) 511–543.

[85] GUTENBERG, B., RICHTER, C.F., Frequency of earthquakes in California, Bull. Seismol. Soc. Am. **34** 4 (1944) 185–188.

[86] SCHWARTZ, D.P., COPPERSMITH, K.J., SWAN, F.H., SOMERVILLE, P., SAVAGE, W.U., Characteristic earthquakes on intraplate normal faults, Earthq. Notes **52** 1 (1981) 71.

[87] SCHWARTZ, D.P., COPPERSMITH, K.J., Fault behavior and characteristic earthquakes: Examples from the Wasatch and San Andreas Fault Zones, J. Geophys. Res. Solid Earth **89** B7 (1984) 5681–5698.

[88] WESNOUSKY, S.G., Earthquakes, quaternary faults, and seismic hazard in California, J. Geophys. Res. Solid Earth **91** B12 (1986) 12587–12631.

[89] PAGE, M., FELZER, K., Southern San Andreas Fault Seismicity is Consistent with the Gutenberg–Richter Magnitude–Frequency Distribution, Bull. Seismol. Soc. Am. **105** 4 (2015) 2070–2080.

[90] FIELD, E.H., JACKSON, D.D., DOLAN, J.F., A mutually consistent seismic-hazard source model for southern California, Bull. Seismol. Soc. Am. **89** 3 (1999) 559–578.

[91] WONG, I., OLIG, S.S., Seismic Hazards In The Basin And Range Province: Perspectives From Probabilistic Analyses, Proc. Vol. Basin Range Prov. Seism. Hazard Summit **98–2** (1998) 110–127.

[92] INTERNATIONAL ATOMIC ENERGY AGENCY, The Contribution of Palaeoseismology to Seismic Hazard Assessment in Site Evaluation for Nuclear Installations, IAEA- TECDOC-1767, IAEA, Vienna (2015).

[93] BONCIO, P., LIBERI, F., CALDARELLA, M., NURMINEN, F.-C., Width of surface rupture zone for thrust earthquakes: implications for earthquake fault zoning, Nat. Hazards Earth Syst. Sci. **18** **1** (2018) 241–256.

[94] AMERICAN NUCLEAR SOCIETY, Criteria for Assessing Tectonic Surface Fault Rupture and Deformation at Nuclear Facilities, ANS 2.30-2015, (2015).

[95] MILLINER, C.W.D., DOLAN, J.F., HOLLINGSWORTH, J., LEPRINCE, S., AYOUB, F., Comparison of coseismic near-field and off-fault surface deformation patterns of the 1992 Mw 7.3 Landers and 1999 Mw 7.1 Hector Mine earthquakes: Implications for controls on the distribution of surface strain, Geophys. Res. Lett. **43** 19 (2016) 10115-10124.

[96] ZINKE, R., HOLLINGSWORTH, J., DOLAN, J.F., DISSEN, R.V., Three-Dimensional Surface Deformation in the 2016 MW 7.8 Kaikōura, New Zealand, Earthquake From Optical Image Correlation: Implications for Strain Localization and Long-Term Evolution of the Pacific-Australian Plate Boundary, Geochem. Geophys. Geosystems **20** 3 (2019) 1609–1628.

[97] HEMPHILL-HALEY, M.A., WELDON, R.J., Estimating prehistoric earthquake magnitude from point measurements of surface rupture, Bull. Seismol. Soc. Am. **89** 5 (1999) 1264–1279.

[98] BIASI, G.P., WELDON, R.J., San Andreas Fault Rupture Scenarios from Multiple Paleoseismic Records: Stringing Pearls, Bull. Seismol. Soc. Am. **99** 2A (2009) 471–498.

[99] PETERSEN, M., CHEN, R., Fault Displacement Hazard for Strike-Slip Faults, Earthquake Engineering Research Institute, Los Angeles, CA (2018) 12.

[100] CHEN, R., PETERSEN, M.D., Probabilistic Fault Displacement Hazards for the Southern San Andreas Fault Using Scenarios and Empirical Slips, Earthq. Spectra **27** 2 (2011) 293–313.

[101] JONES, L. et al., The ShakeOut Scenario, USGS Open File Report 2008-1150, CGS Preliminary Report 25, U.S. Department of the Interior and U.S. Geological Survey (2008).

[102] CHEN, R., DAWSON, T., WILLS, C., Quantifying Surface Fault Rupture Location Uncertainty for Lifeline Crossings, Final Technical Report Award Number G11AP20040, U.S. Geological Survey National Earthquake Hazards Reduction Program, U.S. Geological Survey (2013).

[103] DAWSON, T.E., MCGILL, S.F., ROCKWELL, T.K., Irregular recurrence of paleoearthquakes along the central Garlock fault near El Paso Peaks, California, J. Geophys. Res. Solid Earth **108** B7 (2003) 2356.

[104] ROCKWELL, T., SEITZ, G., YOUNG, J., DAWSON, T., Late Holocene Earthquake History of the Anza Seismic Gap Central Jacinto Fault Zone, Southern California, USGS Final Technical Report, U.S. Geological Survey (2004).

[105] CLARK, K.J. et al., Highly variable coastal deformation in the 2016 MW7.8 Kaikōura earthquake reflects rupture complexity along a transpressional plate boundary, Earth Planet. Sci. Lett. **474** (2017) 334–344.

[106] TODA, S., KANEDA, H., OKADA, S., ISHIMURA, D., MILDON, Z.K., Slip-partitioned surface ruptures for the Mw 7.0 16 April 2016 Kumamoto, Japan, earthquake, Earth Planets Space **68** (2016) 188.

[107] TREIMAN, J.A., Primary Surface Rupture Associated with the Mw 7.1 16 October 1999 Hector Mine Earthquake, San Bernardino County, California, Bull. Seismol. Soc. Am. **92** 4 (2002) 1171–1191.

[108] HAEUSSLER, P.J. et al., Surface Rupture and Slip Distribution of the Denali and Totschunda Faults in the 3 November 2002 M 7.9 Earthquake, Alaska, Bull. Seismol. Soc. Am. **94** 6B (2004) S23–S52.

[109] YAMASHITA, T., UMEDA, Y., Earthquake rupture complexity due to dynamic nucleation and interaction of subsidiary faults, Pure Appl. Geophys. **143** (1994) 89–116.

[110] POLIAKOV, A.N.B., DMOWSKA, R., RICE, J.R., Dynamic shear rupture interactions with fault bends and off-axis secondary faulting, J. Geophys. Res. Solid Earth **107** B11 (2002) ESE 6-1-ESE 6-18.

[111] KAME, N., RICE, J.R., DMOWSKA, R., Effects of prestress state and rupture velocity on dynamic fault branching, J. Geophys. Res. Solid Earth **108** B5 (2003) ESE 13-1-ESE 13-21.

[112] AOCHI, H., SCOTTI, O., BERGE ‐ THIERRY, C., Dynamic transfer of rupture across differently oriented segments in a complex 3-D fault system, Geophys. Res. Lett. **32** 21 (2005) L21304.

[113] URATA, Y., HOK, S., FUKUYAMA, E., MADARIAGA, R., The effect of thermal pressurization on dynamic fault branching, Geophys. J. Int. **196** (2014) 1237–1246.

[114] AOCHI, H., CUSHING, M., SCOTTI, O., BERGE-THIERRY, C., Estimating rupture scenario likelihood based on dynamic rupture simulations: the example of the segmented Middle Durance fault, southeastern France, Geophys. J. Int. **165** 2 (2006) 436–446.

[115] ANDO, R., IMANISHI, K., PANAYOTOPOULOS, Y., KOBAYASHI, T., Dynamic rupture propagation on geometrically complex fault with along-strike variation of fault maturity: insights from the 2014 Northern Nagano earthquake, Earth Planets Space **69** (2017) 130.

[116] TREIMAN, J. et al., ShakeOut Scenario Appendix E: Fault Rupture Impacts at Areas of Lifeline Concentration, U.S. Geological Survey Open File Report 2008-1150 and California Geological Survey Preliminary Report 25E, (2008).

[117] LOUKIDIS, D., SALGADO, R., Bearing capacity of strip and circular footings in sand using finite elements, Comput. Geotech. **36** 5 (2009) 871–879.

[118] WALD, D.J., ALLEN, T.I., Topographic Slope as a Proxy for Seismic Site Conditions and Amplification, Bull. Seismol. Soc. Am. **97** 5 (2007) 1379–1395.

[119] MOSS, R., BUELNA, M., STANTON, K., Physical, Analytical, and Numerical Modeling of Reverse Fault Displacement through Near Surface Soils, Bull. Seismol. Soc. Am. **108** 6 (2018) 3149–3159.

[120] THIO, H.K., OETTLE, N.K., Probabilistic Fault Displacement and Ground Deformation Hazard, FINAL TECHNICAL REPORT AWARD NUMBER G15AP00028, (2018).

[121] DALGUER, L.A., IRIKURA, K., RIERA, J.D., Generation of New Cracks Accompanied by the Dynamic Shear Rupture Propagation of the 2000 Tottori (Japan) Earthquake, Bull. Seismol. Soc. Am. **93** 5 (2003) 2236–2252.

[122] DALGUER, L.A., IRIKURA, K., RIERA, J.D., Simulation of tensile crack generation by three-dimensional dynamic shear rupture propagation during an earthquake, J. Geophys. Res. Solid Earth **108** B3 (2003) 2144.

[123] DALGUER, L.A., MIYAKE, H., DAY, S.M., IRIKURA, K., Surface Rupturing and Buried Dynamic-Rupture Models Calibrated with Statistical Observations of Past Earthquakes, Bull. Seismol. Soc. Am. **98** 3 (2008) 1147–1161.

[124] ERICKSON, B.A., DUNHAM, E.M., An efficient numerical method for earthquake cycles in heterogeneous media: Alternating subbasin and surface-rupturing events on faults crossing a sedimentary basin, J. Geophys. Res. Solid Earth **119** 4 (2014) 3290–3316.

[125] OGLESBY, D.D., DAY, S.M., Fault Geometry and the Dynamics of the 1999 Chi-Chi (Taiwan) Earthquake, Bull. Seismol. Soc. Am. **91** 5 (2001) 1099–1111.

[126] LOZOS, J.C., A case for historic joint rupture of the San Andreas and San Jacinto faults, Sci. Adv. **2** 3 (2016) e1500621.

[127] WOLLHERR, S., GABRIEL, A.-A., MAI, P.M., Landers 1992 “Reloaded”: Integrative Dynamic Earthquake Rupture Modeling, J. Geophys. Res. Solid Earth **124** 7 (2019) 6666–6702.

[128] AOCHI, H., ULRICH, T., A Probable Earthquake Scenario near Istanbul Determined from Dynamic Simulations, Bull. Seismol. Soc. Am. **105** 3 (2015) 1468–1475.

[129] DURAND, V., HOK, S., BOISELET, A., BERNARD, P., SCOTTI, O., Dynamic rupture simulations on a fault network in the Corinth Rift, Geophys. J. Int. **208** 3 (2017) 1611–1622.

[130] KUEHN, N.M., ABRAHAMSON, N.A., WALLING, M.A., Incorporating Nonergodic Path Effects into the NGA‐West2 Ground‐Motion Prediction Equations, Bull. Seismol. Soc. Am. **109** 2 (2019) 575–585.

[131] ABRAHAMSON, N., WOODDELL, K.E., Probabilistic Hazard Incorporating 3-D Simulations into Nonergodic Ground-Motion Models, IAEA, In: Best Practices in Physics Based Fault Rupture Models for Seismic Hazard Assessment of Nuclear Installations: issues and challenges towards full Seismic Risk Analysis, Proceedings of the IAEA Workshop Held in Cadarache-Chateau, 14-16 May, France (2018).

[132] ABRAHAMSON, N., Current and Planned Uses of Finite-Fault Numerical Simulations for Seismic Hazard Studies at the Diablo Canyon Power Plant, In: Best Practices in Physics Based Fault Rupture Models for Seismic Hazard Assessment of Nuclear Installations, Proceedings of a Workshop Held in Vienna, 18–20 November 2015, IAEA-TECDOC-CD-1833, IAEA, Vienna (2018).

[133] DALGUER, L.A. et al., Development of Dynamic Asperity Models to Predict Surface Fault Displacement Caused by Earthquakes, Pure Appl. Geophys. **177** (2020) 1983–2006.

[134] DAY, S.M., Three-dimensional simulation of spontaneous rupture: The effect of nonuniform prestress, Bull. Seismol. Soc. Am. **72** 6A (1982) 1881–1902.

[135] OLSEN, K.B. et al., ShakeOut-D: Ground motion estimates using an ensemble of large earthquakes on the southern San Andreas fault with spontaneous rupture propagation, Geophys. Res. Lett. **36** 4 (2009) L04303.

[136] BAUMANN, C., DALGUER, L.A., Evaluating the Compatibility of Dynamic Rupture‐Based Synthetic Ground Motion with Empirical Ground‐Motion Prediction Equation, Bull. Seismol. Soc. Am. **104** 2 (2014) 634–652.

[137] ANDREWS, D.J., MA, S., Validating a Dynamic Earthquake Model to Produce Realistic Ground Motion, Bull. Seismol. Soc. Am. **106** 2 (2016) 665–672.

[138] ANDREWS, D.J., Rupture dynamics with energy loss outside the slip zone, J. Geophys. Res. Solid Earth **110** (2005) B01307.

[139] ANDO, R., YAMASHITA, T., Effects of mesoscopic-scale fault structure on dynamic earthquake ruptures: Dynamic formation of geometrical complexity of earthquake faults, J. Geophys. Res. Solid Earth **112** (2007) B09303.

[140] MA, S., ANDREWS, D.J., Inelastic off-fault response and three-dimensional dynamics of earthquake rupture on a strike-slip fault, J. Geophys. Res. Solid Earth **115** (2010) B04304.

[141] SHI, Z., DAY, S.M., Rupture dynamics and ground motion from 3-D rough-fault simulations, J. Geophys. Res. Solid Earth **118** 3 (2013) 1122–1141.

[142] ROTEN, D., OLSEN, K.B., DAY, S.M., CUI, Y., “Quantification of Fault-Zone Plasticity Effects with Spontaneous Rupture Simulations”, Best Practices in Physics-Based Fault Rupture Models for Seismic Hazard Assessment of Nuclear Installations, Pageoph Topical Volumes (DALGUER, L.A., FUKUSHIMA, Y., IRIKURA, K., WU, C., Eds), Springer International Publishing, Cham (2018) 45–67.

[143] UETA, K., TANI, K., Deformation of Quaternary Deposits and Ground Surface Caused by Bedrock Fault Movements (Part 2) -Normal and Reverse Fault Model Tests-, U98048, Central Research Institute of Electric Power Industry, Abiko (1999).

[144] BOMMER, J.J., SCHERBAUM, F., The Use and Misuse of Logic Trees in Probabilistic Seismic Hazard Analysis, Earthq. Spectra **24** 4 (2008) 997–1009.

[145] UNITED STATES NUCLEAR REGULATORY COMMISSION, Updated Implementation Guidelines for SSHAC Hazard Studies, NUREG-2213, USNRC (2018).

[146] THIO, H.K., SOMERVILLE, P., Report 6: Aliso Canyon Probabilistic Fault Displacement Hazard Analysis, Report to the Socal Gas Company, (2019) p. 38.

[147] INTERNATIONAL ATOMIC ENERGY AGENCY, Site and External Events Design (SEED) Guidelines for the Preparation and Conduct of SEED Missions, IAEA Services Series No. 42, IAEA, Vienna (2019).

[148] STEPP, J.C. et al., Probabilistic Seismic Hazard Analyses for Ground Motions and Fault Displacement at Yucca Mountain, Nevada, *Earthquake Spectra*, **17** 1 (2001) 113–151.

[149] BUDNITZ, R.J., APOSTOLAKIS, G., BOORE, D.M., Recommendations for Probabilistic Seismic Hazard Analysis: Guidance on Uncertainty and Use of Experts, NUREG/CR-6372-Vol.1; UCRL-ID-122160, Nuclear Regulatory Commission, Washington, DC (United States). Div. of Engineering Technology; Lawrence Livermore National Lab., CA (United States); Electric Power Research Inst., Palo Alto, CA (United States); USDOE, Washington, DC (United States) (1997).

[150] HARDEBECK, J.L., Seismotectonics and Fault Structure of the California Central Coast, Bull. Seismol. Soc. Am. **100** 3 (2010) 1031–1050.

[151] PACIFIC GAS AND ELECTRIC COMPANY, Report on the Analysis of the Shoreline Fault Zone, Central Coastal California, Nos. 50-275 and 50-323, ML 110140431 (2011).

[152] PACIFIC GAS AND ELECTRIC COMPANY, Calculation Number GEO.DCPP.10.01, Rev 0, Evaluation of Secondary Fault Rupture Hazard from the Shoreline Fault Zone, Nos. 50-275 and 50-323, PG&E Letter No. DCL-10-019, February 26, ML 100680564 (2010).

[153] UNITED STATES NUCLEAR REGULATORY COMMISSION, Confirmatory Analysis of Seismic Hazard at the Diablo Canyon Power Plant from the Shoreline Fault Zone, Research Information Letter (RIL) 12–01, September, ML 121230035 (2012).

[154] U.S. GEOLOGICAL SURVEY, The Uniform California Earthquake Rupture Forecast, Version 3 (UCERF3)—The Time-Independent Model, U.S. Geological Survey Open-File Report 2013-1165, USGS, Reston, Virginia (2013).

[155] HANSON, K.L., LETTIS, W.R., MCLAREN, M., SAVAGE, W.U., HALL, N.T., Style and Rate of Quaternary Deformation of the Hosgri Fault Zone, Offshore South-Central Coastal California, USGS Numbered Series 1995-BB, (2004).

[156] JOHNSON, S.Y., HARTWELL, S.R., DARTNELL, P., Offset of Latest Pleistocene Shoreface Reveals Slip Rate on the Hosgri Strike‐Slip Fault, Offshore Central California, Bull. Seismol. Soc. Am. **104** 4 (2014) 1650–1662.

[157] LETTIS, W.R. et al., “Quaternary deformation of the San Luis Range, San Luis Obispo County, California”, Geological Society of America Special Papers, Vol. 292, Geological Society of America (1994) 111–132.

[158] FIELD, E.H. et al., Uniform California Earthquake Rupture Forecast, Version 3 (UCERF3)—The Time‐Independent Model, Bull. Seismol. Soc. Am. **104** 3 (2014) 1122–1180.

[159] PACIFIC GAS AND ELECTRIC COMPANY, Seismic Source Characterization for the Diablo Canyon Power Plant, San Luis Obispo County, California (2015).

[160] MCLAREN, M.K., SAVAGE, W.U., Seismicity of South-Central Coastal California: October 1987 through January 1997, Bull. Seismol. Soc. Am. **91** 6 (2001) 1629–1658.

[161] MCLAREN, M.K. et al., Complex Faulting Associated with the 22 December 2003 Mw 6.5 San Simeon, California, Earthquake, Aftershocks, and Postseismic Surface Deformation, Bull. Seismol. Soc. Am. **98** (2008) 1659–1680.

[162] PACIFIC GAS AND ELECTRIC COMPANY, Final Report of the Diablo Canyon Long-Term Seismic Program, U.S. Nuclear Regulatory Commission Docket Nos. 50-275 and 50-323 (1988).

[163] PETERSEN, M.D. et al., Evaluating Fault Rupture Hazard for Strike-Slip Earthquakes, American Society of Civil Engineers, Los Angeles, California (2004) 787–796.

[164] YOUNGS, R.R., COPPERSMITH, K.J., Implications of fault slip rates and earthquake recurrence models to probabilistic seismic hazard estimates, Bull. Seismol. Soc. Am. **75** 4 (1985) 939–964.

[165] PAUL C. RIZZO ASSOCIATES, INC., Technical Report, Probabilistic Fault Displacement Hazard Analysis, Krško East and West Sites, Proposed Krško 2 Nuclear Power Plant, Krško, Slovenia Revision 1, Pittsburgh, Pennsylvania, USA (2013).

[166] PAUL C. RIZZO ASSOCIATES, INC., Final Technical Report, Sensitivity Analysis, Probabilistic Fault Displacement Hazard Analysis, Krško East and West Sites, Proposed Krško 2 Nuclear Power Plant, Krško, Slovenia, Revision 1, Pittsburgh, Pennsylvania, USA (2013).

[167] QUITTMEYER, R.C. et al., Probabilistic Fault Displacement Hazard Analysis for Regulatory Decision-Making: A Case-Study for Krško, Slovenia, American Nuclear Society, Pittsburgh, PA (2017) 182–191.

[168] BAZARGAN, S.B., BERNARDIE, S., Geotechnical, Geological, and Seismological (GG&S) Evaluations for the New Nuclear Power Plant at the Krško Site: Phase 1 Summary Report, BRGM/RC-59096-FR, 164p., (2010).

[169] SIROVICH, L., SUHADOLC, P., COSTA, G., PETTENATI, F., A review of the seismotectonics and some considerations on the seismic hazard of the Krško NPP area (SE Slovenia), Boll. Geofis. Teor. Ed Appl. **55** 1 (2014) 175–195.

[170] PUCCI, S. et al., Coseismic ruptures of the 24 August 2016, Mw 6.0 Amatrice earthquake (central Italy), Geophys. Res. Lett. **44** 5 (2017) 2138–2147.

[171] MCCALPIN, J.P., SLEMMONS, D.B., Statistics of Paleoseismic Data Program Element III: Understanding Earthquake Processes, Contract 1434-HQ-96-GR-02752, GEO-HAZ Consulting, Inc., Estes Park (1998).

[172] SUZUKI, Y., ANNAKA, T., Probabilistic Hazard Analysis for Secondary Fault; In: INTERNATIONAL ATOMIC ENERGY AGENCY, Best Practices in Physics Based Fault Rupture Models for Seismic Hazard Assessment of Nuclear Installations, Proceedings of a Workshop Held in Vienna, 18–20 November 2015, IAEA-TECDOC-CD-1833, IAEA, Vienna (2018).

[173] TAKAO, M., TANI, T., OSHIMA, T., ANNAKA, T., KURITA, T., Maximum Likelihood Estimation of the Parameters regarding Displacement Evaluation of Distributed Fault in PFDHA, J. Jpn. Assoc. Earthq. Eng. **16** 2 (2016) 2_96-2_101.

[174] DAY, S.M., DALGUER, L.A., LAPUSTA, N., LIU, Y., Comparison of finite difference and boundary integral solutions to three-dimensional spontaneous rupture, J. Geophys. Res. Solid Earth **110** (2005) B12307.

[175] HARRIS, R.A. et al., The SCEC/USGS Dynamic Earthquake Rupture Code Verification Exercise, Seismol. Res. Lett. **80** 1 (2009) 119–126.

[176] HARRIS, R.A. et al., A Suite of Exercises for Verifying Dynamic Earthquake Rupture Codes, Seismol. Res. Lett. **89** 3 (2018) 1146–1162.

[177] GOULET, C.A., ABRAHAMSON, N.A., SOMERVILLE, P.G., WOODDELL, K.E., The SCEC Broadband Platform Validation Exercise: Methodology for Code Validation in the Context of Seismic ‐ Hazard Analyses, Seismol. Res. Lett. **86** 1 (2015) 17–26.

[178] ANDREWS, D.J., Rupture velocity of plane strain shear cracks, J. Geophys. Res. **81** 32 (1976) 5679–5687.

[179] ABERCROMBIE, R.E., RICE, J.R., Can observations of earthquake scaling constrain slip weakening?, Geophys. J. Int. **162** 2 (2005) 406–424.

[180] CAUSSE, M., DALGUER, L.A., MAI, P.M., Variability of dynamic source parameters inferred from kinematic models of past earthquakes, Geophys. J. Int. **196** 3 (2014) 1754–1769.

[181] MAI, P.M., THINGBAIJAM, K.K.S., SRCMOD: An Online Database of Finite ‐ Fault Rupture Models, Seismol. Res. Lett. **85** 6 (2014) 1348–1357.

[182] SOMERVILLE, P. et al., Characterizing Crustal Earthquake Slip Models for the Prediction of Strong Ground Motion, Seismol. Res. Lett. **70** 1 (1999) 59–80.

[183] MAI, P.M., BEROZA, G.C., A spatial random field model to characterize complexity in earthquake slip, J. Geophys. Res. Solid Earth **107** B11 (2002) ESE 10-1-ESE 10-21.

[184] PITARKA, A., DALGUER, L.A., DAY, S.M., SOMERVILLE, P.G., DAN, K., Numerical Study of Ground-Motion Differences between Buried-Rupturing and Surface-Rupturing Earthquakes, Bull. Seismol. Soc. Am. **99** 3 (2009) 1521–1537.

[185] DALGUER, L.A., MAI, P.M., Near-Source Ground Motion Variability from M~6.5 Dynamic Rupture Simulations, Effects of Surface Geology on Seismic Motion, University of California Santa Barbara, CA, USA. (2011).

[186] KAMAE, K., IRIKURA, K., Source model of the 1995 Hyogo-Ken Nanbu earthquake and simulation of near-source ground motion, Bull. Seismol. Soc. Am. **88** 2 (1998) 400–412.

[187] IDE, S., TAKEO, M., Determination of constitutive relations of fault slip based on seismic wave analysis, J. Geophys. Res. Solid Earth **102** B12 (1997) 27379–27391.

[188] MAI, P.M. et al., On scaling of fracture energy and stress drop in dynamic rupture models: Consequences for near-source ground-motions, Wash. DC Am. Geophys. Union Geophys. Monogr. Ser. **170** (2006) 283–293.

[189] IDE, S., AOCHI, H., Historical seismicity and dynamic rupture process of the 2011 Tohoku-Oki earthquake, Tectonophysics **600** (2013) 1–13.

[190] SCHOLZ, C.H., The Mechanics of Earthquakes and Faulting, 2nd ed., Cambridge University Press, Cambridge (2002).

[191] DALGUER, L. et al., Asperity Models to Predict Surface Fault Displacement Caused By Earthquakes: The 2010 Mw 7.0 Darfield (New Zealand) Earthquake, In: Best Practices in Physics Based Fault Rupture Models for Seismic Hazard Assessment of Nuclear Installations: issues and challenges towards full Seismic Risk Analysis, Proceedings of the IAEA Workshop Held in Cadarache-Chateau, 14-16 May, France (2018).

[192] MARONE, C., Laboratory-Derived Friction Laws and Their Application to Seismic Faulting, Annu. Rev. Earth Planet. Sci. **26** 1 (1998) 643–696.

[193] MARONE, C., SCHOLZ, C.H., The depth of seismic faulting and the upper transition from stable to unstable slip regimes, Geophys. Res. Lett. **15** 6 (1988) 621–624.

[194] BEN-ZION, Y., PENG, Z., LEWIS, M., MCGUIRE, J., High-resolution Imaging of Fault Zone Structures with Seismic Fault Zone Waves, Sci. Drill. (2007) 78–79.

[195] VERMILYE, J.M., SCHOLZ, C.H., The process zone: A microstructural view of fault growth, J. Geophys. Res. Solid Earth **103** B6 (1998) 12223–12237.

[196] BRUNE, J.N., ANOOSHEHPOOR, A., A physical model of the effect of a shallow weak layer on strong ground motion for strike-slip ruptures, Bull. Seismol. Soc. Am. **88** 4 (1998) 1070–1078.

[197] DAY, S.M., ELY, G.P., Effect of a Shallow Weak Zone on Fault Rupture: Numerical Simulation of Scale-Model Experiments, Bull. Seismol. Soc. Am. **92** 8 (2002) 3022–3041.

[198] IDA, Y., Cohesive force across the tip of a longitudinal-shear crack and Griffith's specific surface energy, J. Geophys. Res.**77** 20 (1972) 3796–3805.

[199] PALMER, A.C., RICE, J.R., HILL, R., The growth of slip surfaces in the progressive failure of over-consolidated clay, Proc. R. Soc. Lond. Math. Phys. Sci. **332** 1591 (1973) 527–548.

[200] OHNAKA, M., KUWAHARA, Y., YAMAMOTO, K., Nucleation and Propagation Processes of Stick-Slip Failure and Normal Stress Dependence of the Physical Parameters of Dynamic Slip Failure, Nat. Disaster Sci. **9** 1 (1987) 1–21.

[201] DIETERICH, J.H., Preseismic fault slip and earthquake prediction, J. Geophys. Res. Solid Earth **83** B8 (1978) 3940–3948.

[202] DIETERICH, J.H., Modeling of rock friction: 1. Experimental results and constitutive equations, J. Geophys. Res. Solid Earth **84** B5 (1979) 2161–2168.

[203] RUINA, A., Slip instability and state variable friction laws, J. Geophys. Res. Solid Earth **88** B12 (1983) 10359–10370.

[204] LAPUSTA, N., RICE, J.R., BEN - ZION, Y., ZHENG, G., Elastodynamic analysis for slow tectonic loading with spontaneous rupture episodes on faults with rate- and state-dependent friction, J. Geophys. Res. Solid Earth **105** B10 (2000) 23765–23789.

[205] ROJAS, O., DUNHAM, E.M., DAY, S.M., DALGUER, L.A., CASTILLO, J.E., Finite difference modelling of rupture propagation with strong velocity-weakening friction, Geophys. J. Int. **179** 3 (2009) 1831–1858.

[206] GRAVES, R. et al., CyberShake: A Physics-Based Seismic Hazard Model for Southern California, Pure Appl. Geophys. **168** (2011) 367–381.

[207] GRAVES, R.W., PITARKA, A., Broadband Ground-Motion Simulation Using a Hybrid Approach, Bull. Seismol. Soc. Am. **100** 5A (2010) 2095–2123.

[208] LEVEQUE, R.J., WAAGAN, K., GONZÁLEZ, F.I., RIM, D., LIN, G., Generating Random Earthquake Events for Probabilistic Tsunami Hazard Assessment, Pure Appl. Geophys. **173** 12 (2016) 3671–3692.

GLOSSARY

(in this publication)

Alquist-Priolo earthquake fault zones

Regulatory zones around Holocene faults established in accordance with the Alquist-Priolo Earthquake Fault Zoning Act in California. The intent of the Act is to prohibit building structures for human occupancy across the trace of the faults, thus mitigating hazards associated with surface fault rupture.

Asperity

An area of relatively high shear strength on a fault surface that retards slip. Within the framework of finite fault rupture modelling, the asperity in the kinematic approach is defined as the patch of high slip, and in the dynamic approach as the patch of high stress drop.

Attenuation relationship

A relationship that models the decrease in primary and secondary fault displacement amplitude with increasing distance along the principal fault or from the principal fault, respectively.

Co-seismic deformation

Permanent changes of the ground surface due to fault displacement during an earthquake or larger scale and inelastic deformation (subsidence, uplift, tilting, folding).

Creeping fault

A fault whose displacement occurs gradually and aseismically. Such faults might still have the potential for generating moderate to large earthquakes due to creep only occurring in the shallow portion of the fault.

Deterministic fault displacement hazard analysis

Methodology that estimates the fault displacement hazard at a site assuming a specific earthquake scenario regardless of the frequency for which that earthquake might occur.

Deterministic seismic hazard analysis

Methodology that estimates ground motion hazard at a site assuming a specific earthquake scenario regardless of the frequency for which that earthquake might occur.

Ergodic

Describes a random process in which the distribution of a random variable in space is the same as the distribution of that same random process at a single point when sampled in time.

Fault scarp

A linear or gently curved morphologic slope formed by the displacement of the ground surface by a capable fault. The morphology of the scarp is different for normal, reverse and strike-slip faults; and it changes with time from a free face or steep slope to a graded slope (slope decrease) due to the acting erosive/sedimentary processes.

Fault segment

Part of a geological fault that is bound by either a lithological, structural, or geometrical discontinuity (e.g., fault bend, step over or branch) or a combination of these. These bounds can act as barriers or initiation points for earthquakes. The term 'segment' is thus often used by earthquake geologists as a fault portion that ruptured during a single earthquake (earthquake segment). A single fault segment can rupture alone (single segment earthquake rupture) or together with its neighbours (multiple segment earthquake rupture) during different earthquakes.

Fault/fault zone

A fracture in the crust along which two blocks can move with respect to one another. Faulting might occur along different planes (see Surface fault displacement) and includes both primary and secondary faulting. The fault zone is the area encompassing this faulting.

Fault type

Refers to the three general categories of faults based on their sense of movement: strike-slip, normal, and reverse/thrust. Displacement on a strike-slip fault occurs horizontally parallel to the strike of the fault. A normal fault has its hanging wall block downward relative to the footwall. A reverse fault has its hanging wall block move upward relative to the footwall block. Horizontal and vertical faulting components can be combined in similar proportions, then defining oblique faulting. Faulting mechanism can vary along a single earthquake rupture, for instance depending on the geometrical relationships between block motion and fault geometry (strike, dip).

Fractile hazard curve

A fractile is a point on the distribution such that the calculated hazard has a given probability of being less or equal that point. A 5% and 95% percentile hazard curve indicate that we have a 5% and 95% confidence, respectively, that the calculated hazard would be less than that given by the curve. Fractile hazard curves are often used to show the epistemic uncertainty for each measure of ground motion.

Fracture energy

At the scale of finite fault that produces earthquakes relevant to seismology, fracture energy is a mesoscopic parameter, which contains all the dissipative processes in the volume around the crack tip during rupture propagation, such as off-fault yielding, damage, cracking. All these processes are mapped on the fault plane for earthquake rupture modelling.

Friction law

A constitutive behaviour of rocks under interface sliding that govern shear stress on the fault during rupture propagation. There are two types of friction law usually used in seismology: rate and state-dependent friction and slip-weakening friction.

Ground motion prediction equation

A model that estimates ground motions in terms of a ground motion metric such as peak ground acceleration, peak ground velocity and spectral ordinates with magnitude, distance, site condition, and often other source, path, and site parameters.

Global Positioning System (GPS)

A system of positioning and navigation based on a US satellite constellation. The term Global Navigation Satellite System (GNSS) is now preferred to include the European (Galileo), Russian (GLONASS), Chinese (BeiDou), Japanese (QZSS) and Indian (IRNSS) navigation systems.

Ground crack and fissure (Co-seismic)

Co-seismic features such as fractures or cracks, or fissures when those are accompanied with opening, can be formed in the ground surface during an earthquake, which are not directly related to the surface rupture (marked by slip along a shearing plane) of a capable fault. Secondary earthquake effect considered in the Environmental Seismic Intensity (ESI 2007) scale. There is no distinguishable relative displacement (offset) across a crack or fissure.

Hanging wall/footwall

The block located above (hanging wall) or below (footwall) a dipping fault.

Hazard curve

A plot that shows the probability of exceedance of a specified seismic hazard parameter (e.g., ground motion or fault displacement).

Hypocenter

The point of the earth's crust where a rupture initiates, creating an earthquake.

Interferometric synthetic-aperture radar (InSAR)

A radar technique used in geodesy and remote sensing. The technique can be used to generate maps of surface deformation or digital elevation using the phase differences of waves returning to the satellite.

Light detection and ranging (LiDAR)
A remote sensing technology that measures distance by illuminating a target with a laser and analyzing the reflected light. Airborne LiDAR is a technology frequently used to make high resolution digital elevation models.

Mean hazard curve
Corresponds to the mean of the probability distribution of hazard curves.

Median hazard curve
Corresponds to a 50%, or the 50th fractile, hazard curve.

Paleoseismology
The study of evidence of past (typically prehistoric) earthquakes manifested as displacement on a *fault* or secondary effects such as ground deformation (i.e., liquefaction, tsunami, landslides) with geological techniques, providing data on the timing, location, and size of these earthquakes (modified from [2]).

Permanent ground deformation
Ground displacement resulting from soil liquefaction, sliding, and displacement on a fault, either expressed at the surface or at depth.

Physics-based numerical simulations
Earthquake simulations based on numerical models that incorporate the physics of wave propagation and frictional sliding on the fault. Basically, there are two type of models used in seismology: 1) the kinematic approach that incorporates only the physics of wave propagation, and 2) the dynamic model that incorporates both, the physics of wave propagation and frictional sliding on the fault. The main differences between these two models are that in the kinematic model, the earthquake source is defined by prescribing the fault slip function, while in the dynamic model, the physical basis involved in the fault rupture is considered in which the kinematic slip is determined dynamically as part of the solution of the problem.

Pleistocene
First geological epoch of the Quaternary period. It began at the end of the *Pliocene* (around 2.6 million years ago) and continues to the *Holocene* (until 11 700 years ago). Much of the Pleistocene is commonly characterized by alternating glacial and interglacial periods.

Probability of exceedance

The probability that a given level of seismic hazard, such as peak ground acceleration, will be exceeded at a specified site given a predefined exposure time.

Probabilistic fault displacement hazard analysis (PFDHA)

Methodology that estimates probabilistic fault displacement hazard as expressed in the form of a seismic hazard curve (see hazard curve). Two approaches are used in state-of-the-practice applications: the 'earthquake' approach and 'displacement' approach.

Probabilistic seismic hazard analysis (PSHA)

Methodology that estimates probabilistic ground motion hazard as expressed in the form of a seismic hazard curve (see hazard curve).

Quaternary

The current and most recent geological period that spans from about 2.6 million years before present and today. The Pleistocene and the Holocene geological epochs are included in the Quaternary.

Recurrence interval

The time period between earthquakes of a given magnitude, fault offset of a given amount, or deformation of a given measure.

Return period

The inverse of the annual frequency of exceedance.

Rupture area

Area of a fault-plane that ruptures during a single earthquake.

Rupture length

Length of a fault that ruptured during a single earthquake measured along fault strike.

Synthetic aperture radar (SAR)

A form of radar that can be used in remote sensing and mapping to create two and three-dimensional images of the earth.

Seismic source characteristics

The geometric and kinematic parameters that characterize a seismic source for PSHA, such as length, seismogenic thickness, dip angle, maximum magnitude, and earthquake time recurrence.

Seismic moment

A measure of the size of an earthquake which is a function of the area of the fault rupture, the average displacement over that area, and the shear modulus of the rock along the fault.

Seismotectonic

The study of the relationships between earthquakes and active/capable faults, including regionally significant geological structures generating earthquakes and the time/space variations in the processes or structures.

Shear-wave velocity

The velocity at which shear waves travel in a material. Shear waves are the most damaging type of seismic wave in an earthquake. Knowledge of its velocity is used in several seismological techniques.

Slip distribution

The pattern of slip that occurs along a fault during an earthquake. Slip distributions can be quite variable with strong patches on the fault called asperities.

Slip rate

A parameter that indicates the rate of activity along a fault. The slip rate is calculated by dividing the total fault displacement by the time period over which that displacement has occurred.

Stress drop

The reduction in shear stress before and after an earthquake.

Surface Fault displacement

The relative movement of the two sides of a fault, measured in any chosen direction at the ground surface and the specific amount of the movement. In this document, the term applies both to measured and inferred displacement along a fault. The fault plane (or planes) where the seismic energy is released is called main plane and the principal faulting occurs along this plane. If the rupture occurs in the vicinity of the principal faulting, possibly on splays of the main fault or antithetic faults, it is called secondary or distributed faulting. Some researchers consider triggered ruptures to be a form secondary or distributed faulting (see triggered slip).

Surface rupture during earthquakes (SURE)

Worldwide and unified database of surface ruptures for fault displacement hazard analysis developed as part of TERPRO SURFACE project of the INQUA.

Target performance goal

Target mean annual frequency of a structure, system and component exceeding its specified limit state.

Triggered rupture

Remote triggering of displacement along a fault from a distant earthquake. The fault is in a state of critical stress such that displacement will occur due to a small stress perturbation.

ABBREVIATIONS

FDHI	fault displacement hazard initiative
GIS	geographic information system
GNSS	global navigation satellite system
InSAR	interferometric synthetic aperture radar
LiDAR	light detection and ranging
MBES	multibeam echo sounder
M_w	moment magnitude
PFDHA	probabilistic fault displacement hazard analysis
PSHA	probabilistic seismic hazard analysis
QA	quality assurance
SAR	synthetic aperture radar
SSFD	seismic source and fault displacement
SURE	surface rupture during earthquakes

CONTRIBUTORS TO DRAFTING AND REVIEW

Anooshehpoor, R.	US Nuclear Regulatory Commission, United States of America
Baize, S.	Institut de radioprotection et de sûreté nucléaire, France
Chen, R.	California Geological Survey, United States of America
Contri, P.	International Atomic Energy Agency
Dalguer, L. A.	3Q-Lab, Switzerland
Durouchoux, C.	Électricité de France, France
Fukushima, Y.	International Atomic Energy Agency
Hok, S.	Institut de radioprotection et de sûreté nucléaire, France
Guerrieri, L.	Istituto Superiore per la Protezione e la Ricerca Ambientale, Italy
Ikeda, M.	Shikoku Research Institute Inc., Japan
Inoue, N.	Geo-Research Institute, Japan
Irikura, K.	Aichi Institute of Technology, Japan
Kusumoto, S.	Kyoto University, Japan
Ono, M.	International Atomic Energy Agency
Petersen, M.	US Geological Survey, United States of America
Renault, P.	Swissnuclear, Switzerland
Scotti, O.	Institut de radioprotection et de sûreté nucléaire, France
Seber, D.	US Nuclear Regulatory Commission, United States of America
Senfaute, G.	Électricité de France, France
Sugaya, K.	Nuclear Regulation Authority, Japan
Suzuki, S.	International Atomic Energy Agency
Takao, M.	Tokyo Electric Power Company Holdings, Japan
Thio, H. K.	AECOM, United States of America
Thompson, S. C.	Lettis Consultants International, United States of America
Valentini, A.	International Atomic Energy Agency
Wong, I.	Lettis Consultants International, United States of America

CONSULTANCY MEETINGS

Vienna, Austria, 4-5 May 2017

Vienna, Austria, 1-3 November 2017

Vienna, Austria, 9-10 July 2018

Vienna, Austria, 17-18 January 2019

Vienna, Austria, 10-11 June 2019

IAEA
International Atomic Energy Agency

No. 26

ORDERING LOCALLY

IAEA priced publications may be purchased from the sources listed below or from major local booksellers.

Orders for unpriced publications should be made directly to the IAEA. The contact details are given at the end of this list.

NORTH AMERICA

Bernan / Rowman & Littlefield

15250 NBN Way, Blue Ridge Summit, PA 17214, USA
Telephone: +1 800 462 6420 • Fax: +1 800 338 4550
Email: orders@rowman.com • Web site: www.rowman.com/bernan

REST OF WORLD

Please contact your preferred local supplier, or our lead distributor:

Eurospan Group

Gray's Inn House
127 Clerkenwell Road
London EC1R 5DB
United Kingdom

Trade orders and enquiries:

Telephone: +44 (0)176 760 4972 • Fax: +44 (0)176 760 1640
Email: eurospan@turpin-distribution.com

Individual orders:

www.eurospanbookstore.com/iaea

For further information:

Telephone: +44 (0)207 240 0856 • Fax: +44 (0)207 379 0609
Email: info@eurospangroup.com • Web site: www.eurospangroup.com

Orders for both priced and unpriced publications may be addressed directly to:

Marketing and Sales Unit
International Atomic Energy Agency
Vienna International Centre, PO Box 100, 1400 Vienna, Austria
Telephone: +43 1 2600 22529 or 22530 • Fax: +43 1 26007 22529
Email: sales.publications@iaea.org • Web site: www.iaea.org/publications

International Atomic Energy Agency
Vienna